UNDERSTANDING AND OPTIMIZING HEMATITE PHOTOELECTRODES FOR PHOTOELECTROCHEMICAL WATER SPLITTING

By

Omid Zandi

A DISSERTATION

Submitted to
Michigan State University
in partial fulfillment of the requirements
for the degree of

Chemistry-Doctor of Philosophy

2015

ABSTRACT

UNDERSTANDING AND OPTIMIZING HEMATITE PHOTOELECTRODES FOR PHOTOELECTROCHEMICAL WATER SPLITTING

By

Omid Zandi

The quest for carbon-neutral renewable energy to relax our reliance on the fossil fuels in the future has been the subject of extensive research. Among all the options, sunlight by far provides the most abundant and globally well-distributed source of energy. Capturing less than 1% of the sunlight energy illuminating the earth can entirely satisfy the world's energy demand. This work is thus focused on realizing hematite as an electrode material for solar water oxidation in a photoelectrochemical cell which produces clean burning, energy dense, hydrogen fuel. A combination of sunlight, water and earth abundant hematite, thus provides an essentially unlimited resource to produce solar hydrogen fuel.

Despite several attractive properties of hematite e.g. good light absorption, proper energy levels and stability, the experimental performances measured to date have fallen well short of the theoretical expectations. The poor performance has been generally attributed to recombination processes which limit charge separation and collection on this material. Consequently, a large input voltage is required to oxidize water on hematite, which is a major loss of efficiency. In this work hematite thin films papered by atomic layer deposition were systematically investigated under solar-driven water oxidation. A combination of electrochemical and photoelectrochemical, spectroscopic, and microscopic analysis were

employed to better understand the fundamental mechanisms behind the poor performance. Performance enchantment strategies were then developed and successfully employed to boost the water oxidation performance of the electrodes. For example, substrate modification was shown that enables the deposition of highly crystalline hematite which reduces bulk recombination. The surface recombination on the other hand, was eliminated by a combination of high temperature annealing and addition of catalysts. Finally a simple and universal electrodeposition method was established to deposit highly active hematite photoelectrodes, providing a promising route to achieve efficient water splitting using this material.

ACKNOWLEDGEMENTS

I would like to thank everyone who has, by any means, contributed to this dissertation and my professional development throughout my PhD. Firstly, I would like to thank my advisor, professor Tom Hamann, for his support and guidance throughout my PhD. I am extremely grateful for all the opportunities and support he has provided for me to sustain continued progress in the research presented herein. I would also like to thank the donors of National Science Foundation (CHE-1150378) for funding this project and therefore allowing me to perform this research.

I would like to thank my colleagues and lab-mates for providing a fun and motivating working environment. Specifically, I am grateful for the productive discussions and collaborations with Ben Klahr, Kelley Young, Yuan Gao and Hamed Hajibabaei. I would also like to thank my collaborators Dr. Joseph Beardslee (Calthech) and Dr. Lionel Vayssieres (International Center for Renewable Energy). Also I extend my gratitude to my committee members, Dr. James McCusker and Dr. Rémi Beaulac, for their insightful suggestions.

Finally, I would like to thank my family and friends for their endless support during these years. This dissertation would not be possible without the support of my parents, brothers, and sisters. Specifically I would like to thank my mother to whom I dedicate this dissertation, for all her devotion and support.

TABLE OF CONTENTS

LIST OF FIGURES

Chapter 1:

Introduction

1.1 Motivation

The total energy demand worldwide in 2012 was approximately 17.5 TW (553×10^{18} J/yr). This number is expected to be doubled by the year 2050 due to the world's population growth and industrialization of the developing countries. The majority of the current energy supply is from fossil fuels, which is estimated to continue to supply at least 70% of the energy demand to fulfill the increasing energy consumption.[1] Assuming that the supply of fossil fuels is enough for the next few centuries, reliance on fossil fuels alone is associated with a huge CO_2 emission into the atmosphere resulting in the increasing atmospheric CO_2 level and global climate change. Concern of environmental consequences of global warming (which is now widely accepted and attributed to fossil fuels production/combustion products, e.g. CO_2) has led to great efforts to seek alternative renewable and environmentally green resources to reduce the future reliance on fossil fuels.

1.2 Approach

Among all alternative power options currently available (solar, wind, nuclear, biofuels, hydropower and geothermal), sunlight by far provides the most abundant and globally well-distributed energy resource. Harvesting only 0.01% of the solar photons energy hitting the earth surface instantly (120,000 TW) could essentially satisfy the world's entire energy demand.[2,3] Efficient photovoltaic (PV) systems, e.g. Si and thin film PV cells, have been available for decades which deliver power conversion efficiencies ~20%. The high production cost of these solar cells, and thus the high price ($\$0.35\ (kW\ hr)^{-1}$) of electricity delivered is the major drawback limiting their widespread use.[4,5] There have been major recent advancements in alternative PV technologies, which have the capability of disrupting

the cost/efficiency trade-off of traditional PV. In addition, an economy-of-scale reduction in the cost of Si is rapidly reducing the cost of Si-based PV down to a level nearing grid parity ($0.02-0.05 (kW hr)$^{-1}$) in parts of the United States and Europe. Another problem associated with utilizing the vast solar energy resource is that it has significant regional, seasonal and diurnal variations in intensity. One approach is to store the power generated by PVs in a batteries. With the current batteries technology, however, it is not cost and material efficient to be utilized in large scale. Thus, development of efficient routes to store solar energy in chemical fuels is almost necessary. On the other hand, about 30% of our energy demand is consumed in transportation, which requires high-energy-density chemical fuels.[6,7]

Natural photosynthesis is a great example of utilizing sunlight energy to drive chemical reaction thereby storing the energy in the chemical bonds. The overall efficiency of solar energy storage by photosynthesis is less than 1%, however.[5] Efforts have therefore been made to develop artificial photosynthesis systems capable using sunlight to drive chemical reaction uphill and produce solar fuels. The prototypical example is generating hydrogen from the photoelectrolysis of water. Hydrogen then can be used in the fuel cell engines to produce power.[2,8,9]

In artificial photosynthesis scheme, one strategy is to utilize the power generated by PV systems to drive an external electrolyzer.[8,10] Successful examples of this approach have generated solar-to-hydrogen (STH) efficiencies over 10%.[10–12] For example, recently Lue et al., reported a PV-electrolyzer system composed of earth abundant materials delivering 12.3% STH efficiency.[12] This system utilizes the advantages of a pervoskite based PV cell coupled with NiFe double hydroxide catalyst. While using earth abundant material in pervoskite/NiFe system relaxes the production costs, the long-term stability of the PV

system is the major limiting factor, which needs to be resolved in order to become commercially viable.[13] A more recent system developed by Nocera and co-workers based on a buried junction amorphous Si PV coated with cobalt-phosphate and NiMOZn catalysts provide a more robust approach as it utilizes earth abundant materials and enables stable H_2 production.[8,14] The major drawback of this system is the potentially high production cost and long term stability.

Another strategy, which is a closer analogue of natural photosynthesis, is in situ generation of hydrogen by splitting water at semiconductor electrodes, known as photoelectrochemical (PEC) water splitting.[6,15,16] The first examples of this approach were reported by Boddy[17] in 1968 and later by Fujishima and Honda[18] on single crystal TiO_2 electrodes. Extensive studies have been done since then on advancing PEC water splitting at semiconductor electrodes including exploring alternative materials beyond wide band gap TiO_2.[19] The "holy grail" of this approach is in fact a semiconductor material made of earth abundant material that offers suitable optoelectronic properties to harvest and convert the sunlight energy and is stable under relatively harsh PEC water oxidation conditions. Currently, no single material can meet theses stringent requirements and as result the PEC water splitting efficiencies has fallen well short of the theoretical expectations.[20–22]

If a single material were to be utilized the band gap should strudel the electrochemical potential of H_2O oxidation and reduction reactions, to enable unassisted PEC H_2 production. The semiconductor material therefore must have a band gap of 1.8-2.4 eV to obtain concomitant efficient light absorption and electrochemical reactions.[15,19,23] These band gap and band edge energy requirements greatly limit the choice of materials, as realizing a semiconductor material possessing right energetics has proven difficult.

An alternative tandem device configuration (an photoanode/photocathode PEC cell) relaxes some of the constraints on a single absorber photoelectrode and allows higher efficiencies by absorbing a greater fraction of solar photons.[15,24] In addition, tandem configuration allows independent optimization of photoelectrodes for water oxidation and reduction reactions. Ultimately for PEC water splitting to be practical, a tandem configuration is almost certainly necessary. In a tandem PEC cell a larger bandgap n-type semiconductor electrode (photoanode) is used to harvest the higher energy photons to perform H_2O oxidation reaction. In the other half cell (the photocathode), a narrow bandgap p-type semiconductor is used to generate H_2 from the photoelectrons generated by the lower energy photons of the solar spectrum (Figure 1-1). Despite of decades of research, realizing an efficient, scalable and stable photoanode material has remained a scientific and technological challenge which needs to be addressed to achieve efficient H_2 production via PEC water splitting. This dissertation is therefore focused on understanding and optimization of photoanode material for PEC water oxidation.

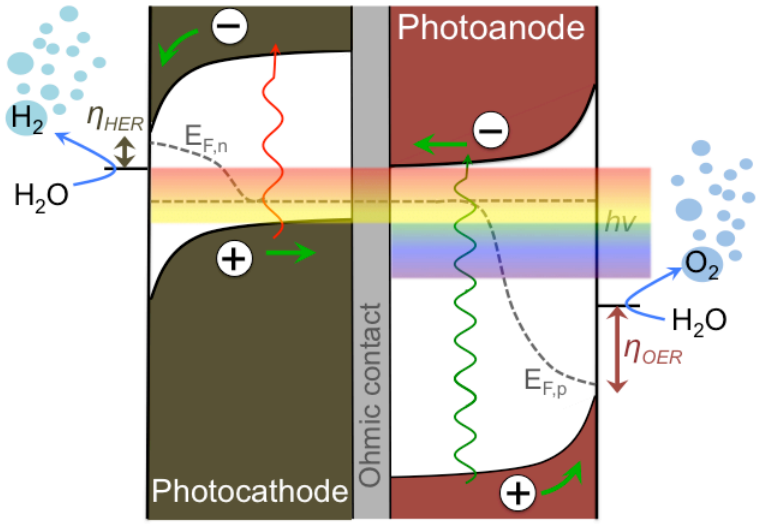

Figure 1-1. PEC water splitting in a tandem photoanode-photocathode cell.

1.3 Basics of PEC water splitting

Splitting water to O_2 and H_2 requires +238 kJ/(mol H_2O) under standard conditions, which corresponds to a –1.23 V Nernstian potential difference of the oxygen evolution (OER) and hydrogen evolution (HER) reactions, which in alkaline conditions can be written as:

$$4H_2O + 4e^- \rightarrow 2H_2 + 4OH^- \quad \text{(HER)} \qquad E^0_{red} = -0.83 \text{ V } \textit{vs}. \text{ NHE}$$

$$4OH^- \rightarrow O_2 + 4e^- + 2H_2O \quad \text{(OER)} \qquad E^0_{ox} = -0.4 \text{ V } \textit{vs}. \text{ NHE}$$

In addition to the thermodynamic potential difference, overpotentials are usually required to compensate for charge carrier recombination and the kinetics of the HER, η_{HER}, and OER, η_{OER}, at the photocathode and photoanode electrolyte interfaces, respectively. Thus, the electron quasi-Fermi level of a photocathode must be at least $-\eta_{HER}$ (V *vs*. RHE) and the quasi-Fermi level of holes of the photoanode must be at least 1.23 + η_{OER} (V *vs*. RHE) (Figure 1-1).

In PEC water splitting, a semiconductor electrode is responsible for harnessing the sunlight, while the interface at semiconductor/liquid junction (SLJ) plays a key role in separating charge carriers and subsequent chemical reactions. Understanding the physicochemical characteristics of the SLJ is therefore particularly important for designing efficient PEC systems. The energetics of an n-type semiconductor is schematically shown in Figure 1-2. When a semiconductor is brought in contact with the solution with electrochemical potential of E_s, electrons will flow between the semiconductor and the electrolyte until equilibrium is established. This charge transfer produces a potential energy gradient at the interface termed “band bending” (Figure 1-2b). The extent of the band

bending is depending on the initial Fermi level energy of the semiconductor (i.e. flat band potential, E_{fb}) for a given semiconductor dopant density (N_D). Band bending enhances charge separation at the interface by directing the minority carries (holes for an n-type semiconductor) to the SLJ and majority carriers (electrons) to the current collector. The layer over which the semiconductor is ionized is called "depletion width" (W), which depends on the potential difference between E_{fb} and E_s (i.e. built-in potential, V_{bi}) and dopant density of the semiconductor (N_D in cm^{-3}):

$$W = \left(\frac{2\kappa\varepsilon_0 V_{bi}}{qN_D}\right)^{1/2} \quad (1\text{-}1)$$

Where κ is the dielectric constant of the semiconductor, and ε_0 is the vacuum permittivity (8.854×10^{-14} C V^{-1} cm^{-1}). The difference between electrons and holes quasi-Fermi levels under illumination determines the magnitude of the photovoltage that can be generated at SLJ (Figure 1-2c). The photovoltage generated under solar illumination can be used to run chemical reactions uphill, e.g. splitting H_2O at potential below thermodynamic oxidation potential. This value in practice is usually smaller than the maximum theoretically extractable energy due to different electron-hole recombination processes, which alter the position of quasi-Fermi levels (electron and hole Fermi level under illumination).[15] Recombination losses in the depletion region and surface are known to be the most contributing factors limiting the photovoltage of H_2O oxidation (by reducing the quasi Fermi level splitting under illumination).[25,26] In addition to surface recombination, bulk recombination of photogenerated charge carriers is another major efficiency loss factor, which limits the charge separation efficiency and thus the photocurrent output (see below).

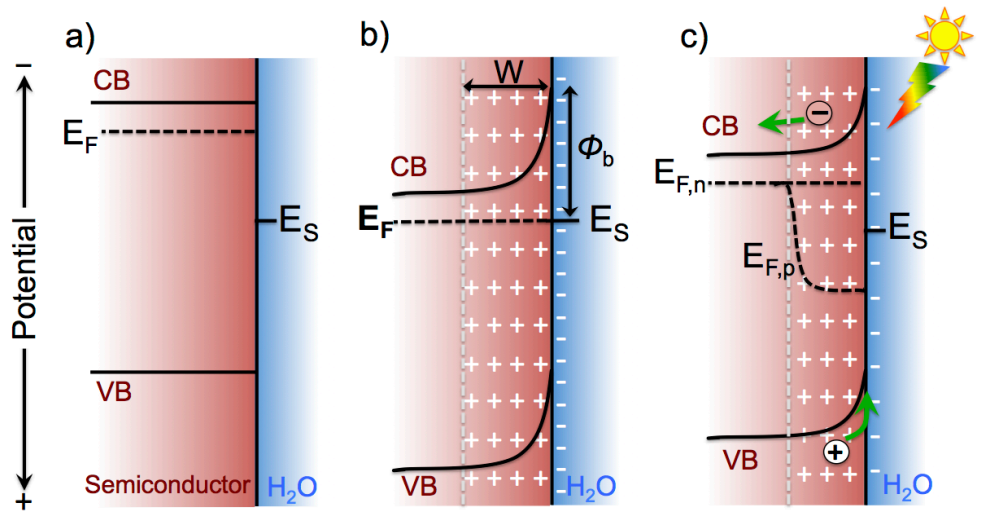

Figure 1-2. Energetics of an n-type semiconductor under conditions of flat band (a) and in equilibrium with an aqueous electrolyte of electrochemical potential E_s in dark (b) and under illumination (c).

1.3.1 Performance evaluation

1.3.1.1 Current-potential (*J-V*) measurements

Single photoelectrodes are often examined under PEC water oxidation conditions in a three-electrode electrochemical cell configuration. This allows for individual characterization of the photoelectrodes independent of any polarization losses at the counter electrode. While the single photoelectrode efficiency does not represent the overall efficiency of the PEC cell, a general principle to calculate efficiency for single photoelectrodes is presented here which could be employed to compare different systems and separately optimize new photoanode and photocathode materials. The efficiency of a single photoelectrode in the three-electrode configuration setup can be calculated directly from the *J-V* response using following equation (Figure 1-3):[15]

$$\eta_{el} = \frac{J_m \times V_m}{P_{in}} \quad (1\text{-}2)$$

Where J_m (in mA cm^{-2}) is the photocurrent density at maximum power point and V_m (in V) is the photovoltage generated at maximum power point with respect to thermodynamic standard potentials (1.23 V for H_2O oxidation on a photoanode), and P_{in} is the illumination power (100 mW cm^{-2}). The efficiency of a single electrode therefore can be readily determined through inspection of a *J-V* curve as shown in Figure 1-3 for the photoanode. It should be noted efficiency calculation for a single photoelectrode is meaningful only when photocurrent is generated at potentials negative of 1.23 V *vs.* RHE.

The solar-to-hydrogen efficiency, η_{STH}, for a complete tandem PEC cell under operating condition can be also calculated form the *J-V* curves using equation 3, assuming unity faradaic efficiency (Figure 1-3),[15]

$$\eta_{STH} = \frac{J_{op} \times 1.23 \text{ V}}{P_{in}} \quad (1\text{-}3)$$

Where J_{op} is the operating current density in mA cm^{-2} and P_{in} is the incident light power density (AM1.5, 100 mW cm^{-2}). In a tandem cell maximum STH efficiencies >20 % is predicted for an optimum band gap alignment and minimum overpotential losses at each photoelectrode/electrocatalyst (i.e. band gaps of 1.6 and 0.95 eV for the photoanode and photocathode, respectively).[27,28] This efficiency figure thus makes tandem PEC cells particularly attractive, which can be achieved in a relatively simple design.

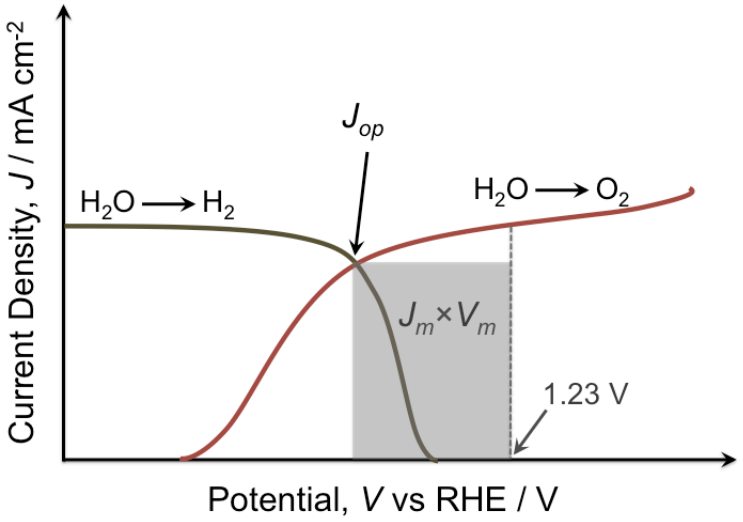

Figure 1-3. Schematic *J-V* characteristics of a tandem PEC cell under operating condition. The matching point of the *J-V* curves determines the output current of a tandem cell, J_{op}. Shaded box is the maximum power generated by the photoanode, which can be used to calculate single electrode efficiency using equation 2.

1.3.1.2 IPCE and APCE measurements

The photocurrent and photovoltage under white light (AM1.5G) illumination is used for the calculation of overall energy conversion efficiency. Another way of assessing the photoelectrodes performance is measuring the quantum efficiency or spectral response under monochromatic illumination. The quantity of *incident photons-to-current conversion efficiency* (IPCE), or *external quantum efficiency* is often used to define the fraction of the incident photons that are converted to electrons in the external circuit.[29]

$$IPCE(\lambda) = \frac{no.\ of\ carriers}{no.\ of\ incident\ photons} = \frac{J_{ph}}{\lambda P_{in}} \times \frac{hc}{e} \qquad (1\text{-}4)$$

Where J_{ph} (A cm^{-2}) is photocurrent, λ is wavelength, P_{in} (W cm^{-2}) is the incident power, h is Planck's constant, c is the speed of light, and e is electron charge. IPCE measurements are

helpful when trying to elucidate the performance limiting factors at different stages of charge separation and transport. From the IPCE one can quantify the conversion efficiency of absorbed photons contributing to the photocurrent. For example by comparing the front and backside illuminated IPCE it is possible to determine whether electron or hole transport is the limiting charge transport factor and finally extract carrier diffusion length.[29,30] IPCE only considers the power of incident light and does not take into account the photons that are transmitted or reflected by the electrode. Dividing the IPCE by light harvesting efficiency (absorptance) produces the *internal quantum efficiency*, or *absorbed photon-to-current conversion efficiency (APCE)* of the electrodes.

$$APCE(\lambda) = \frac{IPCE(\lambda)}{Absorptance} = \frac{IPCE(\lambda)}{1\text{-}T\text{-}R} \qquad (1\text{-}5)$$

T and *R* are the fraction of transmitted and reflected light by the electrode. APCE is another useful parameter, which give a better quantitative assessment of the fraction of the absorbed photons contributing to the photocurrent. Any deviation from 100% APCE can be clearly attributed to the recombination of the photogenerated carriers in the bulk or on the surface of the electrode. APCE values over the entire absorption profile of the electrode would give a clear picture of the charge collection efficiency at different wavelengths. One can also deconvolute bulk recombination from surface recombination by employing a good hole scavenger (e.g. a fast redox couple such as $Fe(CN)_6^{3/4-}$, or H_2O_2). IPCE and APCE measurements under H_2O oxidation and the oxidation of a hole scavenger therefore provide a platform to analyze the degree by which bulk and surface recombination limit the water oxidation performance of the photoelectrodes.

1.4 Photoanode materials

An ideal photoanode material must fulfill several stringent requirements in order to effect stable and efficient H_2O oxidation under solar illumination:

1. It should be an n-type semiconductor in order to effectively utilize the band-bending electric field to separate charge carriers at the SLJ
2. It needs to be a good absorber in the visible part of the solar spectrum
3. The valence band position must be positive of H_2O oxidation potentials
4. The semiconductor needs to be stable under harsh PEC water splitting conditions
5. The charge transport properties must favorably outcompete the recombination losses processes to produce high quantum yields with minimal applied bias

While there is a long list of materials that can harvest the sunlight and possess appropriate energetics, the stability requirement basically limits the photoanode candidates to metal oxide-based semiconductors. Metal oxide candidates, however, are either wide band gap materials or offer poor charge transport and stability.[15,19] Therefore, no single semiconductor material is known to date that can fulfill all of the above requirements. TiO_2 is one of the most studied photoanode materials, which provide a classic benchmark for fundamentals studies on oxide-based photoanodes. Poor light harvesting ability of TiO_2, however, sets a fundamental restriction on efficient PEC water splitting using this material.

Metal oxide semiconductors such as α-Fe_2O_3, WO_3, $CuWO_4$, and $BiVO_4$ offer better light-harvesting ability, though (in some cases) at the expense of poorer charge transport properties compared to TiO_2.[19,31] The energetics of some promising oxide, oxynitride, and nitride photoanode materials is schematically shown in Figure 1-4, comparing the

conduction and valence band edge energies, band gap, and maximum theoretically achievable photocurrent under AM1.5G solar illumination.

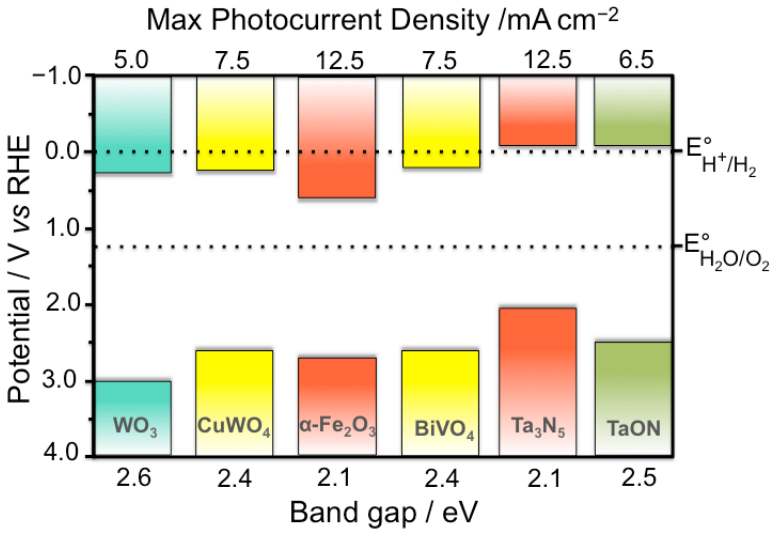

Figure 1-4. Schematic energetics of metal oxide and nitride photoanode candidates for photocatalytic water oxidation. The maximum photocurrent density is estimated by integrating the solar photons with the energy $\geq E_{gap}$ and assuming the quantum efficiency of unity.

WO_3 is another promising material that offers better charge transport properties compared to hematite, albeit with significantly weaker light harvesting ability. WO_3 has a band gap of 2.6-2.7 eV and its valence band is sufficiently positive for H_2O oxidation.[32–35] The flat band potential of WO_3 (~ 0.4 V *vs* RHE) is more negative of that of hematite (~ 0.55-0.6 V *vs.* RHE), which provides an extra photovoltage for H_2O splitting.[24,31] The major drawback of WO_3, beside its poor light absorption, is instability in neutral and basic pH and surface photocorrosion under illumination and positive applied potentials. Efforts have been made to enhance the chemical stability as well as the light harvesting ability of WO_3.[33,34,36] A very promising strategy, which has been shown to enhance the light harvesting ability as

well as the PEC stability of WO_3 is alloying with copper oxide. Copper tungstate ($CuWO_4$) has a reported bang gap of ~ 2.4 eV and enhanced stability.[35,37,38]

BiVO4 is another ternary oxide with the band gap of ~ 2.4 eV first recognized by Kudo *et al.*.[39] Since then, drastic enhancement in PEC H_2O splitting performance of $BiVO_4$ photoanodes have been achieved mainly through doping with W[40–42] and Mo[43,44] and surface modification with water oxidation catalysts.[45–48] The state of the art electrodes have produced photocurrent values in the order of 3-4 mA cm^{-2} and IPCE values up to 70% at 1.23 V vs RHE.[40,47]

(TaON) and tantalum nitride (Ta_3N_5) are another earth-abundant-based class of materials, which have received a lot of recent interests.[49–54] The problem of nitride-based materials, however, is their instability under H_2O oxidation conditions. The surface of these materials quickly undergoes photo-oxidation, forming insulating oxide layer on the surface.[55] While TaON have shown to be more stable than Ta_3N_5, effective surface protection strategies are crucial to achieve sustained H_2O oxidation with these materials. Another challenge with nitride-based materials is the synthesis process as it requires high temperature ammonolysis to obtain high quality Ta_3N_5 material. High temperature treatment limits the utilization of conventional transparent conductive substrates, which is necessary for tandem cell integration.

1.5 Hematite (α-Fe_2O_3)

The optimum performance for a photoanode in tandem configuration PEC cell is between 1.8 and 2.3 eV.[23,56] Among different photoanode materials outlined above, hematite with the band gap of 2.1 eV stands out as promising material fulfilling most of the

mentioned requirements for an ideal photoanode. Integrating the AM 1.5 solar spectrum photon flux for the bandgap of 2.1 eV produces a maximum photocurrent density of 12.5 mA cm^{-2}, assuming unity quantum yield. Therefore, the STH efficiency of ~15% is achievable with hematite in a tandem configuration with a suitable photocathode. In addition to a good light absorption, hematite offers excellent stability in neutral and basic pH, which is desired for the H_2O oxidation reaction. Further, iron and oxygen are amongst the most abundant elements in the earth crust, which promises the scalability of PEC devices based on hematite. Despite all these attractive properties, the experimental PEC water oxidation efficiency with hematite has remained poor despite of nearly two decades of extensive research.

Hematite phase of iron oxide has a corundum structure in which two face-sharing FeO_6 polyhedra occur along the *c* axis. The resulting Fe_2O_9 units share edges and corners with each other to form sheets of FeO_6 polyhedra perpendicular to the *c* axis. Because of the face sharing and resulted repulsion between the Fe^{3+} cation centers, FeO_6 coordinations have a slight trigonal (C_{3v} symmetry) distortion.[57,58] From a molecular orbital point of view, the valence band of hematite is mostly composed of O 2p orbitals. The substantial contribution from the Fe 3d, 4s, and 4p orbitals, however, results in some degree of covalency in hematite.[57–59] The bottom of the conduction band is mostly Fe 3d in character localized on iron atoms, albeit with some contribution from O 2p orbitals due to the mentioned covalency.

Two major electronic transitions in hematite are d-d (described by ligand field theory) and ligand-to-metal charge transfer (LMCT) transitions.[57,58] Transitions from high spin ground state in Fe^{3+} to the excited ligand field states are both spin and parity-forbidden.

These transitions can become allowed through magnetic coupling between the nearest Fe^{3+} atoms in the hematite lattice.[58] The LMCT transitions include excitations from O 2p valence band orbitals to Fe 3d crystal field type orbitals. The lowest energy LMCT transition of this series is from nonbonding molecular orbitals localized on O 2p orbitals to the antibonding Fe 3d t_{2g} orbitals.[57,58] Two electronic transitions peaks in hematite around 430 and 550 nm are both assigned to ligand field transitions (Figure 1-5). The LMCT transitions are mainly occur in the UV region of the spectrum.[58] The intense absorption peaks resulting from d-d transitions (which are unexpected based on selection rules) has been explained in terms of magnetic coupling between adjacent Fe atoms as well as the trigonal distortion enforced by the face sharing FeO_6 polyhedra in hematite which both result in the relaxation of the selection rules.[57,58,60,61]

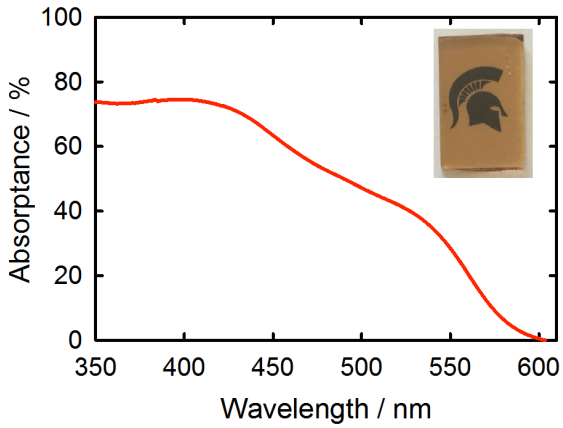

Figure 1-5. Absorptance spectra of 50 nm hematite electrode prepared by ALD.

1.5.1 PEC water oxidation with hematite

The overall photocurrent (J_{ph}) that can be generated under H_2O oxidation on a semiconductor surface can be expressed as a function of three process efficiencies and the

solar photons flux (ϕ): light harvesting efficiency (η_{lh}), charge separation efficiency (η_{cs}), and hole collection efficiency (η_{hc}) *via* H_2O oxidation reaction (Figure 1-6):

$$J_{ph}=-q\phi\left(\eta_{lh}\times\eta_{cs}\times\eta_{hc}\right) \tag{1-7}$$

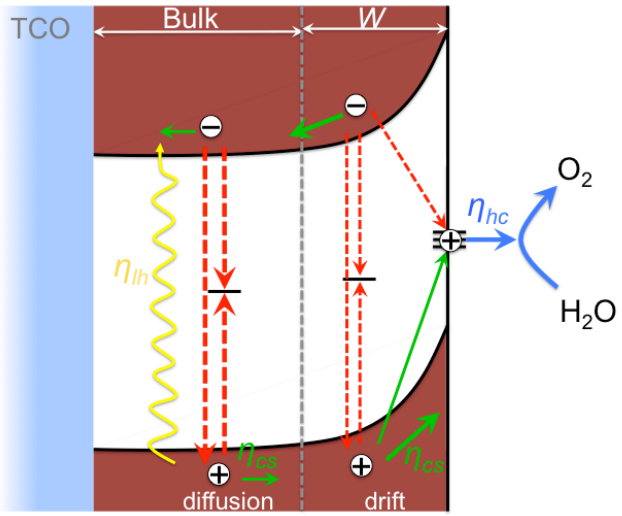

Figure 1-6. Schematic charge transfer processes in hematite under PEC water oxidation. The water oxidation photocurrent is controlled by the efficiency of light harvesting, charge separation, and hole collection processes. Red arrows indicate recombination pathways.

The light harvesting efficiency at a given wavelength (λ) is expressed by Beer's law as a function of semiconductor absorption coefficient (α) and electrode thickness (l): $\eta_{lh}=1-\int e^{-\alpha(\lambda)l}\,d\lambda$. A semiconductor electrode must therefore be $3/\alpha$ thick to absorb 95% of the incident light at a given wavelength.[22]. A plot of calculated maximum photocurrent density (assuming unity conversion efficiency, i.e. $\eta_{cs}=\eta_{hc}=1$) for a hematite electrode as function electrode thickness is shown in Figure 1-7. The photocurrent reaches the maximum ~12.4 mA cm^{-2} at around 1 μm with subtle increase by further increasing the thickness to 2

μm. The photocurrent density of over 10 mA cm^{-2} is possible, however, for a thickness of 500 nm owing to high absorptivity of hematite (α=6×$10^4$$cm^{-1}$ at 550 nm)[22].

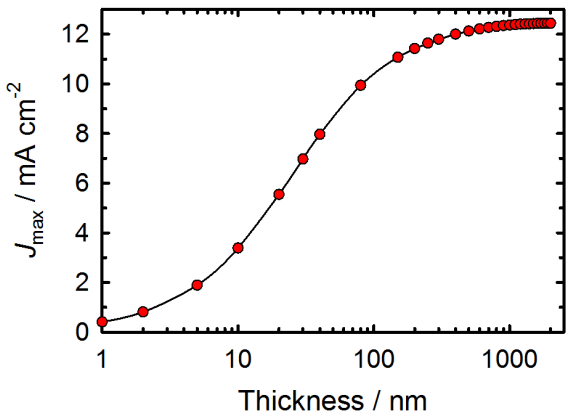

Figure 1-7. Maximum photocurrent density calculated for hematite a function of electrode thickness assuming unity quantum yield for absorbed photons and negligible reflection loss.

1.6 Atomic layer deposition (ALD)

ALD is a gas phase vacuum deposition technique which has received extensive attention for variety of application, e.g. semiconductors, electronics, catalysis, and photocatalysis.[62] ALD working principle is based on the sequential pulsing of two or more reagents which react with the surface of the substrate in a self-limiting manner (Figure 1-8). ALD offer several unique properties, e.g.:

- Gas phase reaction enables uniform and conformal coating of planar and porous substrates
- Angstrom control over the film thickness
- Precise control over the film composition which is ideal for doping and stack deposition

- Excellent control over the film morphology determined by the substrate

ALD can, in principal, be utilized to deposit variety of metal oxide and nitrides using a metal precursor and a suitable co-reactant.[62] In this work ALD was utilized to despite uniform thin films of hematite using ferrocene as Fe precursor and ozone as the oxidant.[63] The ALD made planar hematite thin film are ideal for preforming fundamental investigations. Further, ALD can be utilized to despite surface coatings (e.g. addition of a catalyst) or doping using alternative metal oxide cycles.[64,63]

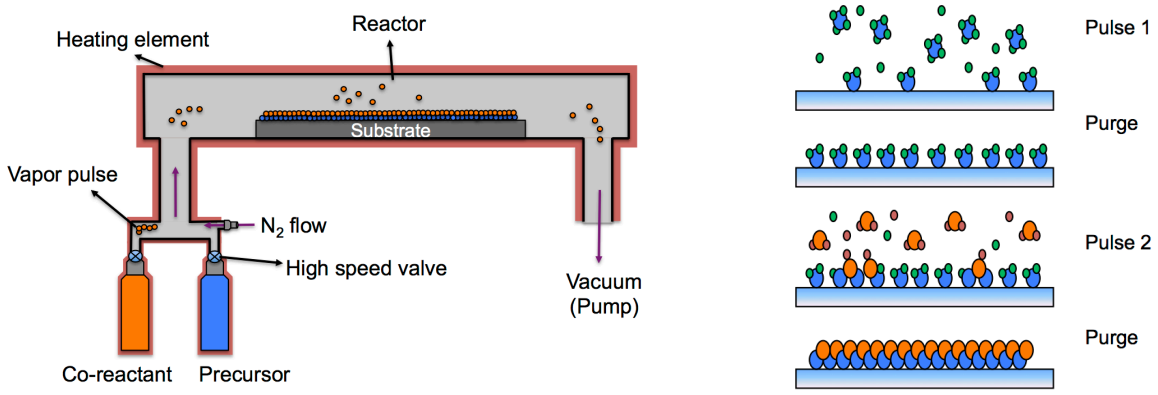

Figure 1-8. Schematic illustration of an ALD instrument (left) and a basic representation of an ALD cycle processes which can be repeated to obtain a desired thickness (left).

1.7 Objectives

PEC water oxidation with hematite has remained inefficient despite of nearly two decades of extensive research.[22,65,66] This is due to charge carrier recombination in the bulk and on the electrode surface, which limit the quantum efficiency of charge separation/transfer and thereby the water oxidation efficiency. Due to intrinsically short (near zero) hole diffusion length in hematite, charge collection length is limited to the depletion width (~20 nm).[63,67] A great research thrust thus has been focused on

nanostructured electrode, which decouples the light absorption depth form the charge collection length thus maximizing the light absorption.[68–70] Although the nanostructured electrodes have produced significant photocurrent enhancement, the overall performance, particularly the photovoltage, is well below the theoretical expectations. In addition to bulk recombination, surface recombination is another major efficiency loss, which is in competition with the forward hole transfer to H_2O molecules. Surface recombination limits the photovoltage under H_2O oxidation, resulting in a very positive photocurrent onset potential. The goal of this dissertation is to acquire an in depth understanding of different charge recombination pathways in the bulk and on the surface using model thin film hematite electrodes prepared by atomic layer deposition (ALD). Unique gas phase and self-limiting surface reaction in ALD allows uniform and conformal thin films, which are ideal for fundamental studies and performing precise structure-function investigation. Once the efficiency limiting processes are elucidated, the thin films can be optically scaled up through depositing an optimized hematite thickness on nanostructured conductive substrates.

REFERENCES

REFERENCES

(1) Energy Information Administration, www.eia.doe.gov.

(2) Lewis, N. S.; Nocera, D. G. *Proc. Natl. Acad. Sci. U. S. A.* **2006**, *103*, 15729.

(3) Smalley, R. E. *MRS Bull.* **2005**, *30*, 412.

(4) Martin, G. A.; Emery, K.; Hishikawa, Y.; Warta, W.; Dunlop, E. D. *Prog. Photovoltaics Res. Appl.* **2012**, *20*, 6.

(5) Lewis, N. S. *Science* **2007**, *315*, 798.

(6) Peter, L. M.; Upul Wijayantha, K. G. *ChemPhysChem* **2014**, *15*, 1983.

(7) Young, K. M. H.; Klahr, B. M.; Zandi, O.; Hamann, T. W. *Catal. Sci. Technol.* **2013**, *3*, 1660.

(8) Nocera, D. G. *Acc. Chem. Res.* **2012**, *45*, 767.

(9) Cook, T. R.; Dogutan, D. K.; Reece, S. Y.; Surendranath, Y.; Teets, T. S.; Nocera, D. G. *Chem. Rev.* **2010**, *110*, 6474.

(10) Khaselev, O.; Turner, J. A. *Science (80-.).* **1998**, *280*, 425.

(11) Heller, a; Laboratories, B.; Hill, M. *J. Electrochem. Soc.* **1982**, 2865.

(12) Luo, J.; Im, J.-H.; Mayer, M. T.; Schreier, M.; Nazeeruddin, M. K.; Park, N.-G.; Tilley, S. D.; Fan, H. J.; Gratzel, M. *Science (80-.).* **2014**, *345*, 1593.

(13) Hamann, T. W. *Science (80-.).* **2014**, *345*, 1566.

(14) Kanan, M. W.; Nocera, D. G. *Science* **2008**, *321*, 1072.

(15) Walter, M. G.; Warren, E. L.; Mckone, J. R.; Boettcher, S. W.; Mi, Q.; Santori, E. A.; Lewis, N. S. *Chem. Rev.* **2010**, *110*, 6446.

(16) Grätzel, M. *Nature* **2001**, *414*, 338.

(17) Boddy, P. J. *J. Electrochem. Soc.* **1968**, *115*, 199.

(18) Fijishima, A.; Honda, K. *Nature* **1972**, *238*, 37.

(19) Chen, Z.; Jaramillo, T. F.; Deutsch, T. G.; Kleiman-Shwarsctein, A.; Forman, A. J.; Gaillard, N.; Garland, R.; Takanabe, K.; Heske, C.; Sunkara, M.; McFarland, E. W.; Domen, K.; Miller, E. L.; Turner, J. a.; Dinh, H. N. *J. Mater. Res.* **2011**, *25*, 3.

(20) Brillet, J.; Gratzel, M.; Sivula, K. *Nano Lett.* **2010**, *10*, 4155.

(21) Lindgren, T.; Wang, H.; Beermann, N.; Vayssieres, L.; Hagfeldt, A.; Lindquist, S.-E. *Sol. Energy Mater. Sol. Cells* **2002**, *71*, 231.

(22) Hamann, T. W. *Dalton Trans.* **2012**, *41*, 7830.

(23) Bolton, J. R.; Strickler, S. J.; Connolly, J. S. *Nature* **1985**, *316*, 495.

(24) Brillet, J.; Yum, J.-H.; Cornuz, M.; Hisatomi, T.; Solarska, R.; Augustynski, J.; Graetzel, M.; Sivula, K. *Nat. Photonics* **2012**, *6*, 824.

(25) Gärtner, W. *Phys. Rev.* **1959**, *116*, 84.

(26) Reichman, J. *Appl. Phys. Lett.* **1980**, *36*, 574.

(27) Prévot, M. S.; Sivula, K. *J. Phys. Chem. C* **2013**, *117*, 17879.

(28) Hu, S.; Xiang, C.; Haussener, S.; Berger, A. D.; Lewis, N. S. *Energy Environ. Sci.* **2013**, *6*, 2984.

(29) van de Krol, R.; Grätzel, M., *Photoelectrochemical Hydrogen Production*; Springer US: Boston, MA, 2012; Vol. 102.

(30) Abdi, F. F.; Van de Krol, R. *J. Phys. Chem. C* **2012**, *116*, 9398.

(31) Sivula, K. *J. Phys. Chem. Lett.* **2013**, *4*, 1624.

(32) Hill, J.; Choi, K. *J. Phys. Chem. C* **2012**, *116*, 7612.

(33) Seabold, J. A.; Choi, K. S. *Chem. Mater.* **2011**, *23*, 1105.

(34) Liu, R.; Lin, Y.; Chou, L.-Y.; Sheehan, S. W.; He, W.; Zhang, F.; Hou, H. J. M.; Wang, D. *Angew. Chem. Int. Ed. Engl.* **2011**, *50*, 499.

(35) Yourey, J. E.; Kurtz, J. B.; Bartlett, B. M. *J. Phys. Chem. C* **2012**, *116*, 3200.

(36) Klepser, B. M.; Bartlett, B. M. *J. Am. Chem. Soc.* **2014**, *136*, 1694.

(37) Doumerc, J. P.; Hejtmanek, J.; Chaminade, J. P.; Pouchard, M.; Krussanova, M. *Phys. status solidi* **1984**, *286*, 285.

(38) Hill, J. C.; Choi, K.-S. *J. Mater. Chem. A* **2013**, *1*, 5006.

(39) Kudo, a; Ueda, K.; Kato, H.; Mikami, I. *Catal. Letters* **1998**, *53*, 229.

(40) Abdi, F. F.; Han, L.; Smets, A. H. M.; Zeman, M.; Dam, B.; van de Krol, R. *Nat. Commun.* **2013**, *4*, 1.

(41) Abdi, F. F.; Savenije, T. J.; May, M. M.; Dam, B.; van de Krol, R. *J. Phys. Chem. Lett.* **2013**, *4*, 2752.

(42) Ye, H.; Park, H. S.; Bard, A. J. *J. Phys. Chem. C* **2011**, *115*, 12464.

(43) Yao, W.; Iwai, H.; Ye, J. *Dalton Trans.* **2008**, 1426.

(44) Pilli, S. K.; Furtak, T. E.; Brown, L. D.; Deutsch, T. G.; Turner, J. a.; Herring, A. M. *Energy Environ. Sci.* **2011**, *4*, 5028.

(45) Zhong, D. K.; Choi, S.; Gamelin, D. R. *J. Am. Chem. Soc.* **2011**, *133*, 18370.

(46) Seabold, J. a; Choi, K.-S. *J. Am. Chem. Soc.* **2012**, *134*, 2186.

(47) Kim, T. W.; Choi, K.-S. *Science (80-.).* **2014**, *343*, 990.

(48) Abdi, F. F.; Van de Krol, R. *J. Phys. Chem. C* **2012**.

(49) Ho, C. T.; Low, K. Bin; Klie, R. F.; Maeda, K.; Domen, K.; Meyer, R. J.; Snee, P. T. *J. Phys. Chem. C* **2011**, *115*, 647.

(50) Pinaud, B.; Vailionis, A.; Jaramillo, T. *Chem. Mater.* **2014**, *26*, 1576.

(51) Dabirian, A.; Van de Krol, R. *Chem. Mater.* **2015**, *27*, 708.

(52) Li, M.; Luo, W.; Cao, D.; Zhao, X.; Li, Z.; Yu, T.; Zou, Z. *Angew. Chem. Int. Ed. Engl.* **2013**, *550*, 1.

(53) Feng, X.; Latempa, T. J.; Basham, J. I.; Mor, G. K.; Varghese, O. K.; Grimes, C. a. *Nano Lett.* **2010**, *10*, 948.

(54) Liu, G.; Shi, J.; Zhang, F.; Chen, Z.; Han, J.; Ding, C.; Chen, S.; Wang, Z.; Han, H.; Li, C. *Angew. Chemie - Int. Ed.* **2014**, *53*, 7295.

(55) Hara, M.; Chiba, E.; Ishikawa, A.; Takata, T.; Kondo, J. N.; Domen, K. *J. Phys. Chem. B* **2003**, *107*, 13441.

(56) Peter, L. M. *J. Solid State Electrochem.* **2012**, *17*, 315.

(57) Sherman, D. M. *Phys. Chem. Miner.* **1985**, *12*, 161.

(58) Sherman, D. M.; Waite, D. T. *Am. Mineral.* **1985**, *70*, 1262.

(59) Tossell, J. A.; Gibbs, G. V. *Phys. Chem. Miner. Miner.* **1977**, *57*, 21.

(60) Pailhé, N.; Wattiaux, a.; Gaudon, M.; Demourgues, a. *J. Solid State Chem.* **2008**, *181*, 1040.

(61) Pailhé, N.; Wattiaux, a.; Gaudon, M.; Demourgues, a. *J. Solid State Chem.* **2008**, *181*, 2697.

(62) George, S. M. *Chem. Rev.* **2010**, *110*, 111.

(63) Klahr, B. M.; Martinson, A. B. F.; Hamann, T. W. *Langmuir* **2011**, *27*, 461.

(64) Riha, S. C.; Klahr, B. M.; Tyo, E. C.; Seifert, S.; Vajda, S.; Pellin, M. J.; Hamann, T. W.; Martinson, A. B. F. *ACS Nano* **2013**, *7*, 2396.

(65) Sivula, K.; Le Formal, F.; Grätzel, M. *ChemSusChem* **2011**, *4*, 432.

(66) Katz, M. J.; Riha, S. C.; Jeong, N. C.; Martinson, A. B. F.; Farha, O. K.; Hupp, J. T. *Coord. Chem. Rev.* **2012**, *256*, 2521.

(67) Klahr, B. M.; Hamann, T. W. *Appl. Phys. Lett.* **2011**, *99*, 063508 1.

(68) Kay, A.; Cesar, I.; Grätzel, M. *J. Am. Chem. Soc.* **2006**, 15714.

(69) Riha, S. C.; Devries Vermeer, M. J.; Pellin, M. J.; Hupp, J. T.; Martinson, A. B. F. *ACS Appl. Mater. Interfaces* **2013**, *5*, 360.

(70) Mayer, M. T.; Lin, Y.; Yuan, G.; Wang, D. *Acc. Chem. Res.* **2013**, *46*, 1558.

Chapter 2:

Substrate Dependent Water Splitting with Ultrathin Hematite Electrodes

Adapted with permission from:

Substrate Dependent Water Splitting with Ultrathin α-Fe_2O_3 Electrodes, Omid Zandi, Joseph A. Beardslee, and Thomas W. Hamann, *J. Phys. Chem. C* **2014**, *118* (30), 16494–16503.

2.1 Abstract

Thin films of hematite (α-Fe_2O_3) were deposited by atomic layer deposition (ALD) and the effects of metal oxide underlayers on the photocatalytic water oxidation performance were investigated. It was found that a Ga_2O_3 underlayer dramatically enhances the water oxidation performance of the thinnest hematite films. The performance enhancement is attributed to the increased crystallinity of the ultrathin films induced by the oxide underlayers. The degree of crystallinity was examined by Raman line shape analysis of the characteristic hematite phonon modes. It was found that multiple metal oxide underlayers, including Nb_2O_5, ITO and WO_3, increase the film crystallinity compared to hematite deposited on bare FTO. The increased crystallite size was also clearly evident from the high resolution SEM images. The degree of crystallinity was found to correlate with the photocatalytic performance. These findings shed light on the origin of the dead layer at the interface of the FTO substrate and ultrathin hematite films and elucidate strategies at overcoming it.

2.2 Introduction

In the previous chapter hematite was introduced as promising photoanode material for photoelectrochemical (PEC) water splitting due to good light absorption, excellent stability, and suitable energetics for H_2O oxidation. Poor charge transport properties in bulk hematite, however, has limited the photocurrent output to values below one quarter of maximum expected photocurrent based on the flux of the absorbed light. The poor charge separation efficiency is attributed to the high rate electron-hole recombination in the bulk, happening immediately after excitation. Bulk recombination is a cause of a very short hole diffusion length (reported to be >5 nm). This implies that the photogenerated holes outside of this thickness are not collected *via* diffusion and therefore undergo recombination. In the depletion region, however, the band bending potential gradient enhances charge separation by drifting the hole to the electrode surface and electrons to the back contact. As far as charge separation is concerned, an optimum hematite electrode must therefore be as thick as the "*depletion width + one hole diffusion length*". This collection length is in a vast contrast with the light penetration depth (~500 nm); meaning that while a thickness of nearly 500 nm is required to obtain complete light absorption, photogenerated holes are only collected for the ~ 20 nm thickness at the interface with the electrolyte. This situation is shown for a thick planar hematite electrode is Figure 2-1a. Efforts have been made to decouple this scale mismatch by fabricating hematite electrodes with nanostructured morphology. The idea is to deposit mesoporous structures with feature size in the order of 20 nm that are optically thick in one direction to enable efficient light absorption while maintaining the majority of the bulk volume within the hole collection length (Figure 2-1b).

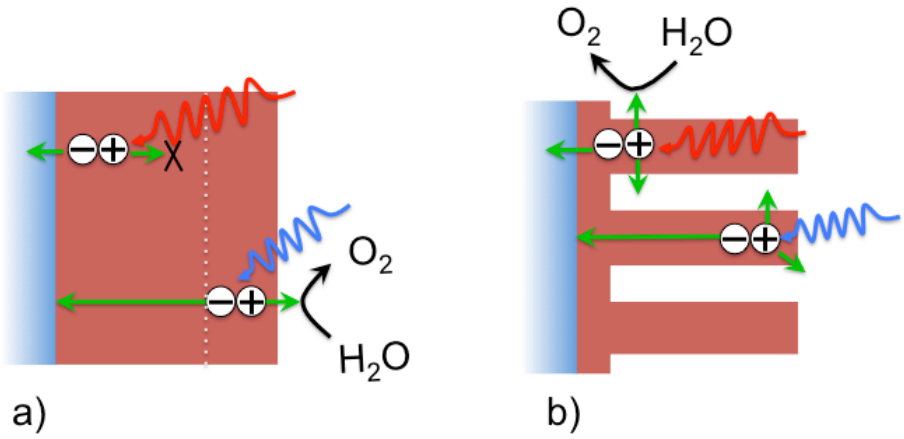

Figure 2-1. Schematic charge separation modes in a thick planar hematite electrode (a) compared to an optimized thickness in a nanostructured morphology (b).

Nanostructuring can be essentially employed in two approaches:

1) Fabricating high aspect ratio hematite electrode with nanoscale structure (Figure 2-1b), e.g. nanotubes,[1] nanowires,[2] nano-cauliflowers,[3] and mesoporous nanoparticle.[4] The first successful example of this approach was reported by Grätzel and co-workers on nano-cauliflower hematite electrodes prepared by chemical vapor deposition which produced current densities over 3 mA cm^{-2} at 1.23 V vs RHE.[3]

2) Thin film absorber (TFA) electrodes deposited on high aspect ratio transparent conductive oxide (TCO) substrates (Figure 2-2). This method, which has received somewhat less attention, is an attractive approach as it allows uniform hematite films with optimized dimensions, which are optically scaled up over the nanostructured conductive substrate. Examples of this approach include coating high surface area conducting substrates such as nanonets,[5] tungsten oxide[6] or nanostructured TCO substrates e.g. nanoparticle Nb:SnO_2,[7] or indium doped tin oxide (ITO) inverse opals,[8] which all have produced substantially higher

photocurrent compared to planar electrodes. One of the significant advantages of the TFA approach is electrodes are amenable to detailed systematic investigation of the material in the form of planar thin films with controllable geometry. The downside of this approach is a substrate-thin film interface effect that can decrease charge separation through inducing a defective hematite layer, which is the focus of this chapter.

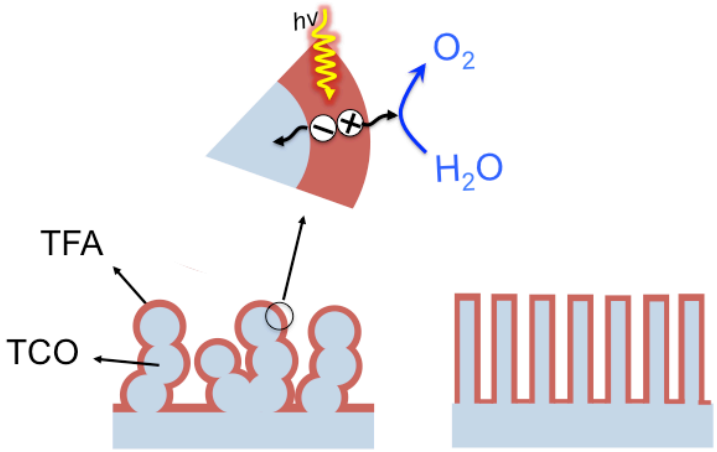

Figure 2-2. Schematic illustration of thin film absorber (TFA) hematite deposited on nanostructured transparent conductive oxide (TCO) substrates with different morphologies.

TFA nanostructuring is an attractive and promising approach for enhancing light absorption and charge separation in hematite electrodes. Electrode thicknesses in the order of depletion width (i.e. 20 nm) perform very poor under PEC water oxidation condition, however. This effect, which is general to different preparation methods, is attributed to the substrate-hematite film interface effect which results in a imperfect hematite film, generally known as "dead layer".[9–12]

While the exact cause of the dead layer is still not fully understood, some combination of an accelerated rate of recombination and/or decreased hole mobility in the dead layer

prevents the efficient charge separation and transport to the electrolyte interface to perform the subsequent water oxidation reaction.[9,11] Itoh and Bockris observed negligible photocurrent for water oxidation with hematite electrodes >20 nm. They attributed this to the fact that in the sufficiently thin films, the diffusion length for electrons from the SnO_2 layer extends into the hematite film, causing enhanced recombination.[13,14] Liang *et al*. attributed the poor water oxidation efficiency with hematite to the enhanced recombination at the trap states in the substrate–hematite interface.[15] Souza et al. studied the influence of the film thickness on water oxidation on nanostructured hematite films prepared by spin coating.[16] Significantly lower photocurrent was observed for thinner electrode, which was attributed to the enhanced electron-hole recombination at the intermediate states close to the conduction band as a result of stress induced by the interaction of the film and the substrate.[16] Le Formal *et al*. attributed the dead layer effect to the lack of crystallinity and enhanced recombination sites at the hematite-substrate interface.[11] Sivula, Grätzel and co-workers studied the PEC water oxidation on ultrathin hematite electrode prepared by APCVD and spray pyrolysis.[11,17] They attributed the significantly lower photoactivity for thinnest films to increased recombination at the FTO–hematite interface due to the formation of the dead layer.[11]

Efforts to mitigate the dead layer effect have primarily consisted of modifying the TCO substrate with oxide underlayers. Incorporation of 5 nm SnO_2 underlayer, or Si doping, was shown to enhance the PEC water oxidation with hematite thin films.[15] A similar effect was also demonstrated with a monolayer of SiO_2.[11] Subsequently Hisatomi *et al*. studied the water oxidation with ultrathin hematite films prepared by spray pyrolysis and suggested that the dead layer, which results from strains and lattice mismatch, can be mitigated by a Ga_2O_3

underlayer.[10] In a subsequent report, similar enhancement were observed for ultrathin hematite films with either 2 nm of Nb_2O_5 or TiO_2 underlayers.[18] The effect of Nb_2O5 and TiO_2 underlayers, however, was attributed to a different effect, i.e. suppressing electron back-recombination from the FTO to the hematite valence band holes.

Although substantial improvement in the water oxidation efficiency with hematite ultrathin films has been achieved by the incorporation of oxide underlayers, the specific physical effect of oxide underlayers has not been unambiguously determined. Understanding the performance limiting processes in ultrathin films is crucial to fully exploit the potential benefits of TFA approach. This work is aimed at acquiring a clearer picture of the dead layer as well as the effects of oxide underlayers. We present an investigation of PEC water oxidation and structural characterization of hematite ultrathin films with and without oxide underlayer. We utilize atomic layer deposition (ALD) to synthesize thin films of hematite electrodes with controlled geometry and composition as well as for the deposition of the underlayers. Ultrathin films of hematite prepared *via* ALD are pinhole free, enabling the uniform and conformal coverage of the underlying substrate. Uniformity and simple geometry of these planar thin films, therefore, serve as excellent model systems to probe the effect of the of oxide underlayers. We further compare the PEC behavior of the hematite electrodes of different thicknesses with and without a variety of metal oxide underlayers under water oxidation conditions. A combination of systematic photoelectrochemical, spectroscopic and microscopic measurement allowed us to clearly determine the factors enabling H_2O oxidation improvement through incorporation of oxide underlayer and elucidate the origin of the dead layer.

2.3 Experimental

2. 3.1 Electrode preparation

Thin films of Fe_2O_3 were deposited on fluorine-doped tin oxide (FTO)-coated glass substrates (Hartford Glass, 15 Ω cm^{-2}) by atomic layer deposition, ALD (Savannah 100, Cambridge Nanotech Inc.), using the procedure described previously.[9,19,20] Briefly, the FTO glass was cleaned by sequential sonication in soap, water and isopropyl alcohol. Fe_2O_3 was deposited onto the cleaned FTO substrate by alternating pulses of ferrocene as iron precursor and a combination of water and ozone as oxidant. The ferrocene cylinder, heated to 70 °C, was pulsed for 20 s and was followed by an oxidation cycle which included 10 sub-cycles of a 0. 015 s H_2O pulse followed by a 2 s ozone pulse, where each sub-cycle was separated by a 5 s purge. Ga_2O_3 was deposited on FTO by ALD using tris(dimethylamido)gallium (III) ($Ga_2(NMe_2)_6$) (Strem Chemicals Inc.) as Ga precursor and H_2O as oxidant using a modified version of previously reported percedure.[21] For the Ga_2O_3 deposition, the precursor cylinder was heated to 150 °C and pulsed for 0.2 s under exposure mode for 8 s, followed by 12 s purge. Then a 0.015 s pulse of H_2O was introduced using the same exposure-purge time to oxidize the Ga precursor. A growth rate of 1.1 Å Ga_2O_3 / cycle was measured by ellipsometry on witness Si wafer. As deposited Ga_2O_3 on FTO substrate was subsequently coated with a desired thickness of Fe_2O_3. After the deposition of Fe_2O_3, films were annealed by heating to 500 °C at a rate of 17 °C /min, sintered at 500 °C for 2h min, and allowed to cool to room temperature over 2 h. Nb_2O_3 was deposited on FTO by ALD using Nb(V) ethoxide ($Nb(OCH_2CH_3)_5$) (Sigma Aldrich) as Nb precursor and H_2O as oxidant. For the Nb_2O_5 deposition, Nb cylinder was heated to 150 °C and pulsed for 0.2 s. After 8 s exposure, the chamber was purged for 12 s. The same exposure/purge time was

used for the oxidant, water. The ALD chamber temperature was set at 200 °C for Nb_2O_5 deposition. WO_3 was deposited using bis(tert-butylimino)bis(dimethylamino)tungsten(VI) (Sigma Aldrich) as precursor and H_2O as oxidant. Briefly, the W cylinder was heated to 75 °C and pulsed for 2 s. After 10 s exposure, the chamber was purged for 10 s. The same exposure/purge time was used for the oxidant, water. The ALD chamber temperature was maintained at 260 °C for WO_3 deposition. SnO_2 was deposited using $Sn(NMe_2)_4$ (Sigma Aldrich) as ALD precursor and ozone as oxidant. The Sn precursor cylinder was heated to 60 °C and pulsed for 0.5 s followed by 10 s purge. 12 s O_3 pulse was used to as oxidant followed by 10 s purge. The ALD chamber temperature was maintained at 230 °C for SnO_2 deposition. Indium tin oxide (ITO)-coated glass substrates (SPI supplies, 8-12 $\Omega\,cm^{-2}$) were used as analogues of an ITO underlayer substrate.

2.3.2 Film characterization

X-ray photoelectron spectroscopy (XPS) measurements were performed at Molecular Materials Research Center in the Beckman Institute at the California Institute of Technology using a Kratos Axis Ultra system with a base pressure of $<1\times10^{-9}$ Torr. A monochromated Al kα source was used to illuminate the sample with 1486.7 eV photons at a power of 150 W. A hemispherical analyzer oriented for detection along the sample surface normal was used. Survey scans were obtained at a resolution of 1 eV with a pass energy of 80 eV. Detailed scans were acquired at a resolution of 25 meV with a pass energy of 10 eV using variable acquisition times. For depth profiling studies, an octopole ion gun was used to etch the sample surface with 500 eV Ar ions for 180 s per step.

The surface morphology of the prepared films was examined by scanning electron microscopy, SEM (Carl Zeiss Auriga, Dual Column FIBSEM). Absorbance measurements

were made using a Perkin-Elmer Lambda35 UV-vis spectrometer with a Labsphere integrating sphere. The absorbance spectra of the films were measured by illuminating from the substrate-electrode interface. The incident light was corrected for passing through and being reflected by the substrate using a previously reported approach.[19] Raman spectroscopy measurements were made LabRam Aramis, Horiba Jobin Yvon instrument equipped with 532 nm laser.

2.3.3 Photoelectrochemical measurements

For photoelectrochemical measurements, electrodes were masked with a 60 μm Surlyn film (Solaronix) with a 0.28 cm^2 hole to define the active area and to prevent scratching of the thin films. Surlyn films were adhered to the electrodes by heating to 115 ℃. The electrodes were examined in contact with aqueous solutions buffered to pH 6.9 using a 0.1 M phosphate buffer, with 200 mM KCl as a supporting electrolyte. A homemade saturated Ag/AgCl electrode and high surface area platinum mesh were used as reference electrode and counter electrode, respectively. The reference electrode was regularly calibrated vs. saturated calomel electrode (SCE) (Koslow Scientific) and all potentials were converted to the reversible hydrogen electrode (RHE) scale by the equation $V_{RHE} = V_{Ag/AgCl} + 0.197\ V + pH\ (0.059\ V)$. Photoelectrochemical measurements were made with an Eco Chemie Autolab potentiostat coupled with Nova electrochemical software. For the current-potential measurements, potential was cycled linearly between 0.0-1.6 V *vs*. Ag/AgCl at the rate of 20 mV s^{-1}. The light source was a 450 W Xe arc lamp (Horiba Jobin Yvon). An AM 1.5 solar filter was used to simulate sunlight at 100 mW cm^{-2} (1 sun). Unless otherwise stated, all photoelectrochemical tests were carried out by shining light on the electrodes through the FTO substrate (back illumination). For back illumination electrodes were clamped to a

custom made glass electrochemical cell. For the front side illumination (electrolyte side) a homemade cell with high optical quality quartz window was used.

2.4 Results and discussion

Figure 2.3 shows the current density-potential (*J-V*) curves of 18 nm hematite electrodes prepared *via* ALD (equivalent of 300 ALD cycles) and deposited on bare and Ga_2O_3 modified FTO substrates. Consistent with previous reports, [11,18] ultrathin films of hematite demonstrated negligible photocurrent due to the dead layer effect and associated high rate of electron-hole recombination. The dramatic shift in the photocurrent onset potential along with enhanced photocurrent indicates the superior charge transport properties of Ga_2O_3 modified film compared to the unmodified electrodes. Since thicker hematite films, as discussed in detail below, were well-behaved when deposited on the same FTO substrates, a trivial cause of the poor performance of defective (e.g. non-conductive) substrates can be ruled out.

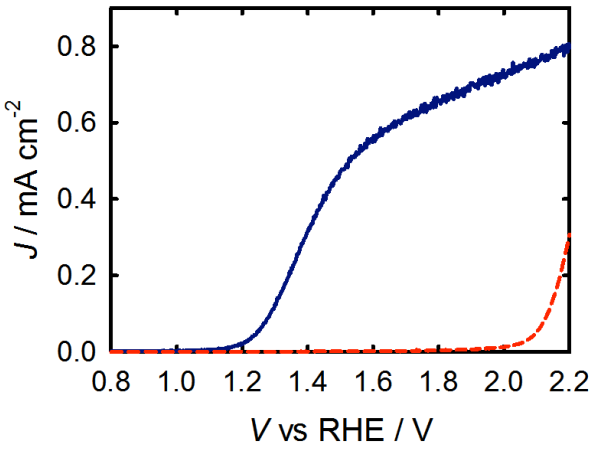

Figure 2-3. *J-V* curves of 18 nm thick hematite electrodes deposited on bare FTO (dashed red) and FTO substrate modified with a 2 nm Ga_2O_3 underlayer (solid dark blue) in response to 1 sun illumination. Dark *J-V* curves are provided in the appendix, Figure A2-1.

A Ga_2O_3 underlayer can improve the PEC water oxidation with hematite in several different ways. Cesar *et al*.,[17] and Itoh and Bockris[13,14] attributed the poor water oxidation performance of hematite thin films to the increased recombination rate at the hematite/FTO interface. They suggested that possible mixing of SnO_2 and Fe_2O_3 at the hematite/FTO interface could induce trap states, enhancing electron–hole recombination at the back contact. In principal Ga_2O_3 underlayer can act as a diffusion barrier layer and block Fe and Sn inter-diffusion during film preparation and annealing. Therefore, the performance enhancement can be a result of less significant mixing at the hematite-FTO interface in the presence of Ga_2O_3 underlayer. In order to control for this possibility, samples of hematite deposited on Ga_2O_3 modified and bare FTO, were prepared and characterized by XPS depth profiling measurements. The effect of Ga_2O_3 underlayer was examined by comparing the XPS depth profile of films treated at different temperatures deposited on FTO and Si substrates. As seen in Figure 2-4, substantial overlap between the profiles of different atomic concentrations can be seen in every case. Since the escape depth of photoelectrons is on the order of 2 - 10 nm, part of the overlap can be attributed to signal from the underlying material. Unfortunately this overlap makes it difficult to accurately determine the extent of elemental diffusion at the hematite/FTO interface. However, a relative comparison can be made of the films deposited on FTO and Si substrates, since no diffusion of Fe or Sn is expected into the Si substrate. For example, by comparing the Fe profile in a hematite film deposited on FTO (Figure 2-4a) and on SnO_2 coated Si substrate (Figure 2-4b), substantial mixing of Fe_2O_3 and SnO_2 is evident. For hematite films deposited on SnO_2 coated Si substrates, the Fe profile declines to zero after ~30 min sputtering time, while for the same

hematite film thickness on FTO, the Fe profile showed non-zero values throughout the underlying FTO layer. Since no Fe was detected in bare FTO substrate, there is apparently substantial mixing Fe and/or Sn at the substrate interface. In the presence of a Ga_2O_3 underlayer, however, nominally identical atomic profiles were observed for Fe, with Fe signals persisting past the Ga signal as shown in Figure 2-4c. Thus the improvement in water oxidation performance upon underlayer incorporation cannot be associated to the mitigation of diffusion effect at the back contact by the Ga_2O_3 layer. In other words, the dead layer is clearly not a result of elemental mixing at hematite-substrate interface. We note that the mixing at the FTO/hematite interface was also observed by Kronawitter *et al*. for hematite thin film through soft X-ray absorption measurements.[22] The interface was found to be associated with a distribution of unoccupied oxygen p-hybridized states located below the conduction band, which are eliminated with high-temperature annealing.

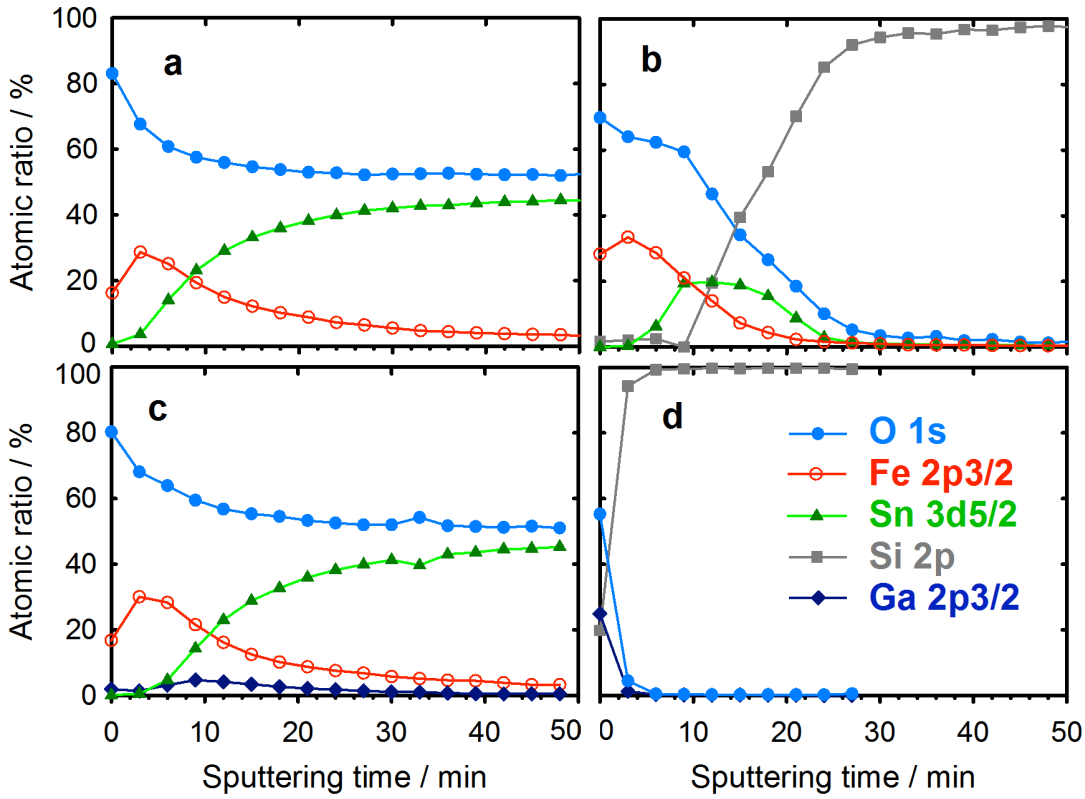

Figure 2-4. XPS depth profile of 18 nm Fe_2O_3 deposited on FTO. b) The same thickness of Fe_2O_3 on a SnO_2 coated Si wafer. c) The profile of 18 nm Fe_2O_3 with 2 nm Ga_2O_3 underlayer deposited on FTO. d) The profile of 2 nm Ga_2O_3 deposited on Si wafer.

In addition, from Figure 2-4c it can be seen that Ga profile shows nonzero values over a wide range of sputtering time extended into the Fe_2O_3 and SnO_2 layers. Comparing this profile to that of the same thickness of Ga_2O_3 deposited on Si (Figure 2-4d), where the Ga concentration declines to zero within 3 min of sputtering, shows that there is substantial Ga diffusion into the adjacent Fe_2O_3 and SnO_2 layers. Therefore, control experiments were performed to examine the possible doping effect of Ga in hematite. For this purpose, 300 ALD cycle hematite electrodes were doped with Ga by alternating ALD cycles of Fe_2O_3 and Ga_2O_3 and examined under water oxidation conditions. The amount of Ga doping was taken

as the equivalent of 2 nm Ga_2O_3, i. e. 18 ALD cycles (1 cycle of Ga_2O_3 after each 16 cycles of Fe_2O_3). Negligible photocurrent was observed for Ga doped hematite compared to the electrode with Ga_2O_3 underlayer (Figure A2-2 in the appendix). In addition, *J-V* curves of hematite electrodes having 1, 2 and 4 nm Ga_2O_3 underlayers (Figure A2-3) showed an optimum Ga_2O_3 underlayer thickness of 2 nm. While an effect from doping is also expected for the 1 and 4 nm Ga_2O_3 underlayers, the water oxidation efficiency was significantly lower with these thicknesses of the underlayer. These combined results rule out any significant contribution from Ga doping.

Itoh and Bockris also suggested that when the hematite film is sufficiently thin, the diffusion length of electrons from the underlying SnO_2 substrate extends over a greater portion of the hematite film, causing enhanced electron-hole recombination.[13] Similar conclusion was made by Hisatomi *et al*. and it was suggested that this electron back recombination can be blocked by 2 nm of Nb_2O_5 or TiO_2 underlayers.[18] This electron-blocking effect is also possible for Ga_2O_3, due to the conduction band energy offeset.[23] However, it is not trivial to define electronic bands for a material that is only 2 nm thick and highly mixed with adjacent SnO_2 and Fe_2O_3 layers. In any case, to address this possibility, we note that hematite is already highly doped and bulk electron-hole recombination is generally limited by the rate of hole trapping.[52] Therefore, increasing the number of electrons should have a negligible effect on the recombination rate. It is therefore unlikely that the underlayer improve the performance of hematite thin films by reducing recombination with FTO electrons.

Another possible role of an underlayer is increasing the concentration of photogenerated charge carriers due to an increase in the electrode thickness, e.g. increasing

the growth rate of Fe_2O_3, an increase in the absorptivity, α, or band gap reduction. To address these possibilities, absorption measurements were performed of films with and without Ga_2O_3 underlayer. Figure 2-5 shows the absorptance spectra of 18 and 60 nm hematite films, with and without a Ga_2O_3 underlayer. No significant contribution in visible light absorption was observed for 2nm Ga_2O_3 (Figure A2-4). Interestingly, the absorptance of the film deposited on Ga_2O_3 underlayer was significantly higher with more pronounced absorption peaks at ~530 and 400 nm. The absorption spectrum and onset matched that of unmodified hematite film, however, indicating no changes in the hematite band gap or major electronic transitions by the Ga_2O_3 underlayer. A larger absorptance was also observed for 60 nm films with a Ga_2O_3 underlayer, however the extent of the absorptance increase was lower compared to 18 nm films. Thus, at least part of the improved performance of hematite electrodes with a Ga_2O_3 underlayer can be attributed to increased light absorption. The increased light absorption must be due to an increased hematite film thickness and/or increased absorptivity. A plot of the absorbance spectra of 18 nm electrodes with and without a Ga_2O_3 underlayer is shown in the appendix, Figure A2-5. The absorbance at 550 nm is 0.202 and 0.105 for the films with and without a Ga_2O_3 underlayer, respectively. Assuming the same absorption coefficient of 8×10^4 cm^{-1} at this wavelength,[24] the thickness of the film with the underlayer must be about twice as much. Therefore, if the increased absorption is simply due to an increased thickness, it should be clearly observable by ellipsometry as well as from the XPS depth profiles. Identical thicknesses were measured however, by ellipsometry for 300 ALD cycles hematite deposited on bare and Ga_2O_3 coated FTO indicating no growth rate change for Fe_2O_3 deposition on Ga_2O_3 surface. The relative thicknesses were also compared from XPS depth profiling measurements of films

containing 400 ALD cycles hematite grown on Si wafers with and without a Ga_2O_3 underlayer. Similar profiles of Fe were observed in both cases which indicates that the thicknesses of Fe_2O_3 are nominally the same (Figure A2-6). Any small difference in thickness, within experimental error of this measurements, cannot account for the large difference in the film absorbances. Thus, the increased light absorption is due to an increased absorptivity.

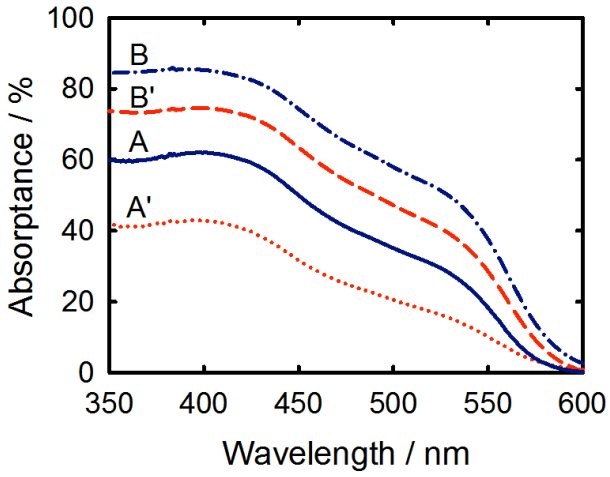

Figure 2-5. a) Absorptance spectra of 18 nm hematite film with (A) and without (A') a Ga_2O_3 underlayer. B and B' curves correspond to a 60 nm films with and without a Ga_2O_3 underlayer, respectively.

Interestingly, a noticeable change in the color of the hematite electrodes deposited on Ga_2O_3 underlayers observed after annealing (Figure 2-6) which was in contrast to the hematite films deposited directly on FTO. Absorption measurements of hematite films were therefore carried out for hematite films with and without a Ga_2O_3 underlayer films both before and after annealing at 500 °C. The absorptance spectra of 18 nm hematite film deposited on bare and Ga_2O_3 coated FTO are shown in Figure 2-6. Interestingly, the higher absorptance and clear absorption peaks only appear after annealing for the films with a

Ga_2O_3 underlayer. We note that crystalline hematite (α-Fe_2O_3) generally forms after annealing at temperatures ~500 °C or higher.[19] Below this temperature, amorphous (or partially crystalline) Fe_2O_3 is the dominant component of films prepared *via* ALD. This is consistent with the spectral profile of the un-annealed films which clearly show characteristics of an amorphous phase, with no well-defined transition peaks. After annealing, however, the absorption onset and electronic transition responsible for indirect and direct transitions of hematite can be clearly distinguished at ~530 and 400 nm, respectively.[25,26] Similar absorption properties were observed for 18 nm hematite films with an Nb_2O_5 underlayer under similar conditions (Figure A2-7). Higher absorptivity and was also observed for hematite films annealed at elevated temperatures by Pailhé *et al*. which attributed to the larger crystallite size.[27] It was found that larger crystallite size allow structural relaxation from octahedral to C_{3v} like symmetry, which in turn alters the optical transition properties manifested as increased absorptivity of the films. The same correlation between the size of the crystallites and absorptivity was also observed by Sivula *et al*. for mesoporous hematite films annealed at various temperatures.[28] Therefore, the increased absorptivity for the hematite films with a Ga_2O_3 underlayer, which correlates with the larger grain size (see below), is attributed to the same effect.

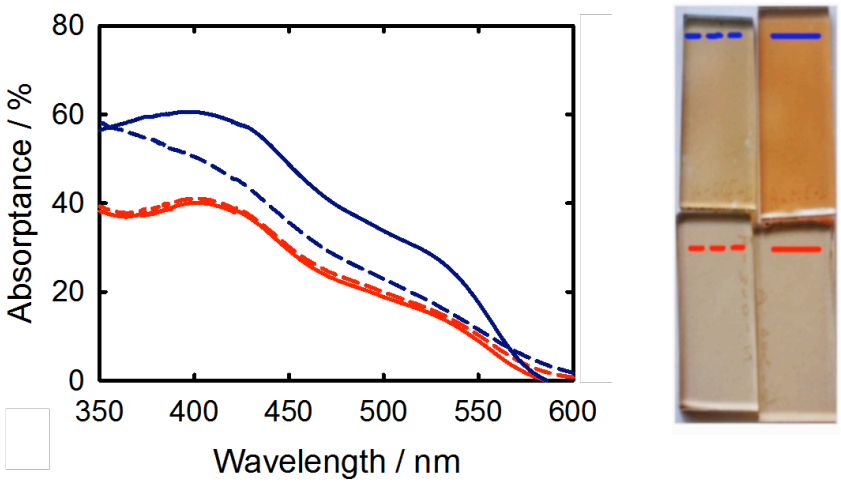

Figure 2-6. Absorptance spectra of 18 nm hematite films with (dark blue) and without (red) Ga_2O_3 underlayer before (dashed lines) and after (solid lines) annealing in 500 °C.

As can be seen in Figure 2-7a, in the case if sufficiently thick films, the Ga_2O_3 underlayer not only did not improve the water oxidation performance, but also reduced the plateau photocurrent significantly. We note that lower photocurrent at higher hematite thicknesses with oxide underlayer was also observed by Hisatomi and co-workers who attributed it to a lower electron extraction efficiency as a result of the electron-blocking effect of the oxide underlayer.[48] The lower photocurrent however, can be due the increased absorptivity discussed above; i.e. since more light is absorbed near the substrate, fewer holes are generated in the depletion region near the electrolyte interface when electrodes are illuminated from the substrate side (back illumination). As discussed in the previous chapter, holes generated outside of the ~20 nm depletion region undergo recombination and do not contribute to the water oxidation photocurrent.[19] If a stronger absorbance is the cause of the lower plateau photocurrent of the 60 nm films, illuminating the electrodes for the front side (electrolyte side) should overcome this and produce an essentially identical *J-V* response. These situations are schematically shown in Figure 2-8. Figure 2-7b clearly shows

that indeed this is the case and the *J-V* curves of the front illuminated 60 nm electrodes with and without a Ga_2O_3 underlayer are nominally identical. This also corroborates with the assignment of the Ga_2O_3 underlayer effect to be primarily increasing the absorptivity of hematite thin films.

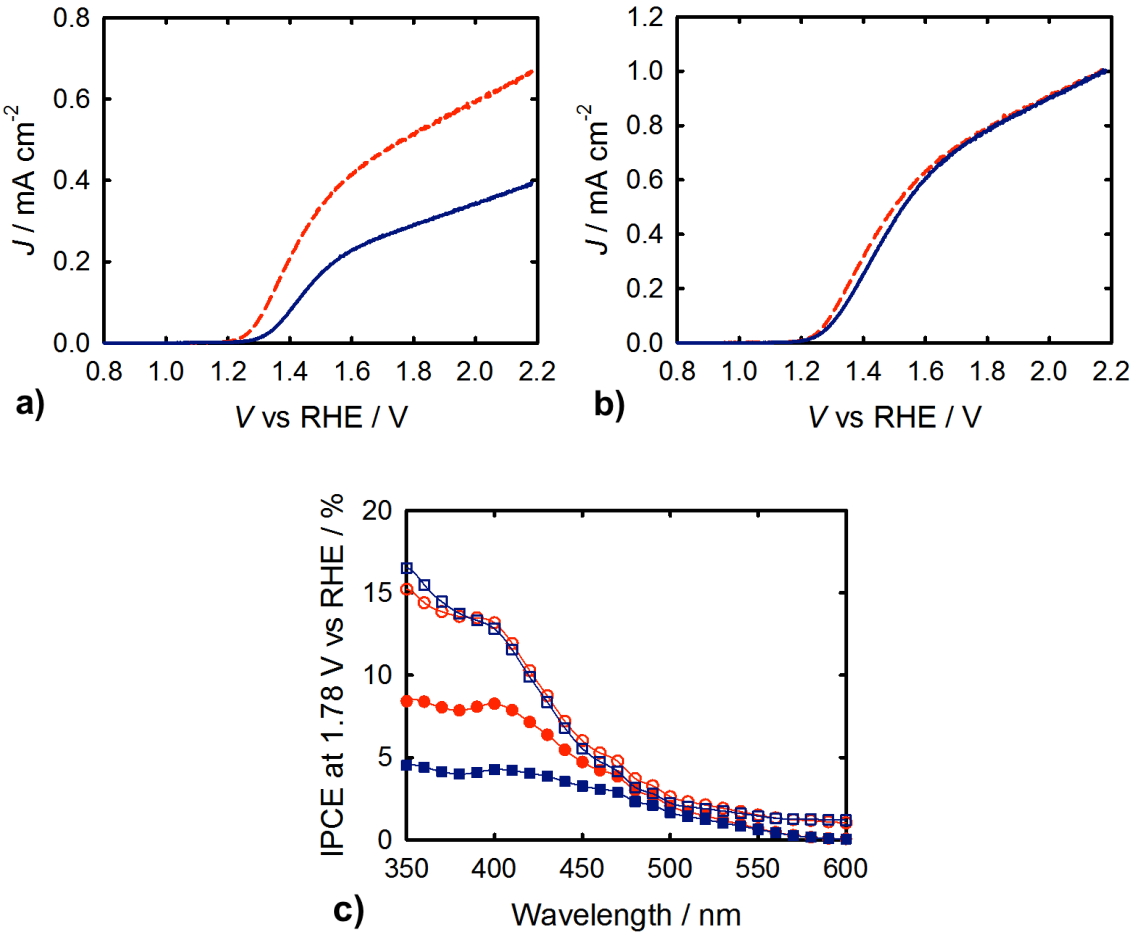

Figure 2-7. *J-V* curves and IPCE of 60 nm hematite electrodes with (dark blue) and without (red) a Ga_2O_3 underlayer under back side (substrate side) (a) and front side (electrolyte side) illumination (b). c) IPCE values of the same electrodes measured under front side (opens shapes) and backside (solid shape) illumination direction.

This situation should result in the spectral response due to differences in light penetration depths. The incident photo-to-current efficiency (IPCE) measurements (Figure

2-7c) clearly showed that the shorter wavelengths contribute less to the photocurrent when illuminated from the substrate side compared to the electrolyte side. The red wavelengths with longer penetration depth are only minimally affected by the illumination direction. These combined results confirm our assignment of increased absorptivity as a primary effect of the underlayer on the optical properties of hematite thin films.

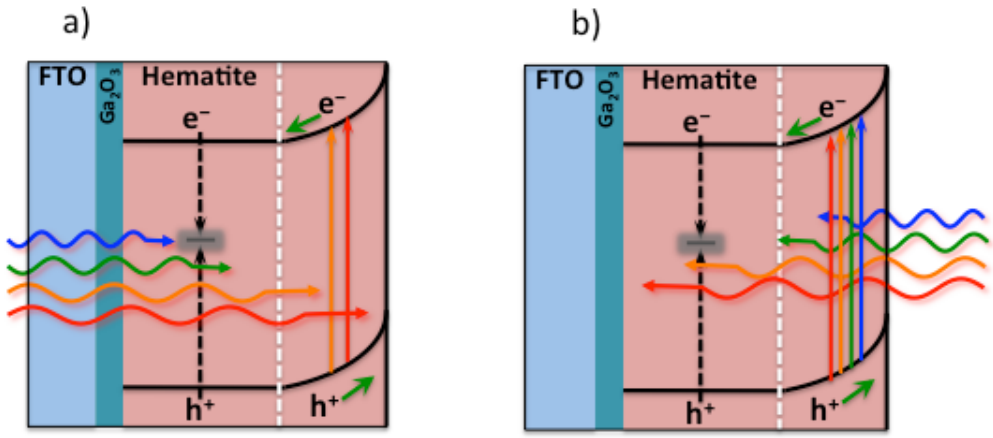

Figure 2-8. Schematic electronic transitions of 60 nm hematite electrodes under back side (a) and front side (b) illumination directions. Short wavelengths contribute less to the photocurrent when illuminated from the backside as photogenerated hole are created outside of the hole collection length.

In addition to an increased absorptivity, absorption peaks at ~530 and 400 nm of the hematite film with an underlayer were more prominent as seen in Figure 2-6. These observations are consistent with a more ordered structure and atomic arrangement, i.e. an increased crystallinity of the films deposited on Ga_2O_3 as others have suggested.[10] Raman spectroscopy was utilized to examine the crystallinity of the hematite thin films. Raman spectroscopy has been utilized extensively to investigate amorphous to crystalline phase transitions, oxygen defects, stress states and quantum size effects in metal oxides.[29–34]

Raman spectra provide not only the basic structural information but also subtle spectra alterations, such as the line shape and full width at half maximum (FWHM) of Raman peaks, can be used to evaluate crystalline quality of nanostructures.[29,34–36] Crystalline quality can be described in term of correlation length, which is defined as the average size of the material homogeneity region corresponding to the actual grain size, average distance between defects, or grain boundaries. So-called phonon confinement (PC) effects are often used to explain the correlation length and quality of the crystalline medium.[29,31,34] PC effects describe the phenomena that occur when the phonon momentum selection rule is deviated. This generally happens when the dimension of ordered crystal domains become very small and manifests as both frequency shift and asymmetrical broadening of the Raman bands.[29,31,34]

A Raman spectrum of a 60 nm hematite film deposited on FTO is shown in Figure A2-8. The Raman spectrum of hematite is distinct from that of other iron oxide phases.[31,32,35,37,38] Seven Raman bands at 222, 239, 286, 403, 488, 600 and 1300 cm^{-1} can be clearly resolved, which match quite well with the reported values for hematite in literature and that of a reference hematite sample.[31,32,35] Four major Raman phonon modes of 18 nm hematite thin films with and without a Ga_2O_3 underlayer are shown in Figure 2-9. Interestingly, the Raman spectra match the absorption measurements discussed above; i.e. as deposited film on Ga_2O_3 underlayer were primarily amorphous which produced more intense and sharper Raman peaks after annealing. Annealing had a negligible effect on the Raman spectra for the films without an underlayer. The FWHM for the peak at 288 cm^{-1} was found to be 12.40 and 27.97 cm^{-1} for the annealed films with and without the Ga_2O_3 underlayer, respectively. The asymmetric broadening along with a subtle blue shift of the peaks was also observed for

the hematite film without an underlayer. Peak broadening and frequency shifts have been extensively observed for TiO_2 nanocrystals and hematite thin films which have been attributed to phonon confinement, internal stress and nonstoichiometry.[29,32,35] In our films, since the preparation condition was strictly the same for electrode with and without underlayer, the effects of impurities and non-stoichiometry are unlikely which we rule out. Therefore we attribute the peak shift and broadening to the lower crystallinity and smaller crystallite size for hematite films deposited on bare FTO. The high resolution SEM images of 18 nm hematite films deposited on bare FTO and on a Ga_2O_3 underlayer (Figure 2-10) strongly support this assignment. Thin films of hematite deposited on a Ga_2O_3 underlayer exhibit significantly larger grain sizes along with more ordered structure compared to the film without the underlayer. An SEM image of a hematite film with an Nb_2O_5 underlayer is shown in Figure A2-7, indicating identical effect. We note that this assignment is consistent with the absorption spectra in Figure 2-6, i. e. more pronounced peaks and increased absorptivity correlates with the larger grain size for hematite films deposited on a Ga_2O_3 underlayer as observed by others.[27,28]

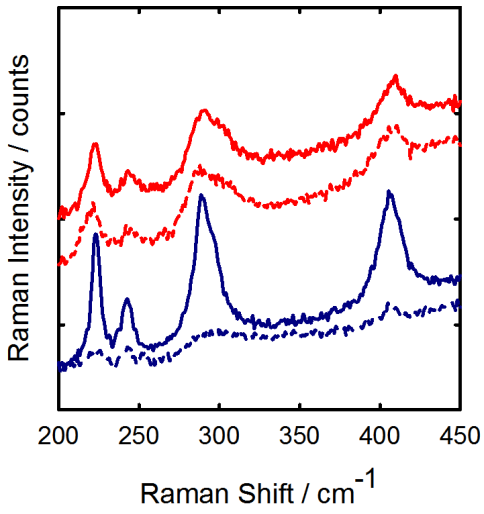

Figure 2-9. Raman spectra of four major hematite phonon modes of 18 nm hematite films with (dark blue) and without (red) Ga_2O_3 underlayer before (dashed lines) and after (solid lines) annealing.

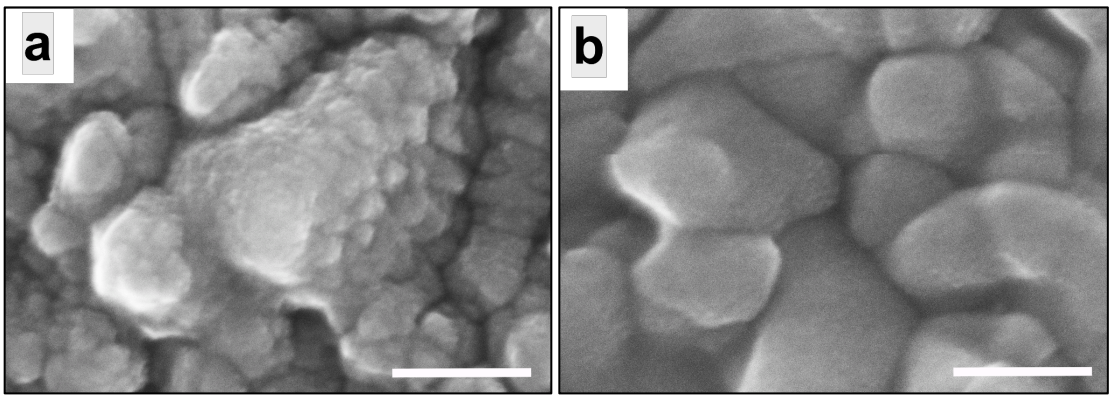

Figure 2-10. SEM images of 18 nm hematite deposited on bare FTO (a) and Ga_2O_3 modified FTO (b) substrates. The scale bar is 100 nm.

Another interesting comparison is the effect of different oxide underlayers which have been reported to improve the water oxidation performance of hematite thin films.[6,18] Figure 2-11a shows the Raman spectra of 18 nm hematite films deposited on bare FTO and three different oxide underlayers including Ga_2O_3, Nb_2O_5, WO_3, as well as an ITO-coated glass

substrate. The *J-V* curves of hematite films deposited on each of these underlayers, and directly on FTO, are shown in Figure 2-11b. Clearly all of the oxide underlayers improve the water oxidation performance, however to different extents. Interestingly the intensity and sharpness of the Raman bands can be correlated to the improvement in the photocatalytic activity of the corresponding electrodes. The effect of the ITO and WO_3 underlayers on the *J-V* curves is less significant compared to the Ga_2O_3 and Nb_2O_5 underlayers. The Raman spectra of the films with WO_3 or ITO also show a subtle broadening and peak shift compared to the corresponding films with either Ga_2O_3 or Nb_2O_5 Underlayers. In addition, each of these underlayers produced an enhanced absorbance, with the spectra shown in Figure 2-11c. FWHM extracted from the Gaussian fit of the Raman spectra indicated a strong correlation between the Raman line shapes, increased absorptivity and the observed PEC activity (See Figure A2-9). These results are all consistent with our assignment of increased crystallinity as being the primary beneficial effect of underlayers.

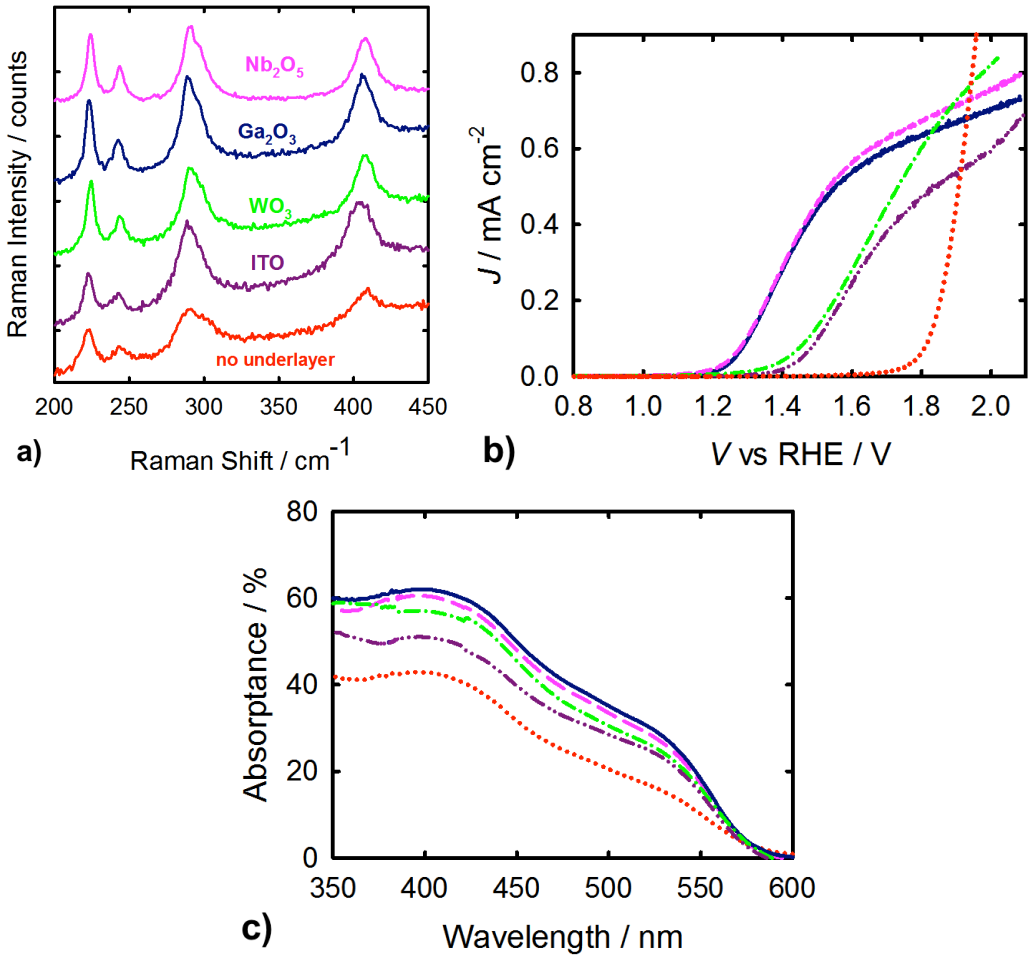

Figure 2-11. a) Raman spectra of 18 nm hematite films on bare FTO and on different 2 nm thick oxide underlayers. Corresponding *J-V* curves (b) and absorptance spectra (c) of the same films.

2.5 Conclusion

The study presented herein shed light on the fundamental origin of the poor water oxidation performance of very thin hematite films, the origin of the dead layer, and the primary effect of metal oxide underlayers. The hematite films deposited on bare FTO exhibit poor crystallinity with small crystallite domains. This could result in a high density

of defects and grain boundaries, which may increase the rate of recombination near the back contact. An amorphous, or low crystallinity, region at the interface would also diminish the already low mobility of minority carriers which would prevent efficient charge transport. The effects of increased recombination and decreased mobility for the very thin films that are relevant here are difficult to separate, however we note that both effects are likely and would greatly diminish the water splitting performance. Once the thickness of the hematite films increases beyond the dead layer region, with a critical thickness ~20 nm, the film crystallinity increases which results in an improved water oxidation performance, as discussed above for 60 nm films. In order to realize the TFA strategy of making nanostructured electrodes, it is optimal to only make electrodes as thick as the collection length. Thus, it is crucial to not only understand the limitations of very thin electrodes, but to establish methods to overcome them. We demonstrated that Ga_2O_3 and Nb_2O_5 are promising oxide underlayers that enable the deposition of highly crystalline hematite films with the average crystallite size of ~ 3 times larger that of the films deposited on bare FTO according to SEM images. The increased crystallinity manifests as an increased correlation length of the crystalline medium, which results in the sharper Raman peaks. In addition, the increased crystallinity results in stronger light absorption with more defined transition peaks. It is further expected that such an increased crystallinity would improve the hole mobility which would result in a higher charge collection efficiency.

APPENDIX

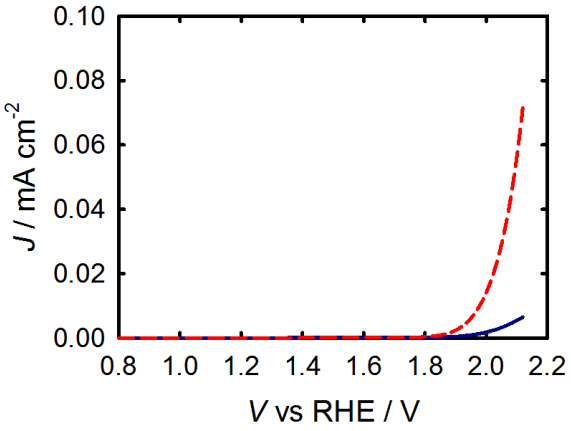

Figure A2-1. *J-V* curves of 18 nm hematite electrodes with (solid dark blue) and without (dashed red) Ga_2O_3 underlayer, under water oxidation condition in dark.

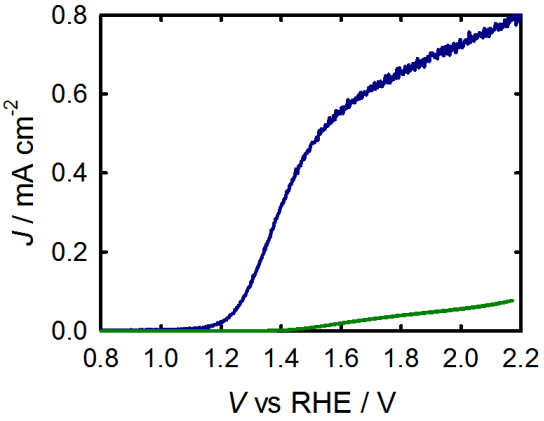

Figure A2-2. *J-V* curves of 18 nm hematite electrodes with 2nm (18 ADL cycles) Ga_2O_3 underlayer (dark blue) and the same thickness of hematite without underlayer but doped with the same ALD cycles of Ga_2O_3 (green).

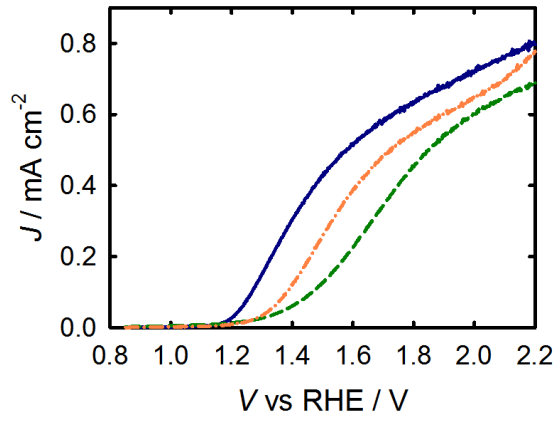

Figure A2-3. *J-V* curves of 18 nm hematite electrodes with 1 (dash-dotted orange), 2 (solid dark blue) and 4 nm (dashed green) Ga_2O_3 underlayer, under water oxidation condition and 1 sun illumination.

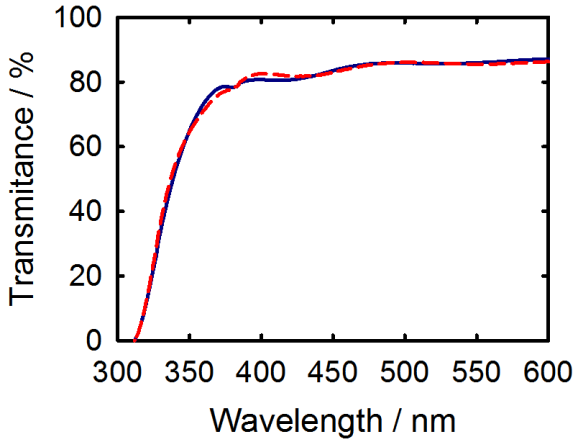

Figure A2-4. Transmittance of FTO (dashed red) and FTO coated with 2 nm Ga_2O_3 (solid dark blue).

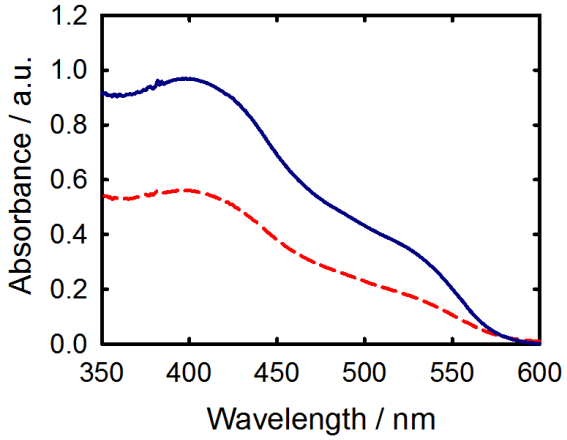

Figure A2-5. Absorbance spectra of 18 nm hematite with (solid dark blue) and without (dashed red) a Ga_2O_3 underlayer.

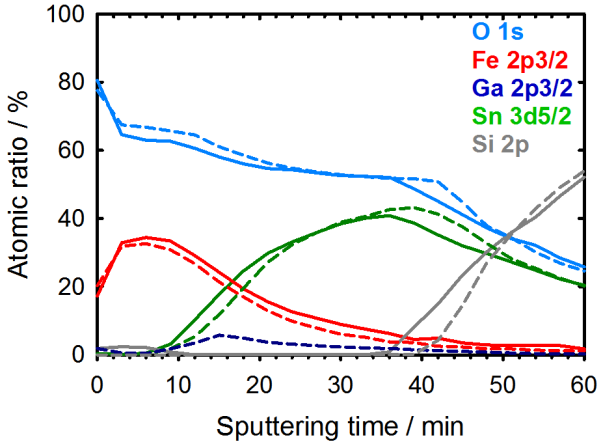

Figure A2-6. XPS depth of hematite films with (dashed lines) and without (solid lines) Ga_2O_3 underlayer deposited on SnO_2 coated Si wafer.

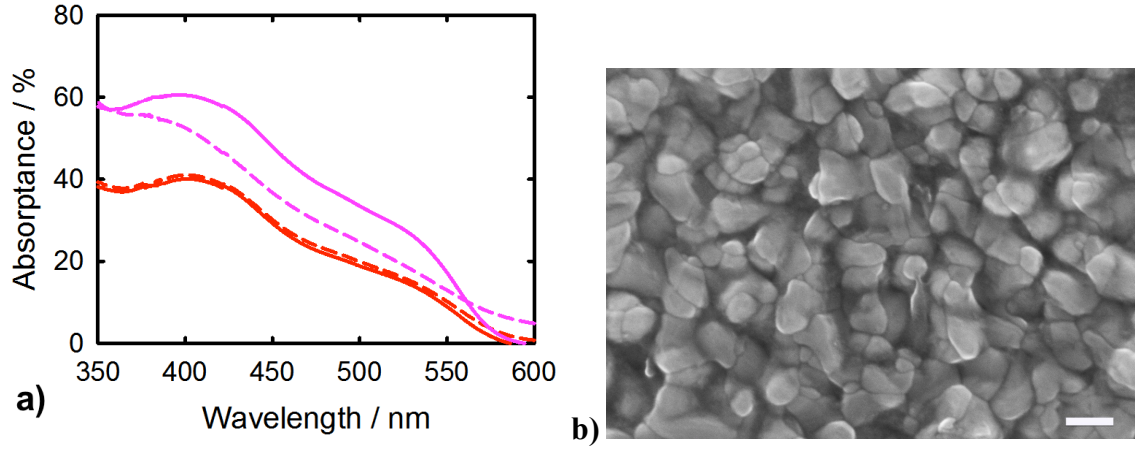

Figure A2-7. a) Absorptance spectra of 18 nm hematite films with (pink) and without (red) Nb_2O_5 underlayer before (dashed lines) and after (solid lines) annealing in 500 °C. b) SEM images of 18 nm hematite on FTO with 2 nm Nb_2O_5 underlayer. Scale bar is 100 nm.

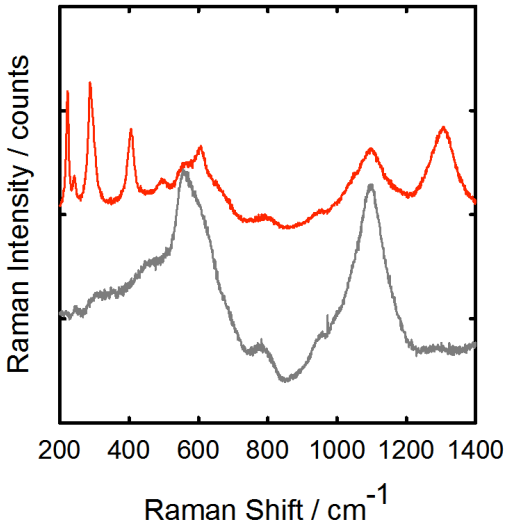

Figure A2-8. Raman spectrum of a 60 nm hematite (red) film deposited on FTO overlaid with that of the FTO substrate (grey).

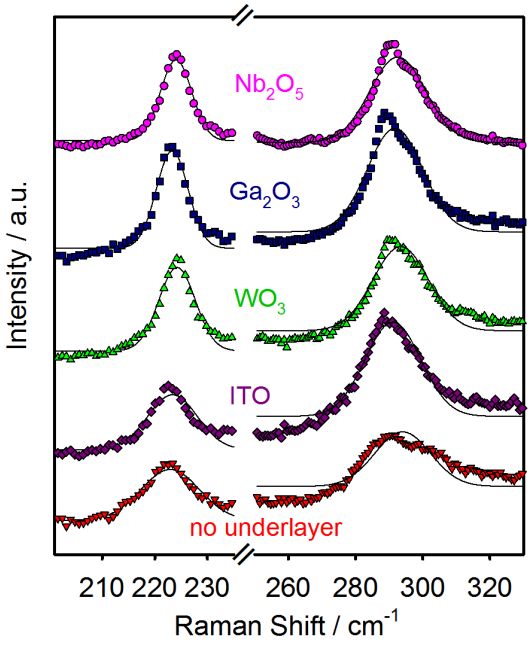

Substrate	Nb_2O_5	Ga_2O_3	WO_3	ITO	FTO
FWHM / cm^{-1} (Peak at 223 cm^{-1})	4.96	5.03	5.83	7.86	9.30
FWHM / cm^{-1} (Peak at 288 cm^{-1})	12.20	12.40	14.30	15.15	27.97

Figure A2-9. Experimental and Gaussian fit of two Raman phoneme modes for 18 nm hematie films deposited on different underlayers. A table of calculated FWHM values is also shown.

REFERENCES

REFERENCES

(1) Mohapatra, S. K.; John, S. E.; Banerjee, S.; Misra, M. *Chem. Mater.* **2009**, *21*, 3048.

(2) Wen, X.; Wang, S.; Ding, Y.; Lin Wang, Z.; Yang, S. *J. Phys. Chem. B* **2005**, *109*, 215.

(3) Kay, A.; Cesar, I.; Grätzel, M. *J. Am. Chem. Soc.* **2006**, 15714.

(4) Sivula, K.; Zboril, R.; Le Formal, F.; Robert, R.; Weidenkaff, A.; Tucek, J.; Frydrych, J.; Grätzel, M. *J. Am. Chem. Soc.* **2010**, *132*, 7436.

(5) Lin, Y.; Zhou, S.; Sheehan, S. W.; Wang, D. *J. Am. Chem. Soc.* **2011**, *133*, 2398.

(6) Sivula, K.; Formal, F. Le; Grätzel, M. *Chem. Mater.* **2009**, *21*, 2862.

(7) Stefik, M.; Cornuz, M.; Mathews, N.; Hisatomi, T.; Mhaisalkar, S.; Grätzel, M. *Nano Lett.* **2012**, *12*, 5431.

(8) Riha, S. C.; Devries Vermeer, M. J.; Pellin, M. J.; Hupp, J. T.; Martinson, A. B. F. *ACS Appl. Mater. Interfaces* **2013**, *5*, 360.

(9) Zandi, O.; Klahr, B.; Hamann, T. *Energy Environ. Sci.* **2013**, *6*, 634.

(10) Hisatomi, T.; Brillet, J.; Cornuz, M.; Le Formal, F.; Tétreault, N.; Sivula, K.; Grätzel, M. *Faraday Discuss.* **2012**, *155*, 223.

(11) Le Formal, F.; Grätzel, M.; Sivula, K. *Adv. Funct. Mater.* **2010**, *20*, 1099.

(12) Zandi, O.; Beardslee, J. a; Hamann, T. W. *J. Phys. Chem. C* **2014**, *118*, 16494.

(13) Itoh, K.; Bockris, J. O. *J. Electrochem. Soc.* **1984**, *131*, 1266.

(14) Itoh, K.; Bockris, J. O. *J. Appl. Phys.* **1984**, *56*, 874.

(15) Liang, Y.; Enache, C. S.; van de Krol, R. *Int. J. Photoenergy* **2008**, *2008*, 1.

(16) Souza, F. L.; Lopes, K. P.; Longo, E.; Leite, E. R. *Phys. Chem. Chem. Phys.* **2009**, *11*, 1215.

(17) Cesar, I.; Sivula, K.; Kay, A. *J. Phys. Chem. C* **2009**, *113*, 772.

(18) Hisatomi, T.; Dotan, H.; Stefik, M.; Sivula, K.; Rothschild, A.; Grätzel, M.; Mathews, N. *Adv. Mater.* **2012**, *24*, 2699.

(19) Klahr, B. M.; Martinson, A. B. F.; Hamann, T. W. *Langmuir* **2011**, *27*, 461.

(20) Klahr, B.; Gimenez, S.; Fabregat-Santiago, F.; Hamann, T.; Bisquert, J. *J. Am. Chem. Soc.* **2012**, *134*, 4294.

(21) Dezelah, C. L.; Niinisto, J.; Arstila, K.; Niinisto, L.; Winter, C. H. *Chem. Mater.* **2006**, *18*, 471.

(22) Kronawitter, C. X.; Zegkinoglou, I.; Rogero, C.; Guo, J.-H.; Mao, S. S.; Himpsel, F. J.; Vayssieres, L. *J. Phys. Chem. C* **2012**, *116*, 22780.

(23) Xu, Y.; Schoonen, M. *Am. Mineral.* **2000**, *85*, 543.

(24) Young, K. M. H.; Klahr, B. M.; Zandi, O.; Hamann, T. W. *Catal. Sci. Technol.* **2013**, *3*, 1660.

(25) Sherman, D. M.; Waite, D. T. **1985**, *70*, 1262.

(26) Marusai, L. A.; Messier, R.; White, W. B. *J. Phys. Chem. Solids* **1980**, *41*, 981.

(27) Pailhé, N.; Wattiaux, a.; Gaudon, M.; Demourgues, a. *J. Solid State Chem.* **2008**, *181*, 2697.

(28) Sivula, K.; Zboril, R.; Le Formal, F.; Robert, R.; Weidenkaff, A.; Tucek, J.; Frydrych, J.; Grätzel, M. *J. Am. Chem. Soc.* **2010**, *132*, 7436.

(29) Bersani, D.; Lottici, P. P.; Ding, X.-Z. *Appl. Phys. Lett.* **1998**, *72*, 73.

(30) Bersani, D.; Lottici, P. P.; Montenero, A. *J. Raman Spectrosc.* **1999**, *360*, 355.

(31) Faria, D. De. *J. Raman Spectrosc.* **1997**, *28*, 873.

(32) Jubb, A. M.; Allen, H. C. *ACS Appl. Mater. Interfaces* **2010**, *2*, 2804.

(33) Heutz, S.; Salvan, G.; Silaghi, S. *J. Phys. Chem. B* **2003**, *107*, 3782.

(34) Balaji, S.; Djaoued, Y.; Robichaud, J. *J. Raman Spectrosc.* **2006**, *37*, 1416.

(35) Chernyshova, I. V; Hochella, M. F.; Madden, a S. *Phys. Chem. Chem. Phys.* **2007**, *9*, 1736.

(36) Xu, Y. Y.; Zhao, D.; Zhang, X. J.; Jin, W. T.; Kashkarov, P.; Zhang, H. *Phys. E Low-dimensional Syst. Nanostructures* **2009**, *41*, 806.

(37) Onari, S.; Arai, T.; Kudo, K. *Phys. Rev. B* **2008**, *16*, 1717.

(38) Glasscock, J. a.; Barnes, P. R. F.; Plumb, I. C.; Bendavid, A.; Martin, P. J. *Thin Solid Films* **2008**, *516*, 1716.

Chapter 3:

Enhancing the Photovoltage of Hematite Electrodes Through Surface State Passivation

3.1 Abstract

Hematite (α-Fe_2O_3) thin film electrodes prepared by atomic layer deposition (ALD) were employed to photoelectrochemically oxidize water under 1 sun illumination. It was shown that annealing at 800 °C dramatically improves the photovoltage of the ultrathin film hematite electrodes. The effect of high temperature treatment is shown to remove one of two surface states identified, which reduces recombination and Fermi level pinning. Further modification with Co-Pi water oxidation catalyst resulted in unprecedented onset voltage of ~0.6 V vs. RHE (slightly positive of the flat band potential).

3.2 Introduction

In the previous chapters the thin film absorber approach was introduced as a promising approach to scale up the light absorption while maintaining the hematite electrode thickness in the order of the hole collection length. One downside of ultrathin hematite films is the substrate-film interface effects which results in the defective hematite films. We demonstrated that this limitation can be effectively mitigated by incorporating an oxide underlayer e.g. Ga_2O_3 or Nb_2O_5. Ultrathin films of hematite with a Ga_2O_3 underlayer demonstrated PEC water oxidation performance as good as the state of the art bare planar hematite electrodes. The photocurrent onset potential of bare hematite electrode however, regardless of the preparation methods, has been consistently around 1.1-1.2 V vs RHE, which is about 600 mV positive of the theoretically expected value (i.e. flat band potential).[1–3] The positive photocurrent onset potential is attributed to surface recombination.[4–7]. Thus, the surface hole collection efficiency is an important factor which influences the working photovoltage and thus directly the STH efficiency.[1,6,8] In the case of hematite, surface recombination is responsible for nearly 600 mV voltage loss, which strongly limiting the potential utilization of hematite electrodes in a tandem PEC devices.

Strategies to improve the photovoltage are mainly based on modifications of the electrode surface aiming to suppress surface recombination or accelerate forward hole transfer to H2O oxidation reaction. In fact the state-of-the-art devices have produced promising results by applying efficient water oxidation catalyst systems such as Co-Pi.[9–11] For this system, the photovoltage was improved by ~0.25 V which we attributed to better charge separation thus reducing surface state recombination.[9] Recently a photocurrent onset as low as ~0.69 V *vs.* RHE was reported by Du *et al.* for thin film hematite electrodes

modified with a $NiFeO_x$ catalyst.[12] Numerous examples of an onset potential shift upon incorporation of water oxidation catalysts, and oxide overlayers all indicate the importance of surface properties on the water oxidation performance of hematite electrodes. Here we demonstrate that a water oxidation onset potential as low as ~0.7 V *vs*. RHE is achievable for a bare hematite electrode by annealing out deleterious surface states and thus reducing surface recombination. Further modification with Co-Pi reduces the onset potential to produce the highest reported photovoltage to date.

3.3 Experimental

Hematite thin films were prepared by atomic layer deposition (ALD) according to the procedure described in chapter 2. Hematite electrode included 300 ALD cycles (18 nm) of Fe_2O_3 deposited on a Ga_2O_3 coated FTO substrates. The films were first annealed by heating to 500 °C at a rate of 17 °C /minute, sintered at 500 °C for 30 minutes, and allowed to cool to room temperature over 2 hours. For high-T annealing, electrodes were the further annealed at 800 °C in a preheated furnace for 4 minutes followed by immediate cooling at ambient.

Co-Pi was deposited by photo-electrodeposition according to previous reports.[9,10] Hematite electrodes were immersed in a solution containing 0.5 mM $Co(NO_3)_2 \cdot 6H_2O$ in a 0.1 M phosphate buffer (pH 6.9). A bias of 0.7 V *vs.* RHE was applied under 1 sun illumination. The thickness of the Co-Pi layer was controlled by varying the amount of charge allowed to pass during the deposition. For the electrodes reported herein, it was found that ~ 0.12 mC cm^{-2} charge (30 s at 4 μA cm^{-2}) results in the most effective activity.

For photoelectrochemical measurements, electrodes were examined in contact with aqueous solutions of 1 M KOH and added amount of 0.5 M H_2O_2 as hole scavenger. A homemade saturated Ag/AgCl electrode was used as a reference electrode and high surface area platinum mesh was used as the counter electrode. The reference electrode was regularly calibrated *vs*. saturated calomel electrode (SCE) (Koslow Scientific) and all potentials were converted to the reversible hydrogen electrode (RHE) scale by the equation $V_{RHE} = V_{Ag/AgCl} + 0.197\ V + pH\ (0.059\ V)$. Photoelectrochemical measurements were made with an Eco Chemie Autolab potentiostat coupled with Nova electrochemical software. The light source was a 450 W Xe arc lamp (Horiba Jobin Yvon). An AM 1.5 solar filter was used to simulate sunlight at 100 mW cm^{-2} (1 sun). All photoelectrochemical tests were carried out by shining light on the electrodes through the electrolyte side (front side illumination). Chopped Light *J-V* curves were measured at a rate of 75 mV s^{-1} using a computer controlled ThorLabs solenoid shutter. Cyclic voltammogram surface state measurements were performed by applying a potential of 2.0 V *vs.* RHE under 1 sun illumination for 60 seconds, and then scanning cahtodically in the dark. Impedance measurements were measured at different applied bias using perturbation amplitude of 10 mV. The frequency range was 10 kHz-6 mHz. Data were fit using Zview software (Scribner Associates).

3.4 Results and discussion

A very straightforward way to quantify the water oxidation efficiency loss due to surface recombination is to compare the photocurrent density *vs*. applied voltage (*J-V*) behavior of electrodes in contact with H_2O and a hole scavenger such as $[Fe(CN)_6]^{4-}$ or H_2O_2.[13,14] Previous studies showed that hole collection efficiency by a hole scavenger is

essentially unity. Therefore, any differences in the *J-V* behavior for electrodes in contact with an aqueous electrolyte, with and without a good hole scavenger, can be unambiguously attributed to surface state recombination. This situation is shown in Figure 3-1 for a hematite thin film electrode in contact with H_2O and H_2O_2 solutions. Assuming no surface recombination for H_2O_2 oxidation, it can be clearly seen that surface recombination is responsible for the loss of ~600 mV of photovoltage under H_2O oxidation condition.[13,14] Surface recombination has been attributed to slow kinetic of four-hole H_2O oxidation reaction, which allows recombination of the surface holes with conduction band electrons.[1,15,16] In addition to slow kinetics, surface trap states can enhance surface recombination by catalyzing parasitic electron hole recombination reactions as well as by pinning the Fermi level on the surface which limits the output photovoltage as observed by others.[4,17,18]

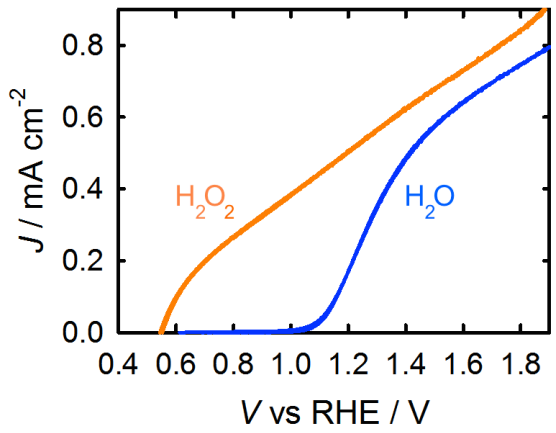

Figure 3.1. *J-V* curves of a hematite thin film electrode annealed at 500 °C in contact with aqueous solutions of 1M KOH and added 0.5 M H_2O_2 under 1 sun illumination.

A general approach to prepare hematite electrodes includes annealing at elevated temperatures to induce crystallinity and obtain phase pure hematite as iron oxide to hematite phase change occurs at temperatures above 450 °C.[19,20] Thus conventionally the annealing temperature of 450-550 °C has been chosen. In this study ultrathin thin film hematite electrodes prepared by atomic layer deposition (18 nm films of hematite deposited on Ga_2O_3 coated FTO substrates) were annealed at 800 °C and examined under PEC water oxidation condition. Control thin films were also prepared by annealing at 500 °C. Control experiments showed that annealing at 800 °C for 4 minutes does not have any measurable effect on the conductivity of FTO substrates, in agreement with previous reports.[11] Figure 3-2 shows *J-V* curves of bare hematite films annealed at 500 and 800 °C. As seen in this graph, high temperature annealing dramatically improves the photovoltage, resulting in the cathodic shift of the *J-V* curve in excess of 300 mV. A cathodic shift of the H_2O oxidation onset potential to ~0.9 V *vs*. RHE upon annealing at 800 °C was also observed by Sivula *et al*.[21]. More recently Domen and co-workers reported the best overall water splitting performance of hematite electrodes which were annealed at 800 °C, however the effect of annealing temperature was not explored.[11]

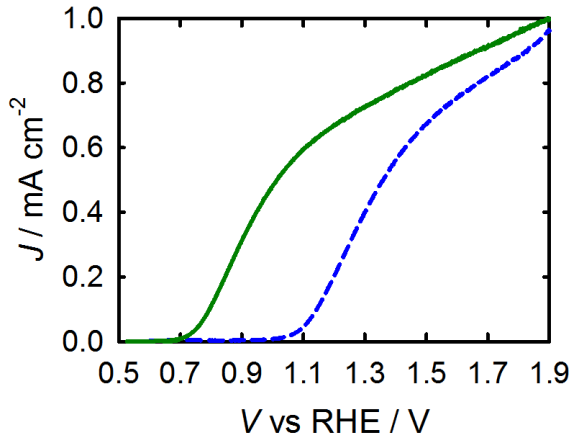

Figure 3-2. *J-V* curves of 18 nm hematite electrodes annealed at 500 °C (dashed blue) and 800 °C (solid green) under H_2O oxidation conditions at pH 13.6 and 1 sun illumination. Dark *J-V* curves are provided in the appendix.

The cathodic shift in the H_2O oxidation photocurrent onset is generally attributed to improved water oxidation efficiency through suppression of surface electron/hole recombination. In order to separate any improvement due to modification of the bulk film from the surface effects, *J-V* measurements were performed in the presence of H_2O_2 and compared to that of H_2O oxidation. As it can be seen from Figure 3-3 (top panel), with H_2O_2 the *J-V* response is nominally identical, with no significant difference in the observed photocurrent or photovoltage. Therefore, the *J-V* difference observed between electrodes annealed at 500 and 800 °C under water oxidation conditions is strictly a consequence of surface effects.

The role of surface states in the PEC water oxidation reaction with hematite electrodes prepared by ALD has already been investigated in detail.[1,4] It was shown that the water oxidation onset is associated with the accumulation of photogenerated holes at the electrode

surface which manifests as a capacitance.[1] This surface state capacitance has a peak around the onset of water oxidation that can be observed through electrochemical impedance (EIS) measurements, photocurrent transients and cyclic voltammetry (CV) measurements.[1,4] In addition to these surface states, another set of states was observed in the CV measurements at more negative potentials (i.e. around the flat band potential). These states showed a similar transient behavior during anodic oxidation, i.e. only observed at relatively high scan rates.[1]

In order to examine the effect of high temperature annealing on the surface states properties, CV measurement were carried out of the electrodes annealed at 500 and 800 °C. For this purpose, electrodes were held at 2 V *vs*. RHE under 1 sun illumination for 60 seconds (in order to photoelectrochemically oxidize the surface states) followed by measuring the cathodic current in the dark as the potential is scanned negatively at 1 V/s (Figure 3-3 c and d). For the control hematite electrode (annealed at 500 °C) on the first scan two peaks in current appear at around 1.1 V and 0.65 V *vs*. RHE. On the second cycle, both of these peaks are gone due to the transient nature of the oxidized states in agreement with the previous work.[1] CV curves at different scan rates are provided in the appendix (Figure A3-2). For the electrodes annealed at 800 °C, only one peak was observed, which coincides with the H_2O oxidation onset potential. The first cathodic peak, which always appears at potentials around the photocurrent onset, has been assigned to the reduction of oxidized surface species (H_2O oxidation intermediates).[1] Therefore, we attribute the first cathodic peak (~1.1 V for control electrode and ~0.7 V for the electrodes annealed at 800 °C) to the same effect. The absence of the second peak at ~0.65 V for the electrodes annealed at 800 °C, clearly indicates the passivation of this set of surface states with an

energy close the flat band (i.e. ~0.52 V *vs*. RHE) upon annealing. This finding is consistent with a recent report by Kronawitter *et al*. who utilized soft X-ray absorption spectroscopy to show that high-temperature annealing can remove oxygen p-hybridized states located just below the conduction band minimum.[22] The existence of a surface states at this energy is also consistent with observations by others through transient absorption spectroscopy measurements.[23,24]

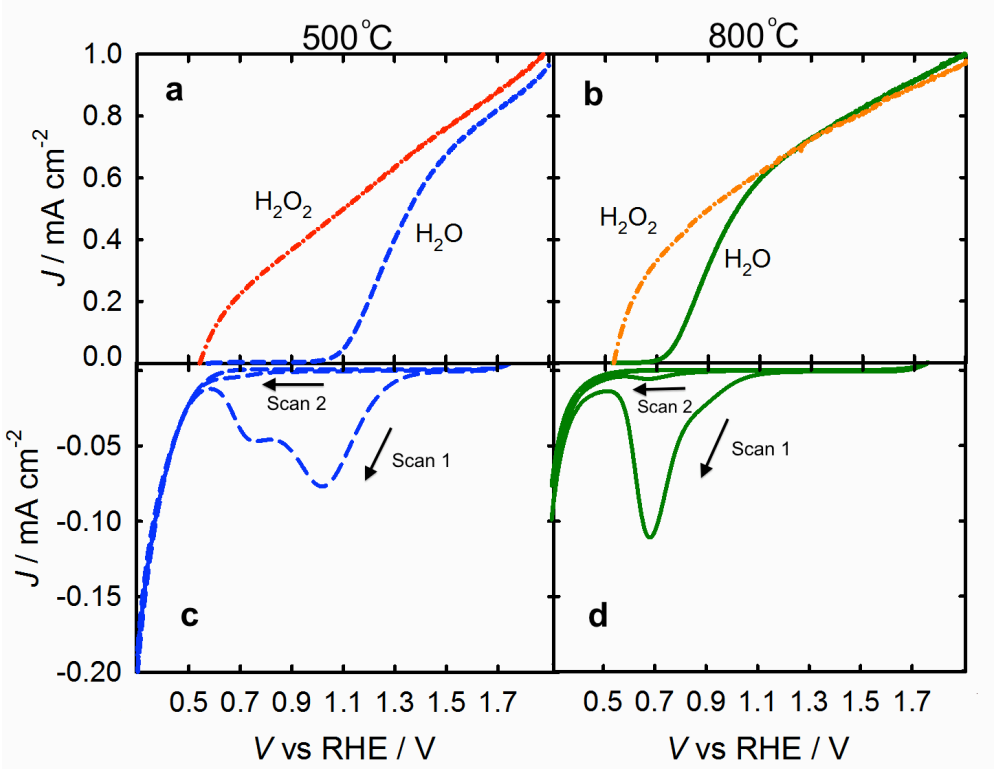

Figure 3-3. *J-V* curves under H_2O and H_2O_2 oxidation conditions for hematite electrodes annealed at 500 °C (a) and 800 °C (b). CV curves scanned at 1 V/s in dark of the electrodes annealed at 500 °C (c) and 800 °C (d).

Surface states with an energy above the charge neutrality level can potentially pin the Fermi level of an n-type semiconductor which gives rise to a fixed barrier height.[18,25] The

density and energy distribution of surface states, therefore, dictates the extent of band bending (barrier height) at the interface. The shallow states identified herein can thus pin the Fermi level and limit the extent of band bending at the hematite/solution interface which controls electron-hole separation. This situation is depicted in Figure 3-4. Indeed, we previously showed Fermi level pinning can account for ~200 mV shift in the *J-V* curves under water oxidation conditions compared to when a fast hole collector was present.[1] The *J-V* curves of the hematite electrode annealed in 500 °C in contact with H_2O and H_2O_2 (Figure 3-3a) do not overlap exactly at positive potentials; the H_2O_2 electrolyte always produces somewhat higher photocurrent at a given applied potential compared to water oxidation conditions.[13,14] This discrepancy can be attributed to the extra potential needed to compensate for Fermi level pinning during water oxidation. As seen in Figure 3-3b this is not the case for the electrode annealed at 800 °C. We therefore attribute part of the increased photovoltage upon annealing at 800 °C to the mitigation of Fermi level pining at the hematite/electrolyte interface by passivating the set of surface states right below he conduction band. The remainder of the increased photovoltage achieved through high temperature annealing is due to the decreased surface state recombination.

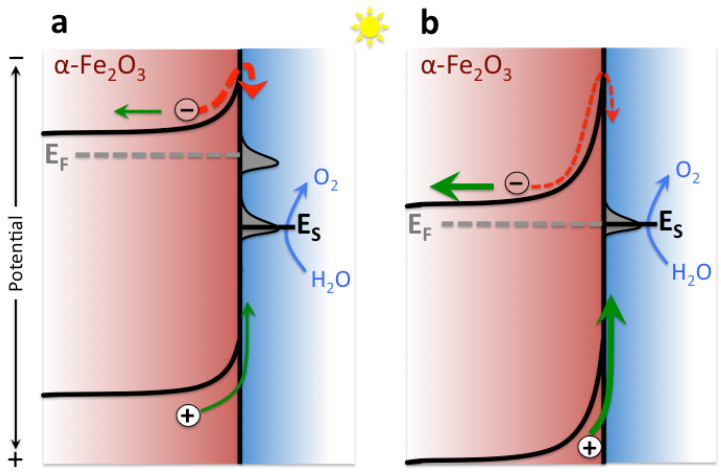

Figure 3-4. Simplified band diagram of hematite electrodes under conditions with (a) and without (b) Fermi level pining by the sub-conduction band surface states.

To further confirm this assignment, electrochemical impedance spectroscopy (EIS) was performed on the hematite electrodes in contacts with aqueous solution under illumination. A physical model was previously developed to describe the capacitive and resistive element under PEC H_2O oxidation at hematite-solution interface.[4] The model includes capacitance due to accumulation of holes on the surface (surface state capacitance, C_{ss}) in addition to space charge capacitance, C_{bulk} (Figure 3-5). Two representative Nyquist plots are shown in Figure 3-5. Each semicircle is representing a capacitive element which appear at specific frequency. From these plots one immediately infers that at 0.9 V vs RHE, charge transfer resistance from the surface states significantly (~2 order of magnitude) lower for the electrode annealed at 800 °C. This is consistent with the *J-V* curves shown in Figure 3-2 where stable photocurrent was measured for this electrode at this potential.

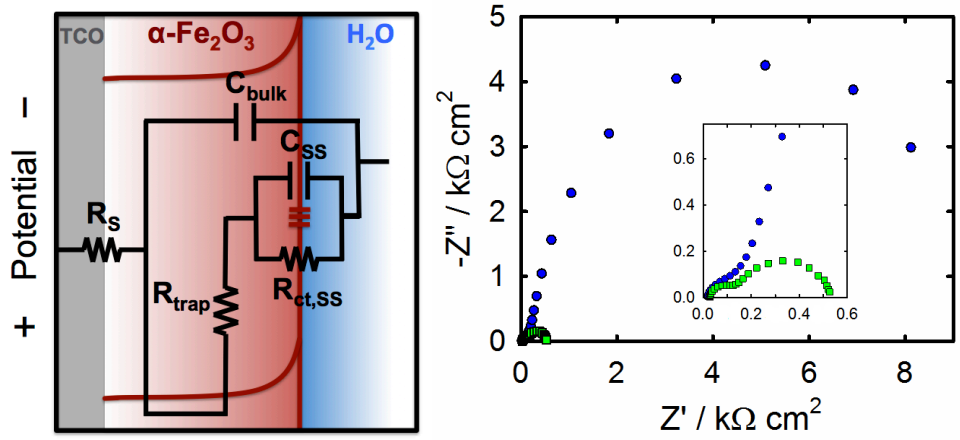

Figure 3-5. Equivalent circuit model used to fit the EIS data under illumination. Shown on the right are representative Nyquist plots for hematite electrodes annealed at 500 (blue circles) and 800 °C (green squares) measured at 0.9 V *vs.* RHE.

The EIS data were then fitted to the equivalent circuit shown in figure 3-5 to extract impedance data measured at different DC bias. Mott-Schottky plots were produced from space charge capacitance using the Mott-Schottky equation shown below, where q is the elementary charge, κ is hematite dielectric contestant (taken as 32), ε_0 is vacuum permittivity and N_D is dopant density.

$$\left(\frac{A}{C_{Bulk}}\right)^2 = \frac{2}{q\kappa\varepsilon_0 N_D}\left(E - E_{FB} - \frac{kT}{q}\right) \qquad (3\text{-}1)$$

The effect of Fermi level pinning was also observed in the Mott-Schottky plots for hematite electrodes annealed at 500 °C. As seen in Figure 3-6, Fermi level pinning appears as a nearly 200 mV "potential independent" region around the same potential where the second peak in the CV responses was observed (0.65 V *vs*. RHE) which was eliminated upon annealing at 800 °C. The absence of Fermi level pinning for the

electrode annealed at high T further confirms the assignment of surface state passivation as the primary effect of high T annealing.

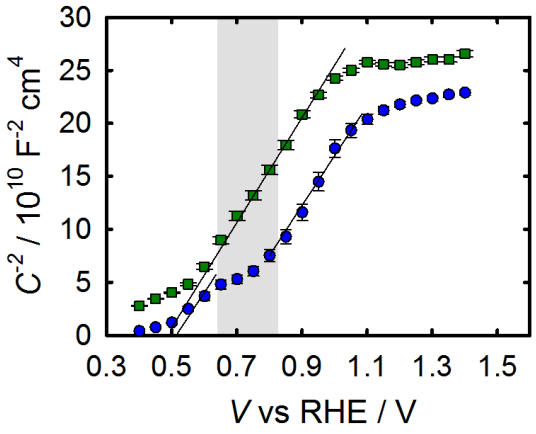

Figure 3-6. Mott-Schottky plots of hematite electrodes annealed at 500 °C (blue circles) and 800 °C (green squares) under water oxidation conditions and 1 sun illumination.

Surface state capacitance, C_{ss}, and charge transfer resistance, R_{ct}, measured at different applied bias are shown in Figure 3-7. From the C_{ss} it can be clearly seen that both electrode annealed at 500 and 800 °C show a peak in C_{ss}, however, at different potentials. The potential at which the peak of the C_{ss} was observed for the electrode annealed at 800 °C, was shifted ~ 400 mV cahtodically, in line with the shift in the *J-V* responses.

Both peaks coincide with the photocurrent onset potential of respective electrodes; in exact same manner as the first peak in the CV responses. Similar to C_{ss}, charge transfer diminishes to a minimum value around the H_2O oxidation photocurrent onset and thus the peak of the surface state capacitance (Figure 3-7). At 0.9 V vs RHE, the value of charge transfer is nearly 2 orders of magnitude lower for the hematite electrode annealed at 800

°C as seen in the Nyquist plots. Nearly 400 mV cathodic shift of the R_{ct} minimum a indicates a more active surface toward H_2O oxidation, i.e. less surface recombination, for electrode annealed at high T. In addition, the surface states observed in the EIS are identical in magnitude, but shifted in potential, indicating that the high T annealing does not alter the nature of these state as seen in the CV measurements. This reconciles our previous assignment of these state to high valent Fe=O species involved in PEC water oxidation reaction.[1]

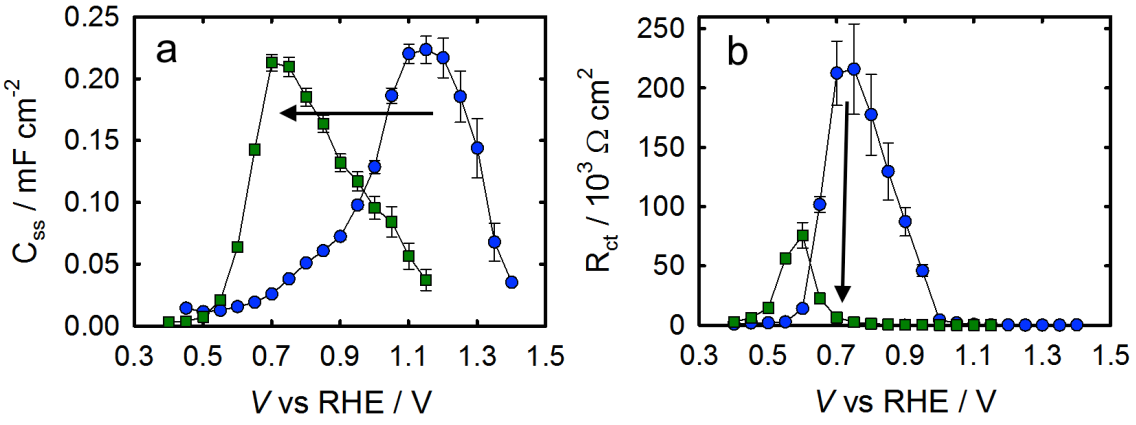

Figure 3-7. Surface state capacitance, C_{ss} (a) and charge transfer resistance, R_{ct} (b) extracted form EIS measurements at different applied potential under illumination for hematite electrodes annealed at 500 °C (blue circles) and 800 °C (green squares).

Despite of drastic improvement in the photovoltage through annealing at high temperature, the onset of H_2O oxidation is still ~200 mV more positive compared to H_2O_2 oxidation onset (i.e. the the flat band potential). This discrepancy can be clearly seen in the chopped light *J-V* curve shown in Figure 3-8a. At potentials just positive of the flat band, even though hole accumulation at the surface occurs (transient peak in current), the recombination rate is too high to allow any steady state faradic current. Assuming the same flux of holes from the bulk for electrodes in contact with H_2O and H_2O_2, the difference in the *J-V* responses shown in Figure 3a can be explained in terms of the slow kinetics of H_2O oxidation not being able to compete with recombination at these potentials, however the fast kinetics of H_2O_2 oxidation can. If this is indeed the case, modification of the hematite surface with a water oxidation catalyst should push the onset potential toward that of H_2O_2 oxidation. Co-Pi based catalysts have been shown to enhance the water oxidation kinetics in variety of electrochemical and photoelectrochemical sysytems.[9,10,26] Therefore, hematite electrodes annealed at 800 °C were further coated with Co-Pi *via* photo-electrodeposition following the procedure reported previously.[9,10] *J-V* curves of a hematite electrode coated with Co-Pi is shown in Figure 3-8b. The Co-Pi modification resulted in an additional ~100 mV shift of the onset potential with a concomitant photocurrent at lower biases. The photocurrent and photovoltage is still less than that of H_2O_2 oxidation at these low applied biases, however, which indicates the rate of surface recombination is still relevant for H_2O oxidation on high temperature annealed surfaces with a Co-Pi catalyst, however it is dramatically reduced.

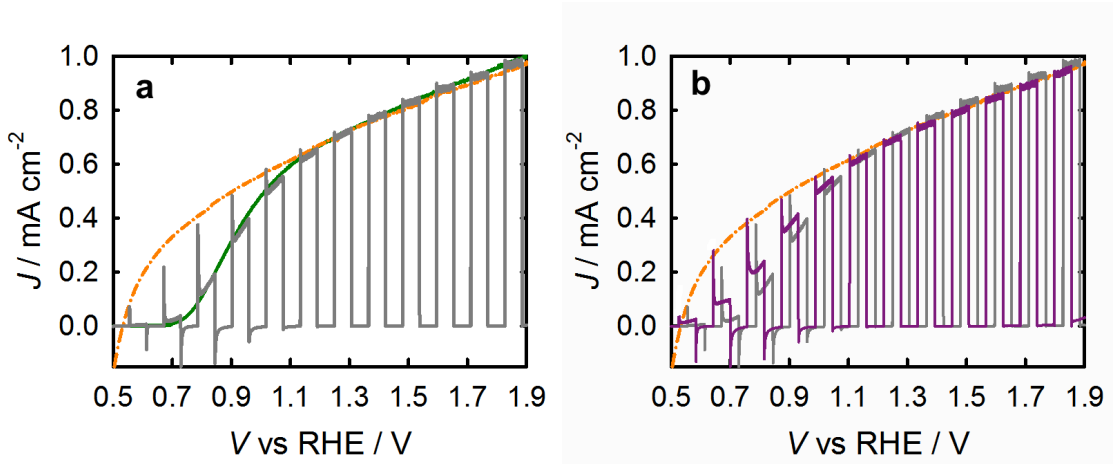

Figure 3-8. a) *J-V* curves of a hematite electrode annealed at 800 °C in contact with H_2O under chopped (solid grey) and continuous (solid green) 1 sun illumination. b) Chopped light *J-V* curves of bare (solid grey) and Co-Pi coated (solid purple) hematite electrodes in contact with H_2O under 1 sun illumination. The *J-V* curve of the bare electrode under H_2O_2 oxidation (dash dotted orange) is also shown for comparison.

The stability of hematite/Co-Pi photoanode systems under H_2O oxidation conditions is well established.[9–11] However, to further confirm the stability and reproducibility of the hematite electrodes annealed at 800 °C, six different electrodes from different ALD batches were annealed at 800 °C and tested under water oxidation conditions. Reproducible stable *J-V*, CV and steady state photocurrent were measured, further confirming the reproducibility and stability of our photoanode system (see Figure A3-3).

Charge separation and collection efficiency were then calculated to gain a more quantitative insight on the quantum efficiency of electron-hole separation and transfer in the bulk and on the surface using the procedure described elsewhere.[14] Assuming the surface hole collection efficiency (η_{hc}) of unity with H_2O_2, the η_{hc} of H_2O oxidation can be calculated by dividing J_{H_2O} by $J_{H_2O_2}$. Plots of calculated values for η_{hc} for hematite

electrodes annealed at 500 and 800 °C are shown in Figure 3-9a. The η_{hc} trend generally resembles that of the H_2O oxidation *J-V* curves, increasing with applied potential. Most notably the η_{hc} of H_2O oxidation with the hematite electrode annealed at 800 °C reaches nearly 100 % at around 1 V *vs*. RHE, while for electrode annealed at 500C the η_{hc} reaches the maximum of 80% at significantly more positive potentials. At 1.23 V η_{hc} is almost 100% for the electrode annealed at 800 °C, indicating quantitative hole collection efficiency on these electrodes. Even with quantitative hole collection efficiency the maximum photocurrent observed at 1.23 V is significantly lower than what is expected based on the flux of the absorbed photons. The maximum photocurrent (J_{abs}) of ~ 4 mA is expected for these thin films by integrating the solar photon flux absorbed by the hematite film and assuming the quantum efficiency of unity, according the following equation.

$$J_{abs}=-q\int_{280}^{\lambda_{gap}}\Phi(\lambda)\times Absorptance\ (\lambda)\times d\lambda \qquad (3\text{-}2)$$

The charge separation efficiency, η_{cs}, can then be calculated by dividing $J_{H_2O_2}$ by J_{abs}. Plots of η_{cs} as a function of applied potential are shown in Figure 3-9b. At 1.23 V the η_{cs} is only ~15% of the expected photocurrent, indicating 85% bulk electron-hole recombination. Although A very short hole diffusion length (and lifetime) is often described to be the dominant factor impeding electron-hole separation in the bulk, our results show that depletion region recombination is essentially limiting charge separation efficiency given that η_{cs} is only ~ 25 % at very positive potential where the entire film is depleted. Thus, although short hole diffusion length is a limiting factor for thick electrode, our results for thin films shows even in the presence of electric field in the depletion region, charge separation is far from quantitative. We therefore, conclude that in addition to bulk recombination (which

always presents for thick electrodes) strong depletion region recombination plays the key role at limiting charge separation efficiency thus the photocurrent of the thin film electrodes.

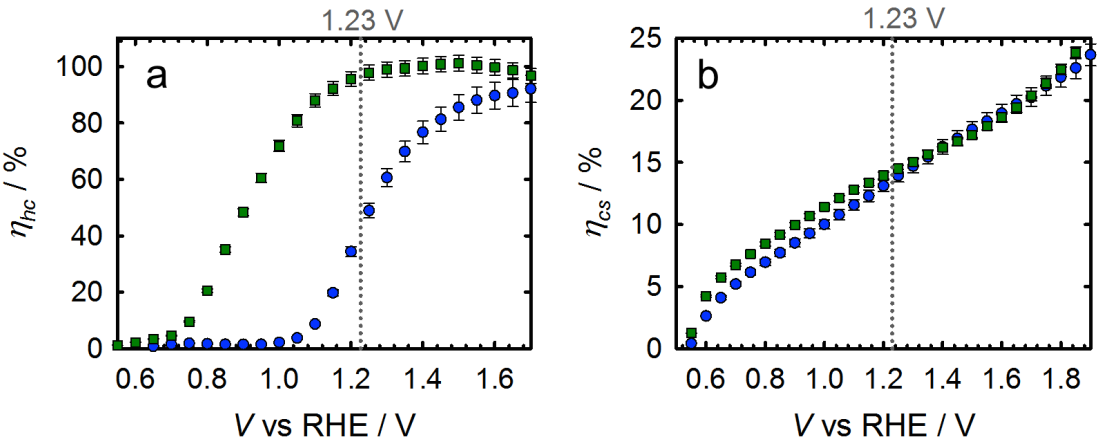

Figure 3-9. Hole collection (a) and charge separation (b) efficiency of hematite electrode annealed at 500 °C (blue circles) and 800 °C (green squares).

3.5 Conclusion

In summary, it was demonstrated that the photovoltage of H_2O oxidation on hematite electrodes can be significantly improved upon annealing at 800 °C. Cyclic voltammetry measurements revealed that a set of surface states with an energy of slightly below the flat band potential are eliminated upon annealing at 800 °C. The performance improvement was therefore attributed to the mitigation of Fermi level pining by these states and a reduction of surface state recombination. Even with the high temperature annealing, there is an additional surface state that coincides with the water oxidation onset potential that we attributed to water oxidation intermediates. The fact that this state remains prominent, and coincides with the photocurrent onset, following the high temperature annealing supports this assignment.

These results are significant as it reconciles the interpretation of surface states throughout the literature as we clearly show that there are two very distinct states, one set that is problematic and another that is inherent in the water oxidation process. Moreover, a route to improve the photovoltage by selectively eliminating the deleterious surface states was demonstrated. We note that it is unlikely that the photocurrent onset would be negative of the flat band potential, and we have shown that the combination of high temperature annealing and the addition of a water oxidation catalyst produce an onset potential only 100 mV more positive of the flat band, thus very little further improvement is probable.

Hematite thin film electrode annealed at 800 °C demonstrated quantitative surface hole collection efficiency, indicating effective surface recombination suppression. The charge separation efficiency, however, is strongly limited by bulk recombination. More specifically we showed that depletion region recombination is the primary limiting factor of the charge separation efficiency of the thin films, which needs to be mitigated to enhance the overall photocurrent. Doping hematite with aliovalent ions to increase the n-type carrier density is one strategy to increase the charge separation efficiency which is the topic of next chapter.

APPENDIX

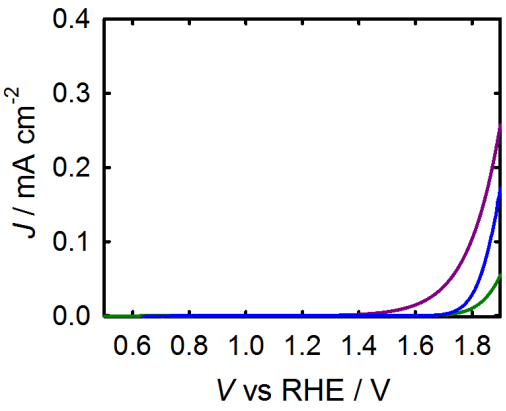

Figure A3-1. *J-V* curves of hematite electrodes annealed at 500 °C (blue), and 800 °C with (purple) and without Co-Pi (green) measured under water oxidation conditions in dark.

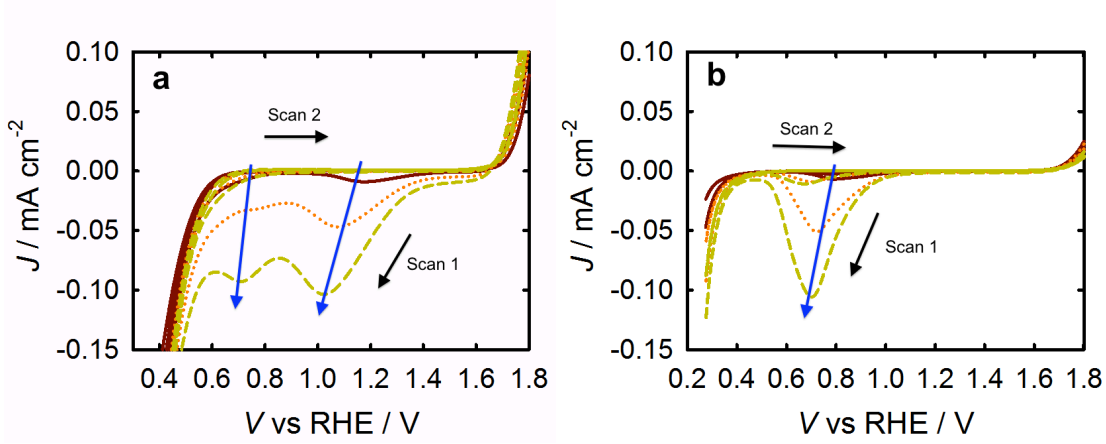

Figure A3-2. CV curves of hematite electrodes annealed at 500 °C (a) and 800 °C (b) measured at the scan rate of 100 (solid dark red), 500 (dotted orange) and 1000 (dashed yellow) mV/s.

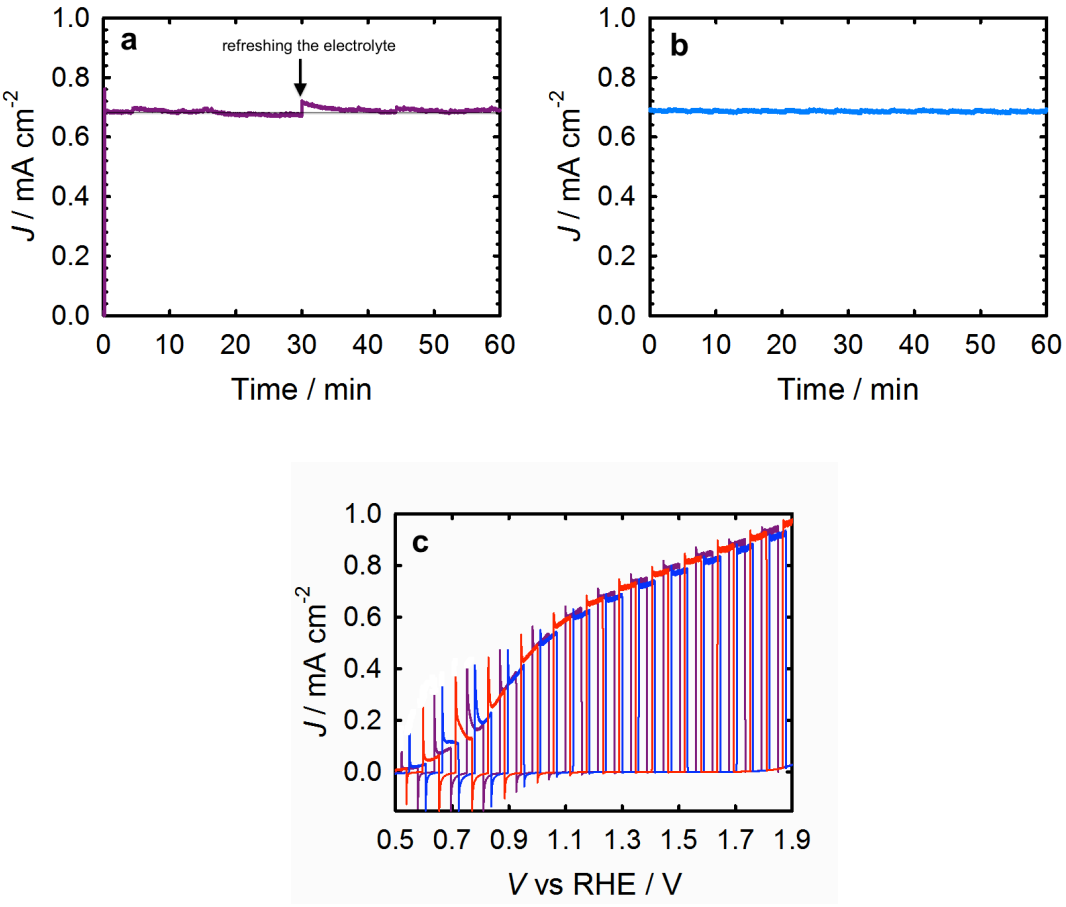

Figure A3-3. Photocurrent density (*J*) measured for a hematite/Co-Pi electrode under 1 sun illumination and a constant applied potential of 1.23 V vs RHE in (a) an aqueous electrolyte without bubbled O_2 and (b) a solution saturated with O_2. c) *J-V* curves measured in the absence (purple) and presence of saturated O_2 (blue) and N_2 (red). Refreshing the electrolyte in (a) consisted of removing bubbles formed on the surface of the electrode by pipetting fresh electrolyte into the cell (this is not the case when O_2 was bubbled into the solution).

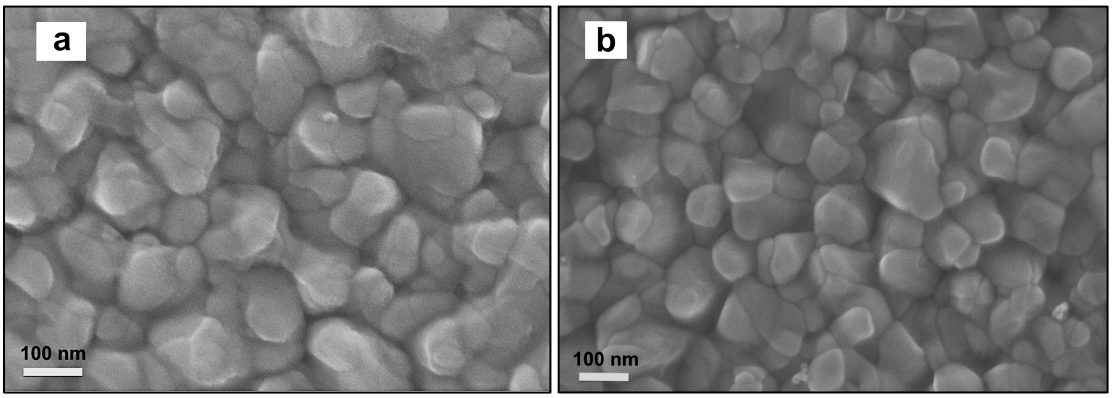

Figure A3-4. SEM images of hematite films annealed at 500 °C (a) and 800 °C (b).

REFERENCES

REFERENCES

(1) Klahr, B.; Gimenez, S.; Fabregat-Santiago, F.; Bisquert, J.; Hamann, T. W. *Energy Environ. Sci.* **2012**, *5*, 7626.

(2) Kay, A.; Cesar, I.; Grätzel, M. *J. Am. Chem. Soc.* **2006**, 15714.

(3) Zandi, O.; Beardslee, J.; Hamann, T. *J. Phys. Chem. C* **2014**, *118*, 16494.

(4) Klahr, B.; Gimenez, S.; Fabregat-Santiago, F.; Hamann, T.; Bisquert, J. *J. Am. Chem. Soc.* **2012**, *134*, 4294.

(5) Young, K. M. H.; Klahr, B. M.; Zandi, O.; Hamann, T. W. *Catal. Sci. Technol.* **2013**, *3*, 1660.

(6) Peter, L. M.; Wijayantha, K. G. U.; Tahir, A. a. *Faraday Discuss.* **2012**, *155*, 309.

(7) Barroso, M.; Pendlebury, S.; Cowan, A.; Durrant, J. *Chem. Sci.* **2013**, *4*, 2724.

(8) Hamann, T. W. *Dalton Trans.* **2012**, *41*, 7830.

(9) Klahr, B.; Gimenez, S.; Fabregat-Santiago, F.; Bisquert, J.; Hamann, T. W. *J. Am. Chem. Soc.* **2012**, *134*, 16693.

(10) Zhong, D. K.; Gamelin, D. R. *J. Am. Chem. Soc.* **2010**, *132*, 4202.

(11) Kim, J. Y.; Magesh, G.; Youn, D. H.; Jang, J.-W.; Kubota, J.; Domen, K.; Lee, J. S. *Sci. Rep.* **2013**, *3*, 1.

(12) Du, C.; Yang, X.; Mayer, M. T.; Hoyt, H.; Xie, J.; McMahon, G.; Bischoping, G.; Wang, D. *Angew. Chem. Int. Ed. Engl.* **2013**, *52*, 12692.

(13) Klahr, B. M.; Hamann, T. W. *J. Phys. Chem. C* **2011**, *115*, 8393.

(14) Dotan, H.; Sivula, K.; Grätzel, M.; Rothschild, A.; Warren, S. C. *Energy Environ. Sci.* **2011**, *4*, 958.

(15) Cummings, C. Y.; Marken, F.; Peter, L. M.; Upul Wijayantha, K. G.; Tahir, A. A. *J. Am. Chem. Soc.* **2012**.

(16) Pendlebury, S. R.; Cowan, A. J.; Barroso, M.; Sivula, K.; Ye, J.; Grätzel, M.; Klug, D. R.; Tang, J.; Durrant, J. R. *Energy Environ. Sci.* **2012**, *5*, 6304.

(17) Cummings, C. Y.; Marken, F.; Peter, L. M.; Tahir, A. a; Wijayantha, K. G. U. *Chem. Commun.* **2012**, *48*, 2027.

(18) Bard, A. J.; Bocarsly, A. B.; Fan, F. F.; Walton, E. G.; Wrighton, M. S. *J. Am. Chem. Soc.* **1980**, *102*, 3671.

(19) Sherman, D. M. *Phys. Chem. Miner.* **1985**, *12*, 161.

(20) Beermann, N.; Vayssieres, L.; Lindquist, S.-E.; Hagfeldt, A. *J. Electrochem. Soc.* **2000**, *147*, 2456.

(21) Sivula, K.; Zboril, R.; Le Formal, F.; Robert, R.; Weidenkaff, A.; Tucek, J.; Frydrych, J.; Grätzel, M. *J. Am. Chem. Soc.* **2010**, *132*, 7436.

(22) Kronawitter, C. X.; Zegkinoglou, I.; Rogero, C.; Guo, J.-H.; Mao, S. S.; Himpsel, F. J.; Vayssieres, L. *J. Phys. Chem. C* **2012**, *116*, 22780.

(23) Barroso, M.; Cowan, A. J.; Pendlebury, S. R.; Grätzel, M.; Klug, D. R.; Durrant, J. R. *J. Am. Chem. Soc.* **2011**, *133*, 14868.

(24) Barroso, M.; Mesa, C. a; Pendlebury, S. R.; Cowan, A. J.; Hisatomi, T.; Sivula, K.; Grätzel, M.; Klug, D. R.; Durrant, J. R. *Proc. Natl. Acad. Sci. U. S. A.* **2012**, *109*, 15640.

(25) Lewerenz, H. J. *J. Electroanal. Chem.* **1993**, *356*, 121.

(26) Kanan, M. W.; Nocera, D. G. *Science* **2008**, *321*, 1072.

Chapter 4:

Investigating the Role of Ti-doping in Hematite Thin Film Electrodes

Adapted with permission from:

Highly Photoactive Ti-doped α-Fe_2O_3 Thin Film Electrodes; Resurrection of the Dead Layer, Omid Zandi, Benjamin M. Klahr, and Thomas W. Hamann, *Energy Environ. Sci.,* **2013***, 6,* 634–642.

4.1 Abstract

Uniform thin films of hematite and Ti-doped hematite (α-Fe_2O_3) were deposited on transparent conductive substrates using atomic layer deposition (ALD). ALD's epitaxial growth mechanism allowed controlling the morphology and thickness of the hematite films as well as the concentration and distribution of Ti atoms. The photoelectrochemical performance of Ti-doped and undoped hematite electrodes were examined and compared under water oxidation conditions. The incorporation of Ti atoms in hematite electrodes was found to dramatically enhance the water oxidation performance, with much greater enhancements found for the thinnest films. An optimum concentration ~3 atomic % of Ti atoms was also determined. A series of electrochemical, photoelectrochemical and impedance spectroscopy measurements were employed to elucidate the cause of the improved photoactivity of the Ti-doped hematite thin films. This performance enhancement was a combination of improved bulk properties (hole collection length) and surface properties (water oxidation efficiency). The improvement in both bulk and surface are attributed to the resurrection of a dead layer by the Ti dopant atoms.

4.2 Introduction

In the previous chapter we discussed and demonstrated that the hole diffusion length in polycrystalline hematite thin films are essentially zero, meaning that only a small portion of the photogenerated hole which are generated in the space charge layer can effectively be collected. Low absorbed photon to current conversion efficiency (APCE) for the ultrathin films (i.e. as thick as the depletion width) indicated strong depletion region recombination. In order to suppress bulk and depletion region recombinations, one strategy is depositing highly doped ultrathin hematite films through n-type doping.

Charge transport mechanism in hematite is known to happen via small polaron hoping at room temperature.[1–4] Small polarons are highly localized and thus require higher activation energy to hop to the neighboring atoms, resulting in a low carrier mobility.[5] Strategies to modify bulk properties to improve the charge transport in hematite have largely focused on n-type doping with aliovalent atoms. Doping is historically used in semiconducting material to tune the conductivity through increasing carrier concentration. While a high electron conductivity is generally required for efficient charge collection, hole conductivity in hematite is shown to be the limiting factor in charge separation.[6,7] Any attempt to tune the conduction property and increasing dopant density by intentional n-type doping, therefore, does not necessarily increase the hole conductivity which is happening via valence band. High concentration of dopants however, allows sharper band bending as potential drops across a thinner width. This is advantageous as hole are generated very close to the interface, which have greater chance to be collected as they travel a shorter distance and experience an already high drift potential.[8] Depletion region recombination is important in materials with low mobility such has hematite since it takes longer for holes to cross the

depletion region which increases the chance of recombination. Warren recently showed the relation between the hole transit time in the depletion region and dopant density for a range of small and large polaron mobility.[9] It was shown for a semiconductor with a low carrier mobility (e.g. hematite with hole mobility ~ 10^{-2} cm^2/Vs)[3,10,11] to have a transit time in the picoseconds regime (comparable with recombination time scale), dopant density must be $>10^{20}$ cm^{-3} corresponding to the depletion width of <10 nm. Therefore, higher dopant density (and smaller space charge layer) is required to accelerate the hole drift in the depletion layer.

Examples of intentional n-type doping include incorporation of M^{4+} cations into Fe^{3+} sites in hematite.[12–17] This in principle can induce oxygen vacancies and thus increase the majority carrier concentration and electron conductivity.[3,15] We note that in the case of hematite very high level of impurities (1-10%) are typically employed which is much larger than the ppm level of dopant generally needed to control the electronics of semiconductors. In principle, there are several ways by which dopants can improve the water oxidation efficiency.[18] Doping can enhance the charge separation efficiency by increasing the minority carrier mobility and/or lifetime and hence enhancing the flux of holes reaching semiconductor/electrolyte interface. This enhancement could arise, for example, from improved crystallinity of the hematite lattice, changing crystallographic orientation, or passivation of bulk trap states.[15,18] Dopants can act as structural directing agents and change the morphological nanostructure, which can modify the light absorption and charge collection efficiency.[17] Since PEC water oxidation is generally the metric used to determine the benefit of dopants, any dopant at the surface can act as a catalyst and thus improve hole collection efficiency. Alternatively, the dopants can passivate surface states thus reducing

surface recombination.[15,18] The dopants could also increase the majority carrier density, hence the flat band potential and conductivity. Interestingly, all of the above possible effects have been previously used to interpret the beneficial effect of different dopants.[13–15,18–20]

Glasscock *et al.* presented a thorough study of undoped and Si and Ti-doped hematite films prepared by magnetron sputtering.[15] It was shown that doping is necessary to activate the poor water oxidation performance of thin film hematite electrodes. Although Ti and Si-doping increased the films conductivity, the conductivity effect alone was argued to be insignificant. The activation mechanism through doping was attributed to the passivation of surface states and bulk grain boundaries and thus suppressing recombination.[15] They also observed significant structural and morphological change for Si-doped films compared to undoped and Ti-doped analogs. The Si-doped samples showed dominantly amorphous structure with significantly smaller grain size. No significant differences were observed in the morphology and crystallinity of undoped and Ti-doped electrodes. In the Raman spectra of Ti-doped films, however, an extra peak was observed at ~ 660 cm^{-1} which was attributed to disorder and grain boundaries near the surface.[15]

McFarland and co-workers studied hematite electrodes prepared by electrodeposition doped with various dopants including Pt, Al, Ti, Cr and Mo.[19–22] 5% Pt-doped hematite demonstrated significantly improved water oxidation photocurrent compared to undoped samples.[22] The effect of Pt was explained in term of increased conductivity resulting from an enhanced carrier concentration. No significant differences were observed in the XRD spectra of undoped and Pt-doped electrodes. Raman spectra, however, showed an extra peak at 657 cm^{-1} for doped samples with its intensity increasing with Pt concentration.[22] The variation in the Raman spectra was attributed to the changes in the surface structure upon

doping with Pt.[22] In another report they presented Al as an effective isovalent dopant for enhanced water oxidation with hematite.[19] While no enhanced carrier concentration is expected from isovalent Al, significantly improved water oxidation photocurrent was attributed to conductivity improvement induced by lattice contraction.[19] The lattice contraction, which was confirmed by structural refinement of XRD analysis, can potentially modify charge transport *via* polaron happing and hence the conductivity. The case of isovalent doping is a good example of performance enhancement through structural modification and not by increasing the carrier concentration. Structural changes observed for the Pt-doped hematite electrodes thus can also contribute to the water oxidation improvement, although it was not elucidated by the authors. They also studied the effect of Ti-doping in hematite films prepared by APCVD.[21] It was found that 0.8 atomic % Ti doped electrode demonstrate substantially higher IPCE when compared to undoped samples. Electrode morphology was found that significantly differs for undoped and Ti-doped samples at different Ti concentration. This dopant-induced structural change is often observed for such preparation methods, which makes the interpretation of photoelectrochemical data difficult.[17,21] He and Parkinson studied the effect of trace amount of metal dopants on hematite water oxidation activity through a high-throughput combinatorial mesurements.[23] The combinatorial approach allowed them to probe the effect of different dopant concentration as well as multiple dopants using an ink-jet printing device. It was found that Ti doping enhances the water oxidation photocurrent while Al and Si had little to no effect when added to the hematite structure individually. Addition of multiple dopants also showed enhanced water oxidation activity, indicating the possible

synergistic effect from multiple dopants.[23] This is possible since several activation mechanisms are probable for any individual dopant both electronically and structurally.

Among all studied dopant candidates, Ti-doped hematite electrodes have demonstrated promising photoelectrochemical performance toward water oxidation.[14,15,18,23] Although significant improvement in the water oxidation efficiency have been achieved by the incorporation of Ti impurity, the specific cause of Ti-doping effect has not yet clearly determined. A great portion of recent studies therefore has been focused on understanding the mechanism by which Ti-doping improves water oxidation with hematite photoelectrodes.

Zhao *et al*. studied the electrical transport properties of epitaxial Ti-doped films prepared by molecular beam epitaxy with different concentrations of Ti.[3] No significant differences in RHEED patterns of the films were observed, indicating no detectable crystallographic orientation changes upon doping. Refined structural parameters form the XRD data, however, showed that the Ti-doped films exhibit lattice expansion in *c* direction compared to the undoped hematite analogous to the observation by MacFarland *et al.* for Al-doping.[19] Fe K-shell and Ti K-edge XANES measurements confirmed that Ti is incorporated as Ti^{4+} and is substituted for Fe in the lattice.[3] From Hall measurements it was found that carrier concentration and mobility do not scale with Ti concentration, indicating that Ti is not simply acting as an electrical dopant.[3] Huda *et al.* studied electronic structure of pure and transition metal doped hematite.[24] The effect of doping with different transition metals was explained in terms of tuning the band diagram and modification in the unit cell volume, which affects the effective mass of charge carriers hence the transport properties. It was found that Ti incorporation is associated with a reduction in the unit cell volume and

reduced Fe−Fe bond length, which could affect the hopping probability of charge carriers, consistent with the observation by Zhao *et al*.[24] Magnan and co-workers studied epitaxial Ti-doped hematite films by RHEED and EXAFS[25,26] No significant changes were observed in the crystalline quality and crystallographic orientations upon Ti-doping up to 17 %. Structural parameters from the EXAFS simulations for undoped and Ti-doped samples indicated that Ti atoms substitute for Fe atoms and there is no evidence of interstitial Ti. It was also found that Ti incorporation is associated with a slight site distortion, i.e. the distance between Ti and surrounding O and Fe atoms are different from that of pure hematite (shorter Ti−O and longer Ti−Fe bonds). No Fe^{2+} and Ti^{3+} were observed at doping levels up to 17%, in agreement with other reports.[3,24,27] The water oxidation improvement was attributed to the formation of cation vacancies and shift of the valence band, increased carrier concentration and diffusion length.[25,26]

Herein we present a thorough study of the role of Ti-doping in hematite thin films prepared by ALD. Conformal and layer-by-layer growth mechanism of ALD enables controlled introduction of dopant in semiconductor thin films, while maintaining the simple and constant geometry dictated by sample substrate. Using ALD, hematite films of different thickness and Ti concentration were prepared by introduction of one cycle Ti between a desired number of Fe_2O_3 ALD cycles during the deposition. The Ti-doped electrodes where then examined under PEC water oxidation and compared with that of undoped samples of the same thickness. Systematic photoelectrochemical and spectroscopic measurements where then designed to probe the effect of Ti-doping by performing control experiments for possible activation mechanisms. These combined measurement allowed to get a better

insight into the performance enhancement mechanism of doping hematite for PEC water oxidation.

4.3 Experimental

Thin films of Ti-doped hematite were deposited on fluorine-doped tin oxide (FTO)-coated glass substrates (Hartford Glass, 12 Ω cm^{-2}) by atomic layer deposition (Savannah 100, Cambridge Nanotech Inc.) using a modified Fe_2O_3 ALD procedure described in chapter 2. Titanium isopropoxide was used as the titanium precursor to add titanium to the films. Ti source was heated to 80℃ and pulsed for 0.2 s followed by a 0. 015 s pulse of water to oxidize the Ti precursor. The ALD chamber temperature was set to 200℃ for all depositions. The ALD doping procedure is illustrated in Figure A4-1 in the appendix. Both undoped and Ti-doped hematite electrodes were annealed by heating to 500℃ at a rate of 17 ℃ /min, sintered at 500 ℃ for 30 min, and allowed to cool to room temperature over 2 h. By changing the cycle ratio of hematite to Ti, different concentrations of Ti doped samples were prepared. For example a cycle ratio of 1:15 of Ti:Fe_2O_3 indicates one cycle of TiO_2 after every 15 cycles of Fe_2O_3. Since the actual atomic percent is not known for all the samples, for the ease of discussion we use the term “cycle %” or “c%” instead of actual atomic percent of Ti. For example, the c% for incorporating 1 cycle of Ti after every 15 cycles of hematite is 6.25 c%.

The best performance doped hematite film was characterized by X-ray photoelectron spectroscopy (XPS) at Evan Analytical Group (Chanhassen, MN). The XPS data were acquired using a PHI Quantera XPS instrument by utilizing a probe beam of focused, monochromatic Al Kα radiation with a take-off angle of ~45º. The x-rays generate

photoelectrons that are energy analyzed and counted to reveal the atomic composition and chemistry of the sample surface. The in-depth distribution of Ti, Fe, Sn and O elements we reassessed by sputter depth profiling which consisted of alternating between ion beam sputter cycles and acquisition of the spectral regions of interest. The surface morphology of Ti-doped and undoped hematite films were examined by scanning electron microscopy (Carl Zeiss Auriga, Dual Column FIBSEM). Absorbance measurements were made using a Perkin-Elmer Lambda35 UV-vis spectrometer with a Labsphere integrating sphere. The absorbance spectra of the films were measured by illuminating from the substrate-electrode (SE) interface. The incident light was corrected for passing through and being reflected by the substrate. Raman spectroscopy measurements were made LabRam Armis, Horiba Jobin Yvon instrument equipped with 532 nm laser and a microscope to focus the laser light on the film surface.

For PEC measurements, hematite electrodes were masked with a 60 mm Surlyn film (Solaronix) with a 0.28 cm^2 hole to define the active area and to prevent scratching of the thin films. Surlyn films were adhered to the electrodes by heating to 115℃. The Ti doped hematite electrodes were examined in contact with aqueous solutions buffered to pH 6.9 using a 0.1 M phosphate buffer, with 200 mM KCl as supporting electrolyte. A homemade saturated Ag/AgCl electrode was used as a reference electrode and high surface area platinum mesh was used as the counter electrode. The homemade reference electrode was calibrated *vs*. saturated calomel electrode (SCE) (Koslow Scientific) and all potentials were converted to the reversible hydrogen electrode (RHE) scale by the equation $V_{RHE} = V_{Ag/AgCl} + 0.197\ V + pH(0.059\ V)$. Photoelectrochemical and impedance spectroscopy measurements were made with an Eco Chemie Autolab potentiostat coupled with Nova

electrochemical software. Impedance data were gathered using a 10 mV amplitude perturbation of between 10,000 and 0.01 Hz. Data were fit using Zview software (Scribner Associates). The light source was a 450 W Xe arc lamp (Horiba JobinYvon). An AM 1.5 solar filter was used to simulate sunlight at 100 mW cm^{-2} (1 sun). Electrodes were tested by shining light on the electrodes both through the electrode/electrolyte side (front illumination) and through the FTO substrate (back illumination). For back illumination electrodes were clamped to a custom made glass electrochemical cell. For the front side illumination a homemade two-hole cell was used with one of the holes covered with high optical quality quartz, acting as window to direct the light to the electrode surface.

4.4 Results

In order to probe the effect of Ti-doping, initially the PEC performance of undoped and 16.67 c% Ti-doped (where one Ti pulse was introduced after every 5 hematite cycles) hematite electrodes were examined by performing current density, *J*, vs. applied voltage, *V* (*J-V*) measurements in contact with aqueous electrolyte under 1 sun illumination. Initial results indicated a significant improvement in the photocurrent density for Ti-doped electrodes compared to the undoped samples, which is in good agreement with literature reports.[14,15,21] Figure 4-1a shows the current density sampled at 1.8 V *vs.* RHE as a function of total hematite cycles for undoped electrodes and electrodes doped with 16.67 c% of Ti. The photocurrent density of the undoped electrodes increases over the first 600 cycles, and then remains essentially constant. This trend is in good agreement with report by Klahr *et al.*.[6] There was a striking enhancement in the photocurrent for the thinnest electrodes below 600 cycles, however a much smaller enhancement was observed for electrodes prepared

from 600 or more cycles. Specifically, the addition of 16.67 c% of Ti to the 300 cycle electrode more than doubles the photoresponse compared to the undoped analog. Initial results of samples incorporating different ratios of Ti produced similar trends of enhancement vs. electrode thickness. Therefore, since the electrodes prepared with 300 ALD cycles showed the most obvious enhancement from the incorporation of Ti atoms, this thickness was chosen to compare the effect of different doping concentrations. A series of electrodes consisting of 300 cycles of hematite incorporating ratios of Ti from 0 to 25 c% were prepared in order to optimize and understand the nature of the enhancement due to Ti dopants. A plot of the photocurrent density sampled at two different applied potentials as a function of Ti c% is shown in Figure 4-1b. The photocurrent density is enhanced for all doping concentrations compared to the undoped sample. There is a relatively sharp increase in photocurrent density from 0 – 5 c% followed by a slow decline in photocurrent density with increasing the concentrations of Ti. The optimal of Ti concentration was observed for 6.25 c% (corresponding to 1:15 TiO_2:Fe_2O_3 ALD cycle ratio). We therefore focused our investigation on the 300 cycle hematite electrode containing 6.25 c% Ti as described below.

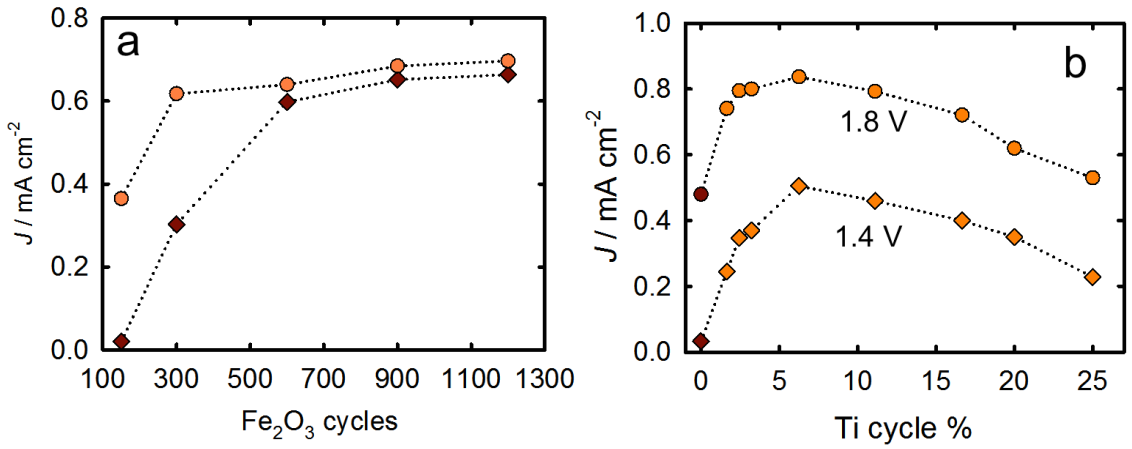

Figure 4-1. a) Photocurrent density at 1.8 V *vs.* RHE as a function of total hematite cycles for undoped hematite (red diamonds) and doped electrodes of 16.67 c% Ti (orange circles). b) Photocurrent density sampled at 1.4 and 1.8 V *vs*. RHE for 300 cycles hematite electrodes containing various concentration of Ti.

XPS depth profiling was performed to characterize the chemical composition and the dopant distribution of the 300 cycle hematite film doped with 6.25 c% Ti. The profiles of the atomic concentration of the elements in this film are shown as a function of normalized depth in Figure 4-2 (a table of these values is provided in the appendix). It can be seen from the Ti profile that the film contains a Ti concentration of ~3 atomic %, which is evenly distributed through the thin film up to the normalized depth of ~200 Å. Thus, the actual atomic concentration of incorporated Ti at this level of doping is ~3% (corresponding to 6.25 c%). A rough estimate of the expected atomic doping concentration can be made from comparing the growth rates of hematite and TiO_2. Given that the ALD growth rate of ~ 0.6 and ~0.15 Å/cycle for Fe_2O_3 and TiO2, repectively, and assuming the growth rates are constant with substrate, each cycle of Ti would produce an atomic percent that is roughly one quarter the cycle percent. ALD growth rates are well-known to depend on the substrate

and other growth conditions, however the measured value of a cycle percent producing approximately half an atomic percent is in reasonable agreement with expectations. An example of an XPS spectrum, measured at the surface, from which the data in Figure 4-2 is gathered, is provided in the appendix. It should be noted that reported depth herein is normalized to the sputter rate of SiO_2, which is not expected to be exactly the same as sputtering hematite. However, assuming the normalized depth of ~200 Å serves as an approximation of the hematite thickness, there is also a significant amount of diffusion of both Fe and Sn atoms across the hematite- FTO interface consisted with the observation discussed in chapter 2.

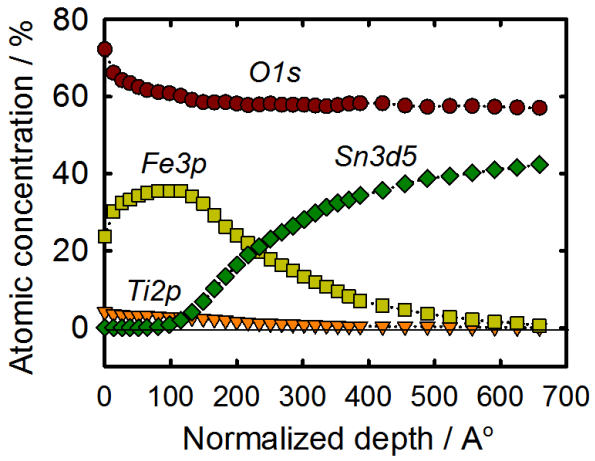

Figure 4-2. XPS depth profiles of a thin film consisting 300 cycles hematite doped with 6.25 c% Ti.

Figure 4-3a shows *J–V* curves of 300 cycle films of undoped hematite and doped with 6.25 c% of Ti in contact with aqueous electrolyte of pH 6.9 under 1 sun illumination. Both the observed photocurrent density and photocurrent onset potential are dramatically improved for the Ti-doped films. A graph of *J–V* curves of 1200 cycle films of undoped and Ti-doped hematite is also shown in Figure 4-3b. The photocurrent density for the doped

electrode is slightly higher; however, the enhancement is much smaller compared to the thinner electrodes under the same conditions. The current onset potential does not change between the thick doped and undoped electrodes. Note that these results are consistent with the results displayed in Figure 4-1. The reason for the different enhancement is discussed below.

SEM images of both doped and undoped hematite films can be seen in the appendix which show the identical morphology of the films. This indicates that a uniform planer morphology has been successfully controlled by the ALD mechanism as expected, for both the doped and undoped electrodes.

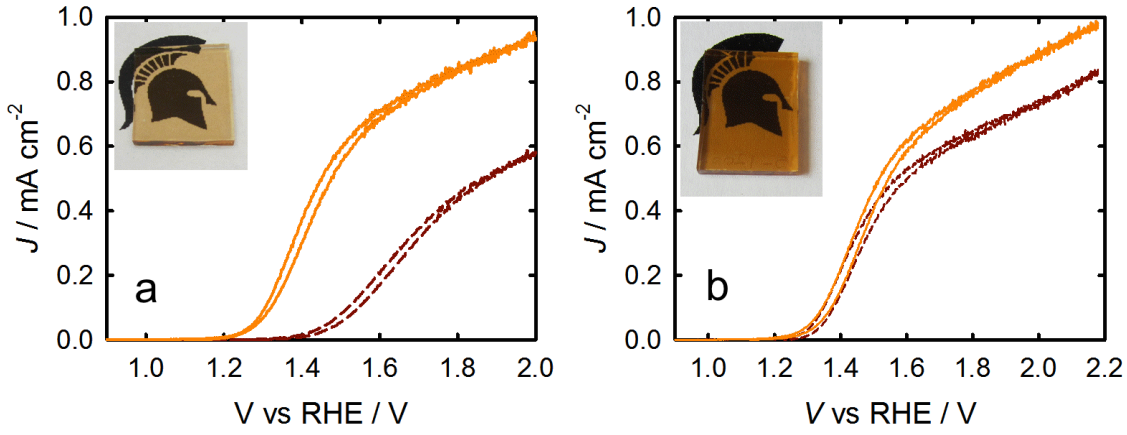

Figure 4-3. *J–V* curves of 300 cycles (a) and 1200 cycles (b) undoped hematite (dashed red) and doped electrodes of 6.25 cycle % Ti (solid orange) in contact with aqueous solution of pH 6.9 and under 1 sun illumination. Inset shows a graphical image of the doped film that produced the *J–V* curve shown in orange.

In order to ensure that the doping was not simply altering the electrode thickness (e. g. increasing the growth rate of hematite), band gap or absorption coefficient, all of which would increase number of minority carriers being generated and increase the current density,

detailed absorption measurements were performed of these films. Figure 4-4 shows the absorptance spectra of the undoped and Ti-doped electrodes which have been corrected for reflection. The absorptance spectra are nominally identical indicating a constant amount and spectral distribution of photons absorbed by the two electrodes. Further, since the absorptance (and absorbance) spectra are identical, it shows that the band gap is not modified from the introduction of such a high degree of impurity, consistent with previous reports.[14,15] The film thickness was measured by ellipsometry to be 20.8 nm for both films. This thickness, combined with the absorbance spectra, produce an absorption coefficient of 2.64×10^5 at 450 nm consistent with previously reported values.[28] In all cases we have found that the electrode thickness is determined by the number of hematite cycles, irrespective of the amount of Ti, as we assumed above. Thus, the improved performance of the Ti doped electrodes is not due to any differences in light absorption due to the band gap, electrode thickness, or absorption coefficient.

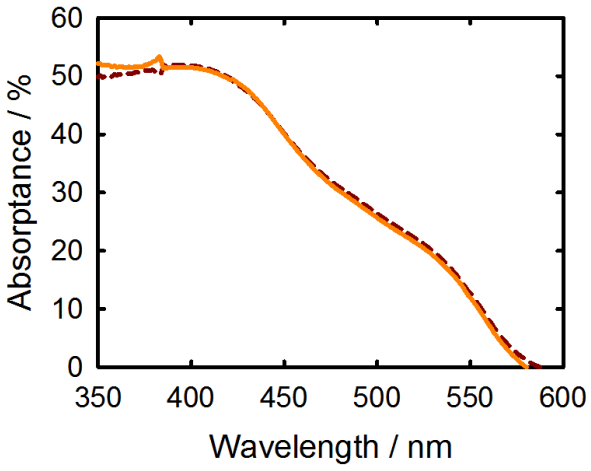

Figure 4-4. Absorptance spectra of 300 cycles undoped (dashed red) and 6.25 c% Ti doped hematite (solid orange) electrodes.

The incident photon to current efficiency (IPCE) at different wavelengths was calculated using photocurrent density produced from water oxidation at 1.8 V vs. RHE under monochromatic illumination. Using the absorptances shown in Figure 4-4 the corresponding absorbed photon to current efficiency (APCE) values were also calculated. Significantly higher IPCE and APCE values were measured over the entire wavelength range as it can be seen from Figure 4-5; indicating higher quantum yield for the Ti doped ultrathin films. We note that the ultrathin Ti doped hematite electrodes demonstrate an APCE as high as 50 % at 400 nm and 1.8V *vs.* RHE, which is comparable to the highest reported.[29]

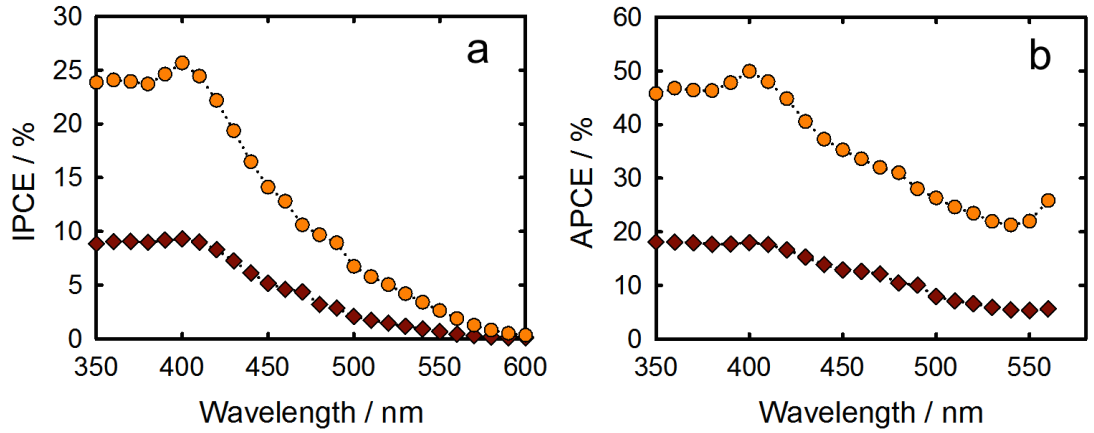

Figure 4-5. IPCE (a) and APCE (b) plots measured at 1.8 V vs. RHE for undoped (red diamonds) and doped with 6.25 c% (orange circles) hematite electrodes of 300 cycles thick.

Since doped hematite electrodes are often examined in the context of PEC water oxidation, the Ti could be enhancing the water oxidation reaction through surface catalysis or by passivating surface states. In order to test this possibility, *J–V* measurements were also performed in an $[Fe(CN)_6]^{3-/4-}$ electrolyte; a fast redox shuttle which has been shown to have

unity hole collection efficiency for undoped electrodes.[30] Figure 4-6a shows typical *J–V* curves for undoped and 6.25 c% Ti doped electrode, each containing 300 ALD cycles of hematite, in contact with the $[Fe(CN)_6]^{3-/4-}$ redox shuttle. There is a significant increase in the photocurrent for the Ti-doped electrodes compared to the undoped, which is in general accord with the water oxidation results shown in Figure 4-3. Assuming hole transfer to $[Fe(CN)_6]^{4-}$ is not the rate limiting step for either doped or undoped hematite electrodes, the increased photocurrent measured for Ti doped hematite electrodes can be attributed to a greater fraction of photogenerated holes reaching the solution interface. The relatively linear voltage dependence of the photocurrent for hematite electrodes in contact with a $[Fe(CN)_6]^{3-/4-}$ based electrolyte has previously been discussed in terms of the product of $\mu\tau/D^2$, where μ is the hole mobility, τ is the hole lifetime and D is the thickness of the electrode.[31] Since the thicknesses of doped and undoped electrodes are the same, the increased slope (and photocurrent) of the *J–V* is due to an increased μ and/or τ. In addition, the constant photocurrent onset potential for doped and undoped electrodes indicates that there is no shift in the conduction band edge due to the Ti dopant. This point is discussed in more detail below.

The higher photocurrent with the Ti-doped electrode in contact with $[Fe(CN)_6]^{3-/4-}$ is attributed to a bulk improvement (an increased μ and/or τ); however under water oxidation conditions the photocurrent of the Ti doped electrode was improved to an even greater extent. For example, at V = 1.7 V *vs.* RHE, the photocurrent density increased from ~0.6 to ~0.8 mA cm^{-2} in the $[Fe(CN)_6]^{3-/4-}$ electrolyte, but increased from ~0.4 to ~0.8 mA cm-2 under water oxidation conditions. Therefore, the Ti dopants must also be improving the water oxidation efficiency; the fraction of holes that oxidize water instead of recombine at

the surface. Possible reasons for this include Ti atoms at the surface acting as a water oxidation catalyst or passivating surface states. In order to check this possibility, undoped hematite electrodes were coated with different number of ALD cycles of Ti. Figure 4-6b shows nominally identical *J–V* curves for hematite electrodes coated with 1, 3 and 5 ALD cycles of Ti which indicates no surface catalytic or surface passivation effects of the Ti atoms. Thicker coatings of TiO_2 decreased the *J–V* response. Further investigation of possible catalytic effect of TiO_2 at the electrode surface was done by depositing different cycles of TiO2 on FTO substrates. These TiO_2 coated electrodes were employed to electrocatalytically oxidize water under dark condition. The onset potential for water oxidation for TiO_2-coated FTO electrodes shifted anodically with increased TiO_2 thickness, indicating no enhancement in water oxidation kinetics resulting from Ti atoms (see the appendix).

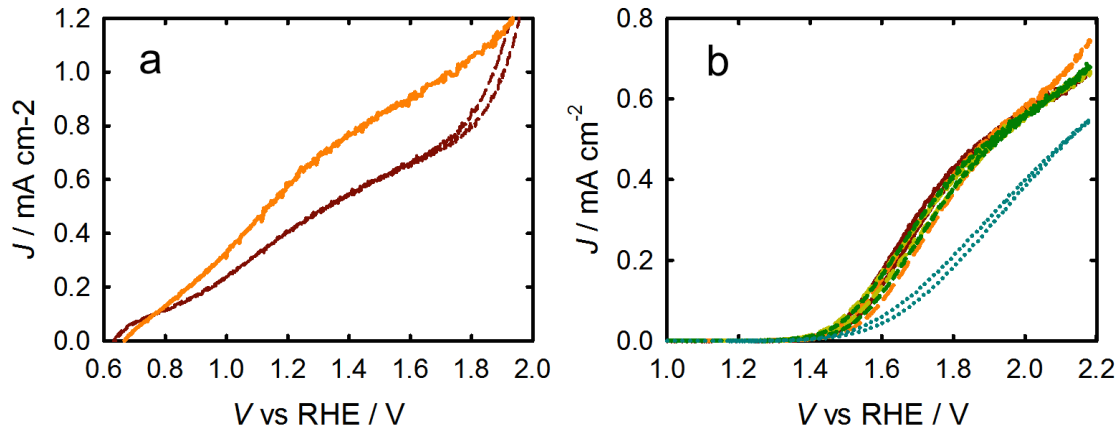

Figure 4-6. a) *J–V* curves of doped (solid orange) and undoped (dashed red) 300 ALD cycle thick hematite electrodes in contact with $[Fe(CN)_6]^{3-/4-}$. b) *J–V* curves of 300 cycle hematite electrodes coated with 1 (orange), 3 (green), 5 (yellow) and 10 (blue) cycles of TiO_2, compared with bare hematite (red) under PEC water oxidation.

Although the water oxidation efficiency is clearly improved for Ti-doped hematite electrodes, there is no indication that Ti at the surface catalyzes water oxidation or passivates surface states. We therefore performed electrochemical impedance spectroscopy (EIS) measurements in order to determine the cause of the higher water oxidation efficiency. We previously reported comprehensive EIS studies on bare undoped hematite electrodes under water oxidation conditions which established an equivalent circuit to interpret the impedance spectra (see the appendix).[32] The equivalent circuit elements include a space charge capacitance of the bulk hematite, C_{bulk}, surface state capacitance, C_{ss}, a resistance which represents the trapping of holes in the surface states, R_{trap}, and charge transfer resistance from the surface states to solution, $R_{ct,ss}$. The results of the fits of the undoped and 6.25 c% Ti doped 300 ALD cycle hematite electrodes can be seen in Figure 4-7. Additional fit results for electrodes containing different Ti concentrations can be found in the appendix. The fit results indicate no significant change in C_{bulk} consistent with Mott-Schottky analysis below. The value of R_{trap} decreases by a factor of ~3 and C_{ss} increases by a factor of ~3 for the Ti-doped electrodes. In addition, $R_{ct,ss}$ decreases by approximately an order of magnitude for the Ti doped electrodes compared to the undoped electrode. All else being equal, a decreased $R_{ct,ss}$ (faster charge transfer from surface states) should produce a lower steady state concentration of trapped holes, C_{ss}. Since we previously attributed the surface trapped holes to water oxidation intermediates such as $Fe^{IV}=O$,[33] a larger C_{ss} indicates a larger number of holes that can be trapped and thus participate in the water oxidation reaction. This interpretation is consistent with the concomitant decrease in $R_{ct,ss}$ with the increase in C_{ss}. Further, a larger number of available surface states to trap holes (participate in water oxidation) is consistent with the smaller resistance of trapping holes, R_{trap}. These combined

results suggest that the effect of the Ti dopants is to produce a hematite surface which has a higher density of active sites for water oxidation.

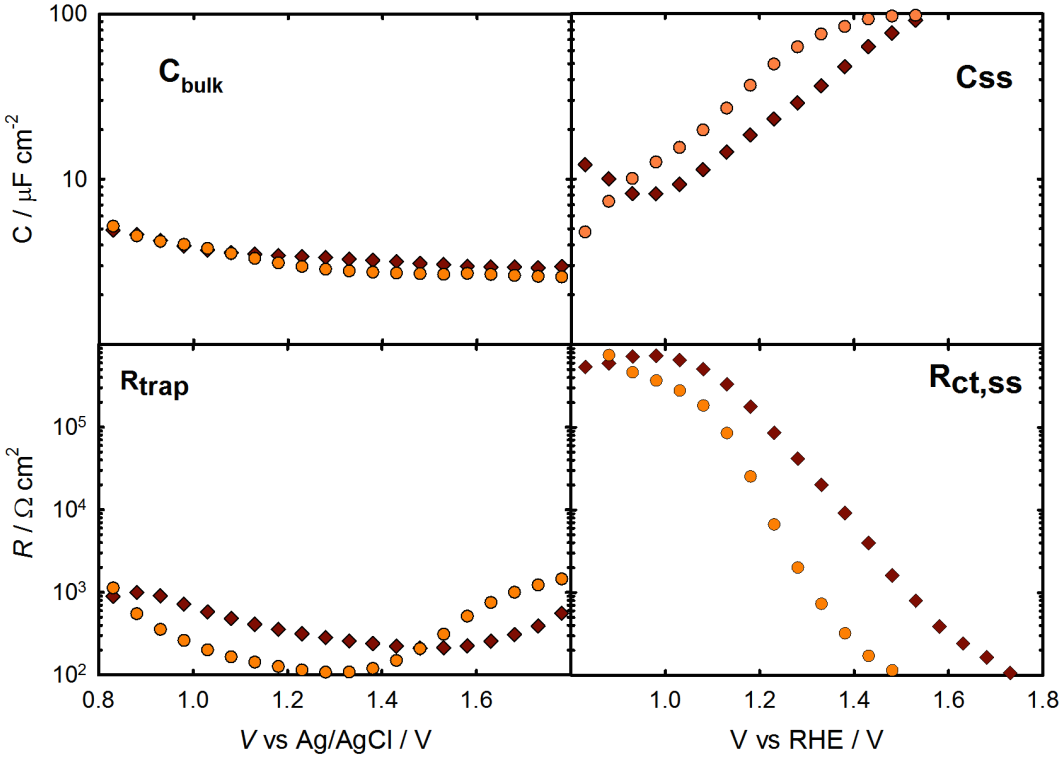

Figure 4-7. Impedance spectroscopy parameters calculated from fitting the EIS data to the equivalent circuit for an undoped (red diamonds) and doped (orange circles) 300 cycles electrode.

Another possible role of the Ti dopants is that of the literal definition of the word "dopants". That is, Ti atoms can act as an electronic dopant which increases the number of majority carriers (electrons) in the hematite structure. Figure 4-8 shows Mott-Schottky plots prepared from EIS data measured in the dark with undoped and 6.25 c% Ti doped 1200 ALD cycle hematite electrodes immersed in an aqueous electrolyte. Relatively thick samples were used for the Mott-Schottky analysis to ensure that the depletion region would

be completely developed for the examined potential range. The flat band potential, E_{fb}, and dopant density, N_D, were calculated from the Mott-Schottky equation:

$$\left(\frac{A_s}{C_{bulk}}\right)^2 = \frac{2}{q\kappa\varepsilon_0 N_D}\left(E\text{-}E_{fb}\text{-}\frac{KT}{q}\right) \quad (4\text{-}1)$$

Where A_s is the surface area of the electrode, N_D is the dopant density, κ is the dielectric constant of the semiconductor and ε_0 is the permittivity of the vacuum. The dielectric constant values quoted in the literature for hematite vary widely from 12–120; we use a value of 32 based on the reported by Glasscock *et al.* as this is consistent with our previous measurements.[6,34] The calculated E_{fb} of 0.850 for the doped and 0.865 V *vs.* RHE for the undoped electrode indicates no significant changes in the band edge positions upon doping. This is in agreement with the constant photocurrent onset potential measured in contact with a $[Fe(CN)_6]^{3-/4-}$ electrolyte (Figure 4-6a) and the constant C_{bulk} vales of the 300 ALD cycle electrodes (Figure 4-7). We note that the calculated E_{fb} from the Mott-Schottky plot in Figure 4-8 is somewhat more positive that the photocurrent onset potential in Figure 4-6a which we attribute to differences in electrode preparation (e.g. thickness) and the facts that excess carriers generated under illumination can shift the E_{fb} to more negative potentials. Mott-Shottky plots derived from C_{bulk} vales of the 300 ALD cycle films in the dark produce a flat band potential of ~0.7 V vs RHE, consistent with the photocurrent onset potential of those electrodes (see the appendix). In addition, by comparing the slope of Mott-Schottky plots the N_D values were found to be essentially unchanged, corresponding to 4.0×10^{18} and 4.4×10^{18} cm^{-3} for undoped and Ti doped electrodes, respectively. If Ti acts as electrical dopant, with each Ti atom donating an electron to the lattice, the dopant density resulting from incorporating 3% of Ti atoms is ~10^{21} cm^{-3}, which is three orders of magnitude higher

than the experimentally measured value. Thus, Ti is clearly not acting as an electronic dopant.

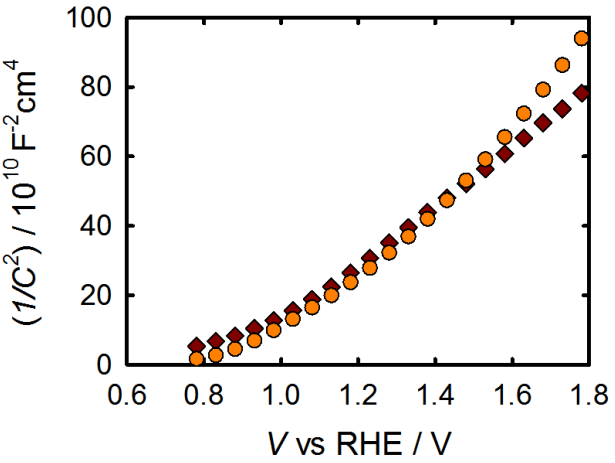

Figure 4-8. Mott-Schottky plots of undoped hematite (red diamonds) and doped with 6.25 c% Ti (orange circles) 1200 ALD cycle electrodes in contact with aqueous electrolyte of pH 7 in dark.

4.5 Discussion

Employing ALD to prepare planer thin film hematite electrodes with and without controlled amounts of Ti atom dopants allowed us to perform systematic investigations of the effect of the Ti dopants with a constant electrode morphology due to ALD's epitaxial, layer-by-layer growth mechanism. A combination of absorption spectroscopy and ellipsometry measurements showed that the electrode thickness, absorption coefficient and band gap were invariant upon the addition of Ti atoms. In all cases, however, we found the PEC performance was increased when Ti atoms were incorporated. The enhancement varied as a function of electrode thickness, with the greatest enhancement found for the thinnest electrodes. Comparison of the PEC performance when a fast redox shuttle showed that

doping increased the number of holes that reach the electrolyte interface, which is attributed to an increased hole mobility and/or increased hole lifetime (slower recombination) in the bulk. This result allows us to conclude that the incorporation of Ti atoms alters the bulk properties of hematite. Mott-Schottky analysis allowed us to rule out the possibility that Ti was acting as an electronic dopant, thus the effect is something else. Since the PEC enhancement is greatest for the thinnest electrodes, the alteration in bulk properties is most significant for the hematite layer nearest the FTO contact.

There have been several previous reports which attributed the relatively poor PEC behavior of ultrathin hematite films to the formation of a "dead layer" at the hematite–FTO interface.[29,35] As discussed in chapter 2 the dead layer is resulting from an imperfect crystal layer at the hematite–FTO interface. We demonstrated that the dead layer effect can be effectively mitigated through incorporation of a Ga_2O_3 or Nb_2O_5 underlayer. Interestingly the performance improvement of the ultrathin thin film with Ti-doping was to the same extent as that of the underlayers. These results suggest that Ti-doping effect is primarily alleviating the dead layer, as it is highest for the thinnest films. This assignment is consistent with the fact that thicker hematite films are not significantly improved upon the incorporation of Ti atoms; the dead layer should be much less significant for thicker films as the dead layer is farther away from the active depletion region. It is not clear how the presence of Ti atoms alleviates the dead layer, however.

In addition to the dead layer effect, comparisons of the PEC performance enhancement with a fast hole collector and under water oxidation conditions indicated that the water oxidation efficiency of holes that reach the electrolyte interface is also improved. This effect is also only significant for the thinnest electrodes (300 ALD cycles or 20.8 nm). Thus, there

is also a dead surface effect. The specific effect of the different surfaces on the water oxidation efficiency was elucidated through impedance spectroscopy. The combination of an order of magnitude lower $R_{ct,ss}$ with the concomitant increase in C_{ss} indicates that there are more active surface species on a Ti-doped hematite electrode which can participate in water oxidation. This makes sense since the crystallographic orientation of the surface atoms will be at least partially determined by the bulk crystal structure; a more crystalline hematite film should present a more ordered surface. Since we assign the first step in water oxidation with hematite electrodes as Fe^{III}-OH terminations being oxidized to form an Fe^{IV}=O species, we hypothesize that Ti doping results in a higher surface concentration of Fe^{III}-OH capable of participating in further water oxidation reactions. Computations by Trainor *et al.* suggested that the $(OH)_3$–Fe–H_3O_3–R surface termination of the (0001) hematite surface was active towards water oxidation while other surface terminations such as $(OH)_3$–R was not.[36] Recently Carter et. al. reported a computational study of water oxidation on the fully hydroxylated (0001) hematite surface, which suggested this is the active hematite surface, and other surface terminations (defects) may reduce the water oxidation efficiency.[37] These works are both in good agreement with our suggestion that the thin undoped surface may have a lower fraction of active, fully hydroxylated, surface species present compared to the doped surface. In addition, we were able to control for possible catalytic and surface state passivation effects of Ti on the hematite surface by depositing TiO_2 on undoped hematite. No enhancement was observed, thus we were able to rule out catalysis or surface passivation effects of Ti doping. As mentioned the mechanism by which Ti-doping activates the bulk of the thin films is not trivial to address. Our structural study however, led to an interesting point. Shown in Figure 4-9 are Raman spectra

of undoped and Ti-doped hematite films of different Ti-concentration and thickness. In the Raman spectrum of Ti-doped electrode showed an interesting feature: an extra peak at 658 cm^{-1} that emerges upon Ti-doping. This peak is often observed for doped and undoped hematite electrodes around 657-660 cm^{-1} which has been assigned to magnetite and maghemite phase impurities.[38–40] This peak was also observed by several group for hematite electrodes upon doping with Ti, Pt, and Si which was assigned to strain-induced distortion and surface defects.[15,17,22] Several experimental and theoretical spectroscopic studies on hematite, however, assign this peak to an IR active and Raman inactive phonon mode which is not observed in the Raman spectra of pure hematite phase.[41–45] This Raman inactive mode is activated upon relaxation of lattice symmetry and hence the selection rules.[42–44] We therefore, assign 658 cm^{-1} peak to distortion-induced Raman mode activated upon doping. This is consistent with the changes in cell parameters (unit cell contraction) observed by Zhao *et al*.,[3] Huda *et al*.,[24] and Magnan *et al*.,[25] for Ti-doped and McFarland and co-workers[19,22] for Pt and Al-doped hematite samples. We note that FeO_6 octahedra in hematite is slightly distorted due to face sharing requirement of Fe_2O_9 units.[46,47] Substitution of Ti for Fe atoms thus further enhances the O_h to C_{3V} distortion leading to the relaxation of the octahedral symmetry and activation of this phonon mode in the Raman spectra. Trigonal distortion upon doping can potentially modify the distances between neighboring atoms, which in turn alters the hopping probability of electron and holes through the bulk. Moreover, substitution of Ti for Fe atoms results in the mixing of Ti s and d orbitals with Fe and O band which further modifies the selection rules and charge transfer properties through neighboring metal centers. Distortion to a more trigonal structure can also modify the ligand field environment around the metal centers and thus alter the orbital splitting and

hybridization. Although it is not trivial to clearly determine this electronic effect, possible modification of band diagram can result in an enhanced carrier dynamics in the valence and conduction band as well as bulk/surface trap passivation. We therefore conclude Ti-doping is enhancing the charge separation in bulk hematite mainly through a structural distortion effect, i.e. trigonal distortion, which result in the enhanced charge separation (bulk improvement) and enhanced charge collection on the surface by exposing more active sites toward oxidation and/or reducing surface traps density hence surface recombination.

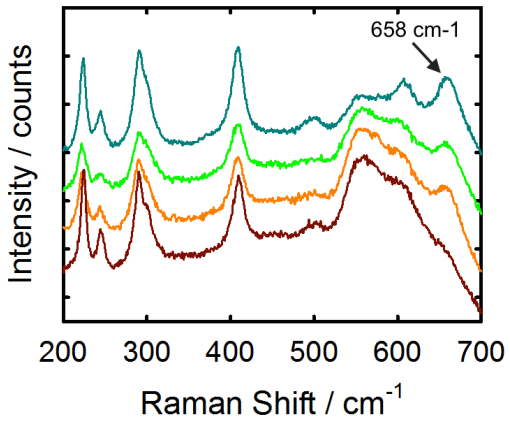

Figure 4-9. Raman spectra of undoped (red) and Ti-doped (orange) hematite thin films deposited on FTO, showing the emergence of distortion-induced peak at 658 cm^{-1} upon doping. Higher Ti concentration (green, 6% Ti) did not change the intensity of the peak while increasing the thickness (cyan, ~ 40 nm) resulted in enhanced peak intensity.

4.6 Conclusion

In this work ALD was used to make Ti doped hematite electrodes which were compared with undoped hematite electrodes. Due to ALD's epitaxial growth mechanism, we were able to control the morphology of the hematite films and separate morphological

changes induced from incorporation of a large concentration of dopants from other effects. We showed that incorporation of a relatively large percentage of Ti impurities to hematite electrodes dramatically enhances the PEC water oxidation performance of hematite electrodes. This performance enhancement was a combination of improved bulk properties (hole collection length) and surface properties (water oxidation efficiency). These improvements are attributed to a resurrection of a dead layer and dead surface, respectively, by the Ti dopant atoms. Optimized Ti dopant concentration and electrode thickness allowed APCE's as high as 50 % to be achieved for water oxidation.

APPENDIX

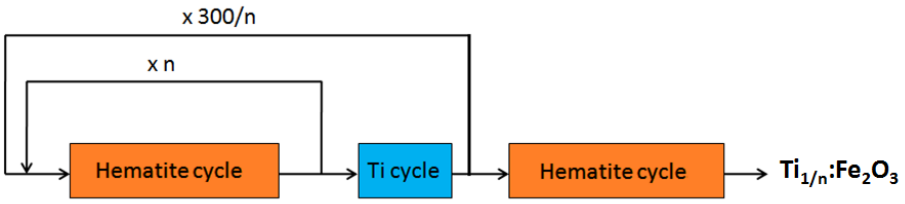

Figure A4-1. Schematic ALD doping procedure employed to deposit Ti-doped Fe2O3. A Hematite cycle comprises a pulse of ferrocene followed by a pulsing sequence of water/ozone as an oxidant. A Ti cycle represents a titanium isopropoxide pulse followed by a pulse of water as an oxidant.

	Atomic concentration (%)			
Depth(°A)	O1s	Ti2p	Fe3p	Sn3d
0	72.3	4.1	23.7	0
13	66.2	3.5	30.2	0
26	64.3	3.3	32.4	0
38	63.5	3.2	33.3	0
51	62.5	3.1	34.3	0
64	61.7	3.2	35	0.1
81	61.2	3	35.5	0.3
98	60.9	2.8	35.5	0.8
115	60.2	2.7	35.5	1.9
132	59.2	2.6	34.1	4
149	58.6	2.4	32.2	6.8
166	58.5	2.2	29.2	10.1
183	58.6	1.9	26.2	13.3
200	58.2	1.6	24	16.3
217	57.8	1.4	22	18.9
234	58	1.2	19.7	21
251	58.2	1.1	17.7	23
268	57.9	1	16.2	24.8
285	57.9	0.9	14.8	26.4
302	57.9	0.8	13.2	28.1
319	57.7	0.7	11.9	29.8
336	57.5	0.6	10.7	31.3
353	57.8	0.5	9.4	32.4
370	58.2	0.4	8.1	33.2
387	58.3	0.4	6.9	34.4
421	58.3	0.3	5.7	35.7
455	57.7	0.3	4.6	37.4
489	57.4	0.3	3.6	38.8
523	57.6	0.2	2.8	39.4
557	57.6	0.1	2.1	40.2
591	57.4	0.1	1.5	41
625	57.2	0	1.2	41.6
659	57.1	0	0.5	42.4

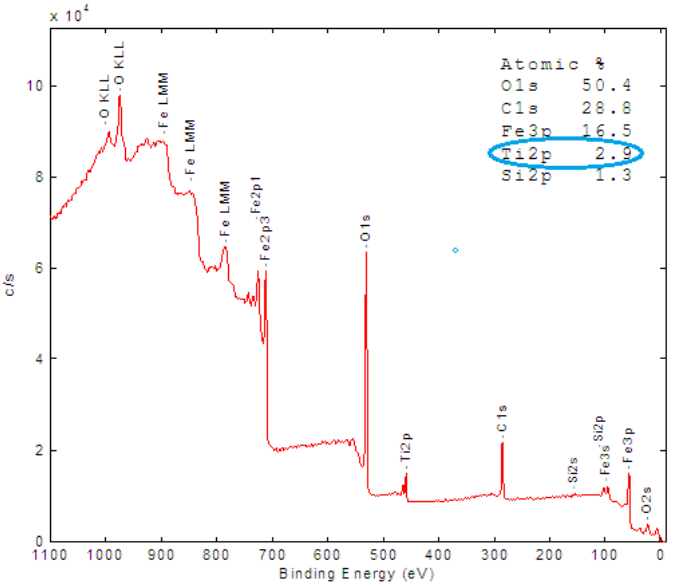

Figure A4-2. Table of atomic concentration values of XPS depth profiling and a XPS surface survey spectrum of Ti doped hematite thin film.

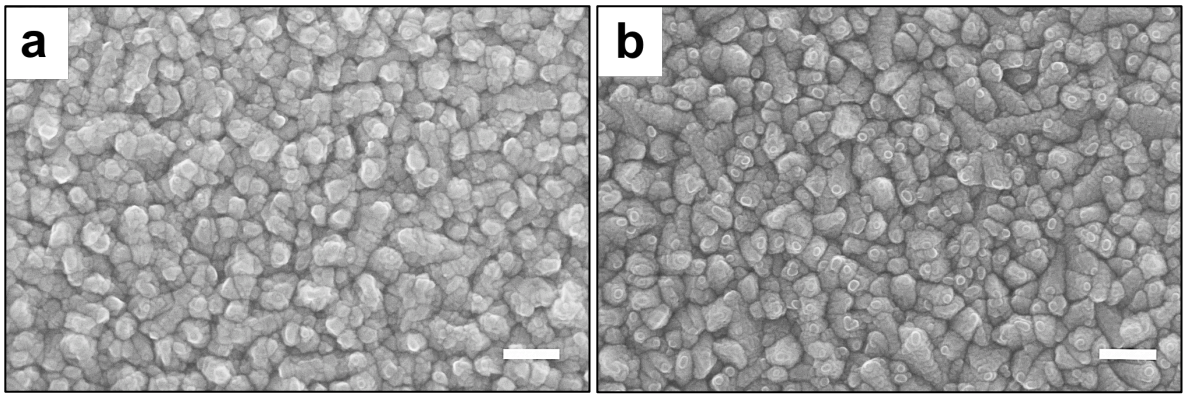

Figure A4-3. The SEM images of undoped and Ti-doped hematite films. The scale bar is 500 nm.

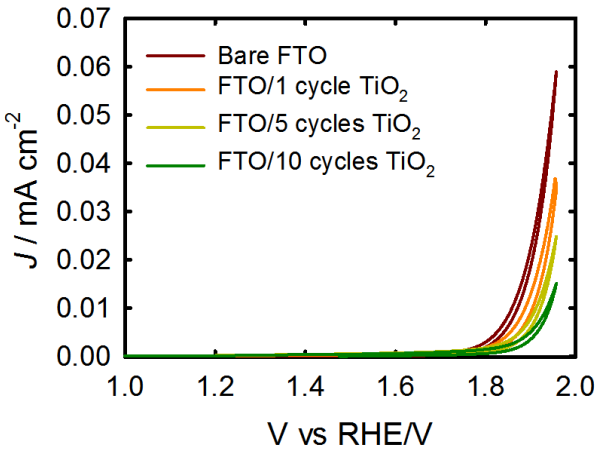

Figure A4-4. *J–V* curves of FTO electrode coated with different ALD cycles of TiO_2.

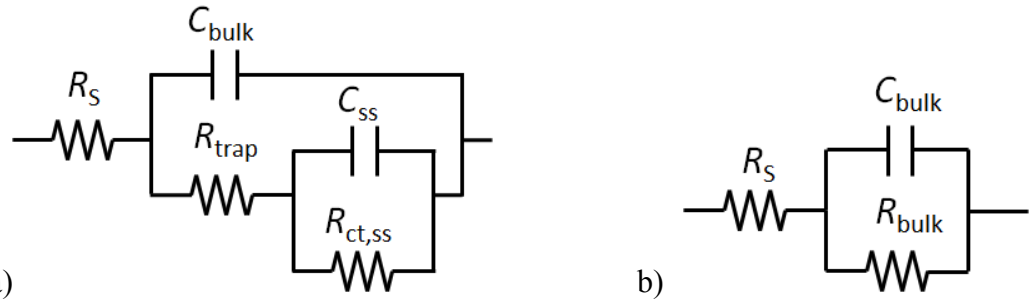

Figure A4-5. Equivalent circuits used to fit the experimental EIS data under illumination (a) and in dark (b).

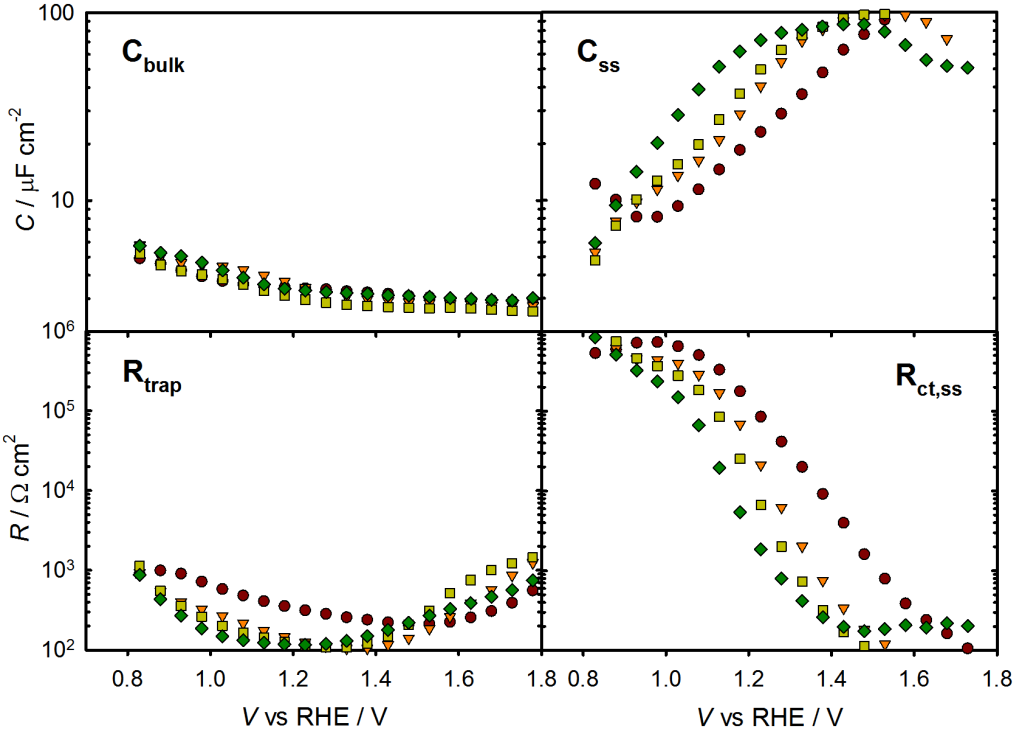

Figure A4-6. Additional EIS results for different Ti dopant concentrations calculated from fitting the experimental data to the equivalent circuits for 300 cycles thick electrodes, under water oxidation and 1 sun illumination with undoped hematite (red circles) of doped of 3.22 (orange triangles) 6.25 (yellow squares) and 11.11 (green diamonds) c% Ti.

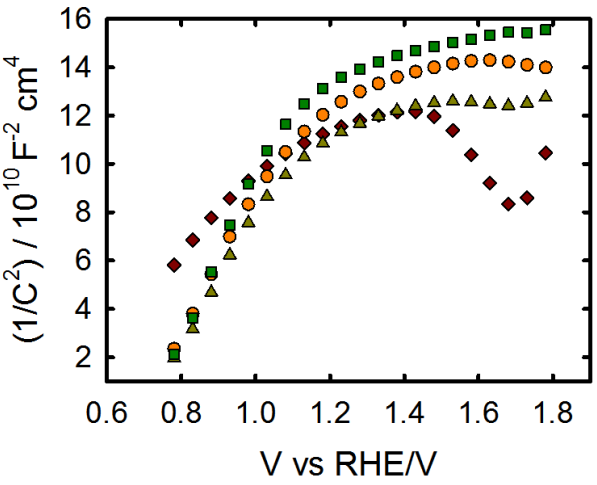

Figure A4-7. Mott-Schottky plots of 300 cycles thick electrodes, under water oxidation in dark for undoped hematite (red circles) and doped of 3.22 (yellow cubes) 6.25 (orange triangles) and 11.11 (green diamonds) c% Ti.

REFERENCES

REFERENCES

(1) Rosso, K. M.; Smith, D. M. a.; Dupuis, M. *J. Chem. Phys.* **2003**, *118*, 6455.

(2) Iordanova, N.; Dupuis, M.; Rosso, K. M. *J. Chem. Phys.* **2005**, *122*, 144305.

(3) Zhao, B.; Kaspar, T. C.; Droubay, T. C.; McCloy, J.; Bowden, M. E.; Shutthanandan, V.; Heald, S. M.; Chambers, S. a. *Phys. Rev. B* **2011**, *84*, 245325.

(4) Liao, P.; Toroker, M. C.; Carter, E. A. *Nano Lett.* **2011**, *11*, 1775.

(5) Bosman, a. J.; van Daal, H. J. *Adv. Phys.* **1970**, *19*, 1.

(6) Klahr, B. M.; Martinson, A. B. F.; Hamann, T. W. *Langmuir* **2011**, *27*, 461.

(7) Liang, Y.; Enache, C. S.; van de Krol, R. *Int. J. Photoenergy* **2008**, *2008*, 1.

(8) Jarrett, H. S. *J. Appl. Phys.* **1981**, *52*, 4681.

(9) Warren, S. C. In *Photoelectrochemical Hydrogen Production*; 2011; Vol. 102, pp. 293–316.

(10) Gardner, R. F. G.; Sweett, F.; Tanner, D. W. *J. Phys. Chem. Solids* **1963**, *24*, 1183.

(11) Liao, P.; Toroker, M. C.; Carter, E. a. *J. Appl. Phys.* **2012**, *112*, 013701.

(12) Hu, Y.-S.; Kleiman-Shwarsctein, A.; Stucky, G. D.; McFarland, E. W. *Chem. Commun.* **2009**, 2652.

(13) Ling, Y.; Wang, G.; Wheeler, D. a; Zhang, J. Z.; Li, Y. *Nano Lett.* **2011**, *11*, 2119.

(14) Wang, G.; Ling, Y.; Wheeler, D. a; George, K. E. N.; Horsley, K.; Heske, C.; Zhang, J. Z.; Li, Y. *Nano Lett.* **2011**, *11*, 3503.

(15) Glasscock, J. a.; Barnes, P. R. F.; Plumb, I. C.; Savvides, N. *J. Phys. Chem. C* **2007**, *111*, 16477.

(16) Hu, Y.; Kleiman-shwarsctein, A.; Forman, A. J.; Hazen, D.; Park, J.; Mcfarland, E. W.; Barbara, S. **2008**, 3803.

(17) Cesar, I.; Sivula, K.; Kay, A. *J. Phys. Chem. C* **2009**, *113*, 772.

(18) Zandi, O.; Klahr, B.; Hamann, T. *Energy Environ. Sci.* **2013**, *6*, 634.

(19) Kleiman-Shwarsctein, A.; Huda, M. N.; Walsh, A.; Yan, Y.; Stucky, G. D.; Hu, Y.-S.; Al-Jassim, M. M.; McFarland, E. W. *Chem. Mater.* **2010**, *22*, 510.

(20) Kleiman-Shwarsctein, A.; Hu, Y.-S.; Forman, A. J.; Stucky, G. D.; McFarland, E. W. *J. Phys. Chem. C* **2008**, *112*, 15900.

(21) Zhang, P.; Kleiman-Shwarsctein, A.; Hu, Y.-S.; Lefton, J.; Sharma, S.; Forman, A. J.; McFarland, E. *Energy Environ. Sci.* **2011**, *4*, 10201028.

(22) Hu, Y.; Kleiman-shwarsctein, A.; Forman, A. J.; Hazen, D.; Park, J.; Mcfarland, E. W.; Barbara, S. *Chem. Mater.* **2008**, *20*, 3803.

(23) He, J.; Parkinson, B. A. *ACS Comb. Sci.* **2011**, *13*, 399.

(24) Huda, M. N.; Walsh, A.; Yan, Y.; Wei, S.-H.; Al-Jassim, M. M. *J. Appl. Phys.* **2010**, *107*, 123712 1.

(25) Magnan, H.; Stanescu, D.; Rioult, M.; Fonda, E.; Barbier, A. *Appl. Phys. Lett.* **2012**, *101*, 133908 1.

(26) Rioult, M.; Magnan, H.; Stanescu, D.; Barbier, A. *J. Phys. Chem. C* **2014**, *118*, 3007.

(27) Kronawitter, C. X.; Zegkinoglou, I.; Shen, S.-H.; Liao, P.; Cho, I. S.; Zandi, O.; Liu, Y.-S.; Lashgari, K.; Westin, G.; Guo, J.-H.; Himpsel, F. J.; Carter, E. a.; Zheng, X. L.; Hamann, T. W.; Koel, B. E.; Mao, S. S.; Vayssieres, L. *Energy Environ. Sci.* **2014**, *7*, 3100.

(28) Sivula, K.; Le Formal, F.; Grätzel, M. *ChemSusChem* **2011**, *4*, 432.

(29) Hisatomi, T.; Dotan, H.; Stefik, M.; Sivula, K.; Rothschild, A.; Grätzel, M.; Mathews, N. *Adv. Mater.* **2012**, *24*, 2699.

(30) Klahr, B. M.; Hamann, T. W. *J. Phys. Chem. C* **2011**, *115*, 8393.

(31) Klahr, B. M.; Hamann, T. W. *Appl. Phys. Lett.* **2011**, *99*, 063508 1.

(32) Klahr, B.; Gimenez, S.; Fabregat-Santiago, F.; Bisquert, J.; Hamann, T. W. *J. Am. Chem. Soc.* **2012**, *134*, 16693.

(33) Klahr, B.; Gimenez, S.; Fabregat-Santiago, F.; Bisquert, J.; Hamann, T. W. *Energy Environ. Sci.* **2012**, *5*, 7626.

(34) Glasscock, J. A.; Barnes, P. R. F.; Plumb, I. C.; Bendavid, A.; Martin, P. J. **2008**, *516*, 1716.

(35) Hisatomi, T.; Brillet, J.; Cornuz, M.; Le Formal, F.; Tétreault, N.; Sivula, K.; Grätzel, M. *Faraday Discuss.* **2012**, *155*, 223.

(36) Trainor, T. P.; Chaka, A. M.; Eng, P. J.; Newville, M.; Waychunas, G. a.; Catalano, J. G.; Brown, G. E. *Surf. Sci.* **2004**, *573*, 204.

(37) Liao, P.; Keith, J. A.; Carter, E. A. *J. Am. Chem. Soc.* **2012**, *134*, 13296.

(38) Campbell, I. H.; Fauchet, P. M. *Solid State Commun.* **1986**, *58*, 739.

(39) Shebanova, O. N.; Lazor, P. *J. Solid State Chem.* **2003**, *174*, 424.

(40) Nie, X.; Li, X.; Du, C.; Huang, Y.; Du, H. *J. Raman Spectrosc.* **2009**, *40*, 76.

(41) Bersani, D.; Lottici, P. P.; Montenero, A. *J. Raman Spectrosc.* **1999**, *360*, 355.

(42) Jubb, A. M.; Allen, H. C. *ACS Appl. Mater. Interfaces* **2010**, *2*, 2804.

(43) Onari, S.; Arai, T.; Kudo, K. *Phys. Rev. B* **2008**, *16*, 1717.

(44) Mccarty, K. F.; April, R.; Rowell, J. M. *Solid State Commun.* **1988**, *68*, 799.

(45) Mccarty, K. F.; Boehme, D. R.; Laboratories, S. N. *J. Solid State Chem.* **1989**, *27*, 19.

(46) Sherman, D. M.; Waite, D. T. *Am. Mineral.* **1985**, *70*, 1262.

(47) Sivula, K.; Zboril, R.; Le Formal, F.; Robert, R.; Weidenkaff, A.; Tucek, J.; Frydrych, J.; Grätzel, M. *J. Am. Chem. Soc.* **2010**, *132*, 7436.

Chapter 5:

High Performance Hematite Electrodes Prepared by Electrodeposition

5.1 Abstract

Hematite electrodes with variable morphologies were prepared *via* a simple electrodeposition (ED) method. The photoelectrochemical (PEC) properties of planar and nanostructured electrodes were examined under PEC water oxidation and compared to that of planar analogs prepared by atomic layer deposition (ALD). The water oxidation performance of electrodeposited planar thin films was surprisingly comparable to nanostructured electrodeposited both of which greatly outperformed the ALD made planar films. Better performance is attributed to variations in the crystallographic properties which result in enhanced hole transport and collection as confirmed by photoelectrochemical and electrochemical impedance spectroscopy measurements and structural analysis. Results indicate a nonzero hole diffusion length for the electrodeposited hematite thin films in contrast to the ALD counterparts. Electrodeposited hematite thin films modified with Co-Pi demonstrated near unity hole collection efficiency producing the highest photocurrent among reported planar electrodes. This approach thus provides a simple and scalable approach to prepare high performance thin film absorber hematite electrodes for solar water splitting.

5.2 Introduction

As discussed in previous chapters, due to a very short hole collection length in hematite, nanostructuring is generally adopted to decouple the feature size and light absorption depth and thus maximizing light absorption while maintaining the bulk within hole collection length.[1–6] Surface modification on the other hand is done primarily by addition of surface coatings to suppress surface recombination and/or enhance water oxidation kinetics.[7–11] Combination of bulk and surface modification strategies produced promising photocurrent of 3-4 mA cm^{-2} at 1.23 V *vs.* RHE in the state of the art systems.[7,12] The water oxidation photocurrent onset of bare hematite in these systems however, has been consistently very positive of the flat band potential which is generally attributed to surface recombination.[13–15] It was demonstrated in chapter 3 that near unity hole collection can be obtained for hematite thin films annealed at 800 °C, producing photocurrent onset just positive of the flat band potential.[16] Most recently Jang and Wang *et al.* employed a combination of high temperature annealing and a $NiFeO_x$ catalyst which produced breakthrough onset potential of 0.45 V *vs*. RHE on a solution processed hematite electrode.[17] Wang's system enabled unassisted water splitting when coupled with an amorphous Si at efficiency of 0.91%. Even with recent progresses however, the photocurrent generated with hematite electrode is far less than what could potentially be generated with a band gap of 2.1 eV (~12 mA cm^{-2}) especially at low applied bias where high photocurrent is desired for a tandem EC cell design.[18] Although low photocurrent has usually been associated with a short hole diffusion length and thus bulk recombination, it was demonstrated that even for the very thin films where the entire bulk of the electrode is within the depletion region, the absorbed photon to current conversion efficiency (APCE) is low (chapter 3).[16,19] This indicates that diffusion

length is essentially zero and there is strong depletion region recombination. Depletion region recombination results in a voltage dependent photocurrent of hematite thin films electrodes,[16,20] which further reduces the fill factor of the *J-V* curves resulting in a low photocurrent at low applied bias. Realizing high photocurrent at low applied potential thus requires effective suppression of depletion region recombination and minimizing bulk recombination. There are several strategies to enhance charge separation presumably by enhancing hole conductivity. One strategy is deposition of highly crystalline hematite electrodes. This was demonstrated by Warren *et al*.[21] for nanostructures with reduced density of high angle grain boundaries and Kim *et al*.[12] for single crystal mesoporus hematite, which both produced record photocurrent. Another strategy is fabrication of highly doped hematite electrodes. Higher dopant density could in principal enhance charge separation in the bulk and most importantly hole transport in the depletion region by placing a shaper band bending at the interface.[22,23]

Here we report a comparative study of hematite electrodes prepared *via* two different routes having planar and nanostructured morphology. An electrodeposition (ED) method was utilized to fabricate planar thin film and nanostructured electrodes simply by tuning the deposition pH and temperature, following a previous report.[24] The water oxidation performance of electrodeposited planar electrodes were then compared to that of ALD prepared hematite thin film analogs. In comparison to ALD benchmark thin films, hematite electrodes prepared *via* ED demonstrated significantly higher water oxidation activity reflected in both the photocurrent onset potential and magnitude. The better performance was found that is a combination of enhanced bulk charge transport and surface hole collection efficiency.

5.3 Experimental

5.3.1 Electrode preparation

Hematite electrodes were prepared *via* electrodeposition of FeOOH from $FeCl_2$ (aq) solution using a modified version of a previously reported method.[24] Briefly F:SnO_2 (FTO)-coted alumnioborosilicate glass substrates (Solaronix, 10 Ω/sq) were cleaned by sonication in soap, water, and isopropyl alcohol each for 10 min followed by blow drying with a stream of N_2. Cleaned FTO were used as the working electrode in a custom made electrochemical cell along with a Pt mesh and an Ag/AgCl as counter and reference electrodes, respectively. Two pHs (acidic and neutral) were chosen for deposition as the solution pH strongly affected the deposition mode thus the electrode morphology.

Electrodeposition of planar thin films in acidic condition (a-ED). Acidic deposition was performed simply in 0.1 M $FeCl_2.4H_2O$ (pH= ~ 4.2) at 60 °C by applying 1.3 V *vs*. Ag/AgCl reference electrode under gentle stirring. The thickness of Fe_2O_3 was determined by the deposition time (i.e. the total amount of charge passed). Acidic depositions produced planar films with excellent uniformity and reproducibility over studied substrates size as large as ~10 cm^2 (Figure A5-1). This method is therefore excellent for fabricating planar uniform thin film hematite coatings on TCO substrates with different morphologies.

Electrodeposition of nanostructured FeOOH in neutral condition (n-ED). Neutral deposition was performed in slightly different conditions as the Fe^{2+} ions are not stable and soluble in neutral and basic pHs. Deposition solution contained 0.02 M $FeCl_2.4H_2O$ and 3 M NH_4Cl. High concentration of NH_4Cl was used to stabilize the Fe^{2+} ions according to the previous report.[24] This solution was purged with N_2 for at least 30 min before adjusting the

pH to 7.5 by addition of KOH. Electrodeposition was then performed in the room temperature under N_2 constant atmosphere (to minimize the oxidation of Fe^{2+} ions) and gentle stirring. The FTO working electrode was biased to 0.0 V *vs*. Ag/AgCl for neutral deposition. Lower applied potential (compared to 0.3 V in utilized by Spray *et al.*[24]) used herein was found that results in the better uniformity and more controllable morphology. The amount of the FeOOH was controlled by the deposition time.

ALD of planar Fe_2O_3 thin films. Analogous thicknesses of Fe_2O_3 were deposited by ALD on FTO substrates using the method described in chapter 2.[19]

Annealing. As deposited films were annealed either at 500 °C (2 h) or 800 °C (10 min) in air to convert the amorphous FeOOH to crystalline α-Fe_2O_3. Annealing at 500 °C was done by ramping the furnace temperature at 20 degree/min to 500 °C, holding for 2h and then cooling to room temperature over 2h . For annealing at 800 °C, electrode were fixed on a flat Si wafer surface which were then placed in a pre-heated furnace at 800 °C for a short annealing time (5-20 min) followed by cooling at room temperature.

Electrocatalyst deposition. Cobalt-phosphate (Co-Pi) deposition were carried out using a photoelectrondeposition method reported previously.[8,25] Hematite electrodes were immersed in a solution containing 0.5 mM $Co(NO_3)_2 \cdot 6H_2O$ in a 0.1 M phosphate buffer (pH 6.9). A bias of 0.1 V *vs.* Ag/AgCl was applied under 1 sun illumination. The thickness of the Co-Pi layer was controlled by varying the deposition time. Deposition time of 30, and 360 s was found that produces the highest improvement for nanostructured and planar electrode, respectively.

5.3.2 Characterization

The surface morphology of the prepared films was examined by scanning electron microscopy, SEM (Carl Zeiss Auriga, Dual Column FIBSEM). Absorbance measurements were made using a Perkin-Elmer Lambda35 UV-vis spectrometer with a Labsphere integrating sphere. The absorbance spectra of the films were measured by illuminating from the substrate-electrode interface. The incident light was corrected for passing through and being reflected by the substrate using a previously reported approach.[19] Raman spectroscopy measurements were made using a Renishaw inVia instrument equipped with 532 nm laser operated at 5% of the source power (45 W). X-ray diffraction (XRD) patterns were obtained on a Bruker D8 Advanced diffractometer using Cu radiation with a Kα1 wavelength of 1.5418 Å.

5.3.3 Photoelectrochemical measurements

The electrodes were examined in contact with aqueous solutions of 1 M KOH electrolyte (pH=13.6). A homemade saturated Ag/AgCl electrode was used as a reference electrode and high surface area platinum mesh was used as the counter electrode. The reference electrode was regularly calibrated *vrsus* saturated calomel electrode (SCE) (Koslow Scientific) and all potentials were converted to the reversible hydrogen electrode (RHE) scale by the equation $V_{RHE} = V_{Ag/AgCl} + 0.197\ V + pH\ (0.059\ V)$. Photoelectrochemical measurements were made with an Eco Chemie Autolab potentiostat coupled with Nova electrochemical software. The light source was a 450 W Xe arc lamp (Horiba Jobin Yvon). An AM 1.5 solar filter was used to simulate sunlight at 100 mW cm^{-2} (1 sun). Unless otherwise mentioned, all photoelectrochemical tests were carried out by shining light on the electrodes through the electrolyte side (front side illumination) in a

custom-made electrochemical cell. All steady state and chopped light *J-V* curves were measured at a rate of 20 mV/s. A computer controlled ThorLabs solenoid shutter was used for the chopped light measurements. EIS data were collected using a 10 mV amplitude perturbation of between 10 kHz–10 mHz. Data were fitted using Zview software (Scribner Associates).

5.4 Results and discussion

SEM micrographs of planar (a-ED) and nanostructured (n-ED) electrodeposited electrodes are shown in Figure 5-1. As it can be seen the a-ED produced uniformly coated planar film which converts to a compact film upon annealing. n-ED on the other hand produces a sheet-like nanostructured FeOOH texture. The cause of the pH-dependent morphology of FeOOH electrodeposition can be found elsewhere.[24,26,27] As seen in the bottom panel, the morphology of the nanostructured films undergo significant changes in the feature size after annealing. Shown also in Figure 5-1 are the SEM micrographs of ALD hematite films. As expected from the conformal growth mechanism of ALD, the film general topography is very similar to the FTO substrate.[19]

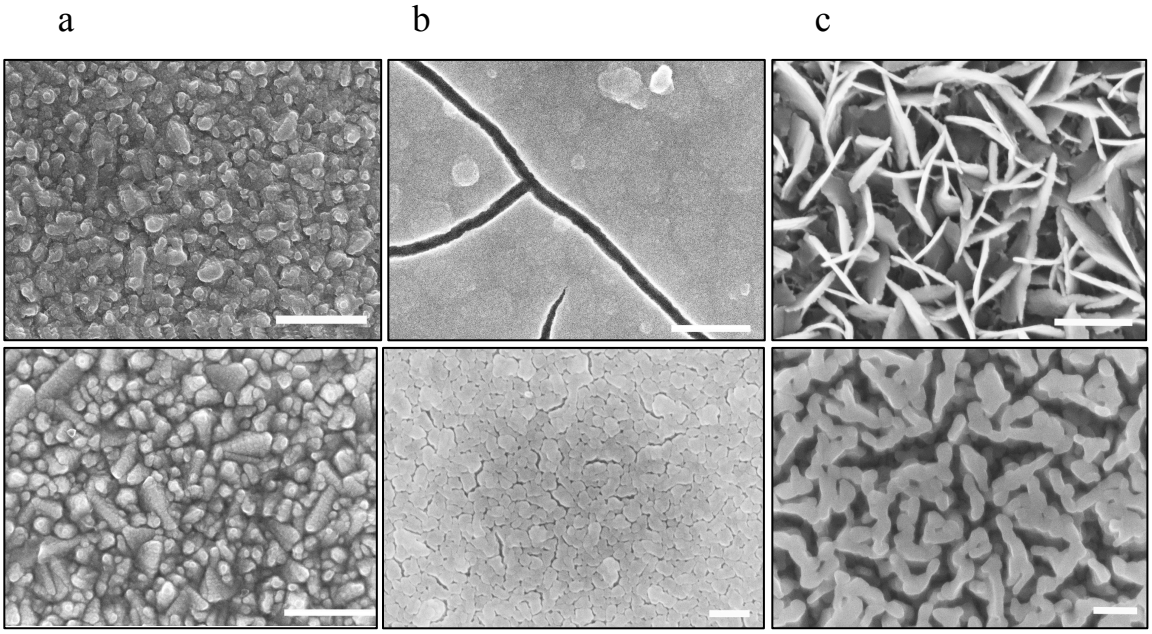

Figure 5-1. SEM images of as-deposited (top panel) and annealed (bottom panel) hematite electrodes prepared via a) ALD b) a-ED and c) n-ED. Scale bars are 400 nm.

In order to test the PEC activity of the electrodeposited films, current-potential (*J-V*) measurements were performed of the electrodes annealed at 500 and 800 °C. Surprisingly, electrodeposited films annealed at 500 °C produced little to no photocurrent, irrespective of the film morphology (Figure A5-3). This is often observed for solution processed hematite electrodes annealed below 500 °C which is attributed to low crystallinity and poor solid-solid contact at the FTO-hematite interface (Figure A5-2).[17,28,29] Annealing at 800 °C for 10 min resulted in dramatic improvement in the water oxidation performance. Electrodeposited hematite electrodes showed significantly better water oxidation performance compared to ALD films both annealed at 800 °C (Figure 5-1). The planar electrodeposited film in particular showed comparable photocurrent to the nanostructured electrodes, producing ~1 mA cm^{-2} at 1.23 V (Figure 1b), the highest reported value for a planar films to the best of

our knowledge. The high photoactivity along with the simplicity and scalability of the a-ED thus make it a promising approach to deposite high performance hematite thin films on transparent conductive substrates with variable morphologies.

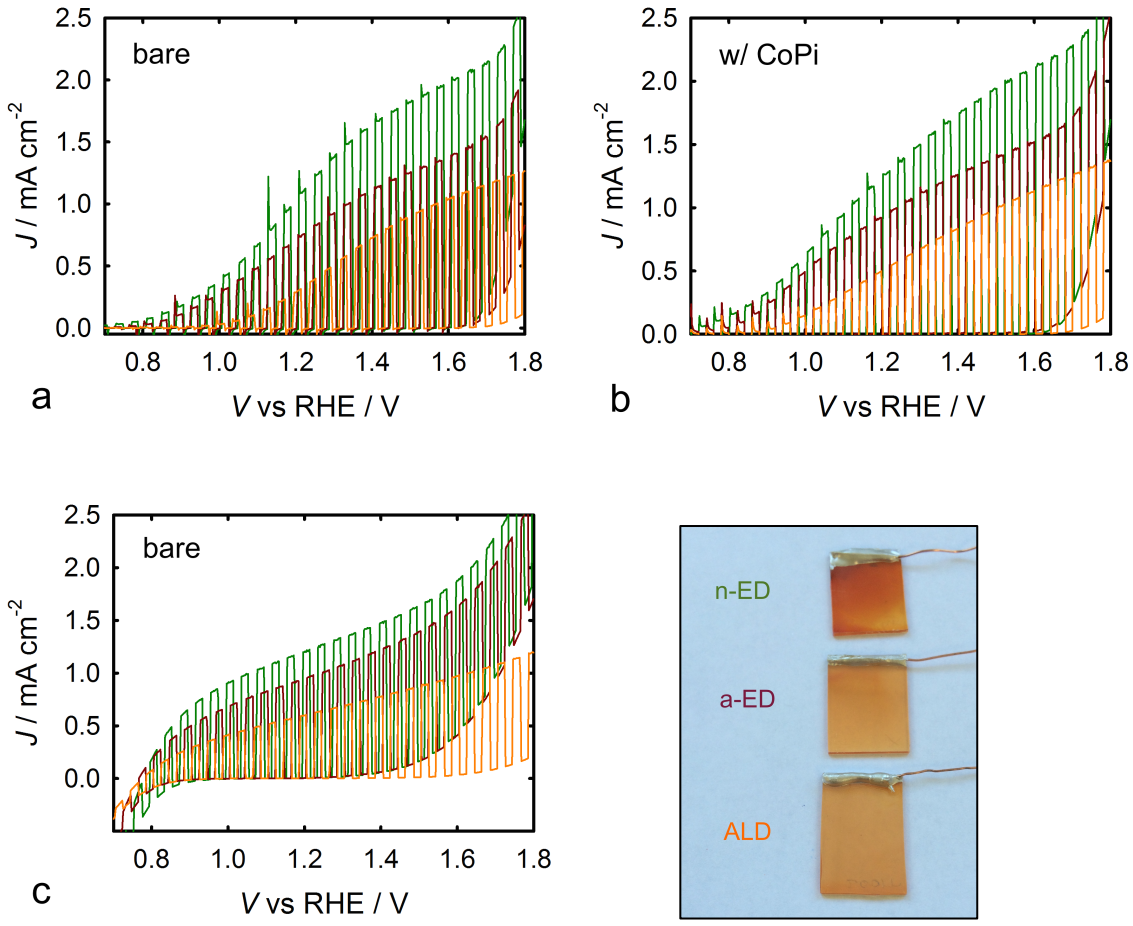

Figure 5-2. Chopped light *J-V* curves of hematite electrode prepared *via* ALD (orange) and ED of planar (dark red) and nanostructured (green) morphology in contact with 1 M KOH (a and b) and 0.5 M H_2O_2 (c). Shown also is a photograph of the electrodes produced the *J-V* responses.

J-V curves were also measured in the presence of H_2O_2 as a hole scavenger (Figure 5-1c). Higher photocurrent observed at low applied potentials in all cases compared to H_2O

oxidation. Assuming unity hole collection with the hole scavenger, the discrepancy in the *J-V* curves under H_2O and H_2O_2 oxidation can be attributed to surface recombination. This effect is more prominent for ALD films as seen from its positive water oxidation onset potential (Figure A5-4). Electrodes were then further modified with the Co-Pi water oxidation catalyst which is known to enhance surface hole collection. Co-Pi modification produced ~100-150 mV cathodic shift in the current onset potential and an overall increase in the photocurrent at low applied potentials (Figure 5-2b) consistent with previous reports.[8,9,12] From the comparison of the *J-V* curves after Co-Pi modification with that of the hole scavenger, electrodeposited electrodes showed near unity hole collection while the ALD film suffers from an additional 200 mV positive onset. In addition to a better photocurrent onset, higher photocurrent was measured for the a-ED film ((~0.95 mA cm^{-2} at 1.23 V) compared to the ALD electrode (~0.5 mA cm^{-2} at 1.23 V) in contact with the hole scavenger. This indicates a higher flux of holes reaching the electrode surface, i.e. better charge separation for ED film given that the light harvesting efficiency of these electrodes were comparable (see Figure A5-5).

Overall, the PEC data clearly indicates a promising performance for electrodeposited hematite electrodes, producing the water oxidation comparable or better than the ALD made counterparts. The somewhat higher photocurrent of the n-ED electrode compared to planar electrodes can partially be attributed to the three-dimensional structure placing a large fraction of the bulk within the hole collection length. The feature size in the nanostructured hematite plays the key role in charge separation and it is proven difficult to control under high annealing temperatures employed.[2,28] The planar electrodeposited electrodes however, outperformed the ALD films of comparable thickness and light absorption. This would

provide a promising alternative approach to deposit high performance hematite on nanostructured TCO substrates given the simplicity and conformal growth of a-ED. Further experiments were therefore conducted to elucidate the fundamental mechanism producing such enhanced water oxidation performance of electrodeposited electrodes compared to control samples deposited by ALD.

The structural properties of hematite films were characterized by X-ray diffraction (XRD) and Raman spectroscopy. Plots of XRD and Raman spectra are shown in Figure 5-3. In the XRD pattern of the electrodeposited hematite annealed at 800 °C several diffraction peaks were observed along [110], [104], [300], [012], [024] directions. For the ALD hematite film only two peaks were resolved corresponding to [104] and [110] diffractions with significantly weaker intensities. Given that the thicknesses of ALD and a-ED planar films are comparable, significantly shaper peaks in the XRD spectrum of the electrodeposited film indicates increased crystallinity. Further, a more intense peak along [110] plane indicates preferential orientation along this plane direction in the electrodeposited films. Higher crystallinity of the ED films compared to ALD made can be explained in term of the deposition conditions. ED resulted in amorphous FeOOH (Figure A5-2) film which is converted to crystalline α-Fe_2O_3 through annealing at elevated temperature.[24] Amorphous nature of the films allows Fe atoms to diffuse easily during annealing and form large crystallite size. For the ALD made films, however, the as-deposited films are already crystalline and annealing at 800 °C results in negligible effects on the diffraction peaks, consistent with the *J-V* responses. Therefore, as far as crystallinity is concerned, there are obvious differences which are explained as follows. First, higher crystallinity in general can result in an enhanced hole mobility, longer lifetimes, and thus

enhanced charge separation. The crystallite sizes were calculated from the [110] diffraction peak suing Scherrer's equation[30] to be 27 and 43 nm for ALD and ED films, respectively (~200 nm thick ALD film was used for crystallite calculation as the film discussed herein showed a very weak diffraction peak). Larger crystallites is associated with reduced density of grain boundaries which are known to reduce hole mobility.[21,31] Grain boundaries strongly affect the hole mobility considering that hole transport is happening *via* small polaron hopping, i.e. the distances and type of the neighboring atoms could strongly modify hole conductivity.[31] *J-V* measurements in hole scavenger suggested that the flux of hole reaching the electrode surface is higher for the planar ED electrodes. We therefore attribute part of the improvement to enhanced charge separation in the bulk, resulting from enhanced hole conductivity in the electrodeposited samples.

Further, higher crystallinity would produce a less defective surface, i.e. reduced density of surface trap states, resulting in less prominent surface recombination. This is consistent with the early water oxidation photocurrent onset measured for ED electrodes compared to ALD films (Figure 5-2). Part of the enhancement in water oxidation performance of the electrodeposited electrodes therefore can be attributed to a more efficient hole collection on the surface, i.e. suppressed surface recombination.

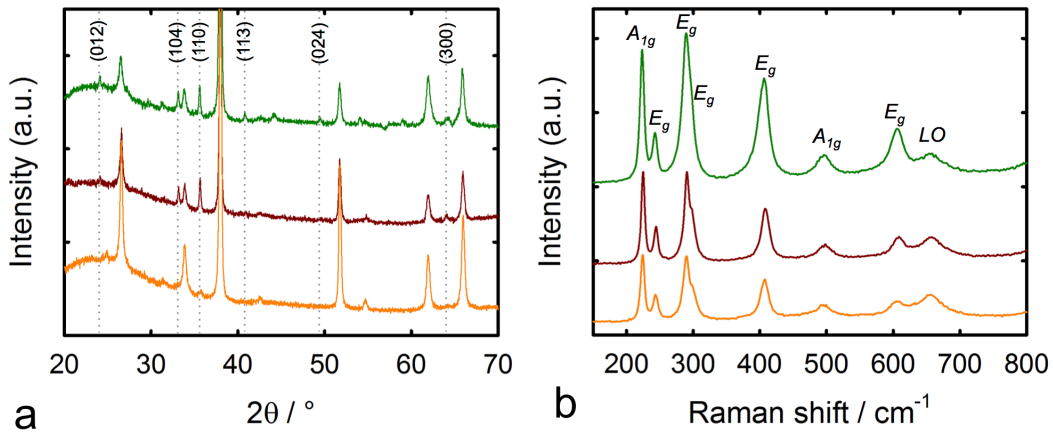

Figure 5-3. (a) XRD and (b) the Raman spectra of hematite electrode prepared via ALD (orange), a-ED (dark red) and n-ED (green) annealed at 800 °C.

Possible modification of the band edge energy and electronic properties, resulting from different preparation routes, were investigated by performing electrochemical impedance spectroscopy (EIS) measurements. Mott-Shottky plots of planar ED and ALD films are shown in Figure 5-4. The flat band potential is identical which is consistent with the onset of the hole scavenger *J-V* (Figure 5-2). Dopant densities were calculated using Mott-Schottky equation[32] and a dielectric constant of 32 for hematite.[19,33,34] The carrier concentration of ED films was nearly one order of magnitude higher than that of the ALD film (1.1×10^{21} cm^{-3} and 2×10^{20} cm^{-3} for ED and ALD film, respectively). This increased carrier concentration can potentially enhance charge separation at the interface through inducing a sharper band-bending at the interface. Sharper band bending and associated high drift potential thus can enhance hole transit time in the depletion region, which reduces depletion region and surface recombination as discussed in the previous chapter. We note that the dopant density of the ALD film is somewhat higher than the value previous reported for hematite films

prepared by ALD.[19] This can be a consequence of higher annealing temperature which can enhance he oxygen vacancy Sn diffusion-doping into the hematite film.[35]

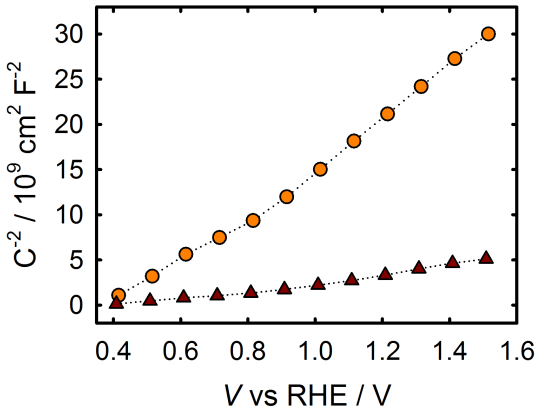

Figure 5-4. Mott-Shottky plots of planar hematite electrode prepared by ALD (orange circles) and a-ED (dark red triangles) measured in dark. EIS data fitted using the Randal circuit shown in the appendix.

J-V responses presented above indicate enhanced charge separation and surface hole collection which correlate with increased crystallinity and carrier concentration. In order to further validate this assignment and get a better insight into the dynamics of charge carriers in the bulk and on the electrode surface, EIS measurements were also carried out under 1 Sun illumination. The impedance data were fit to a circuit model previously established for hematite-electrolyte interface under illumination (see the appendix).[36] The equivalent circuit model contained a chemical capacitance due to hole build-up on the surface, surface state capacitance (C_{ss}), in addition hematite space charge capacitance (C_{bulk}). The model also includes a resistance due to hole trapping in the surface states, R_{trap}, and hole transfer on the surface, R_{ct} (i.e. charge transfer resistance). Plots of these parameters are shown in Figure 5-

5 versus applied potential for planar ED and ALD electrodes. C_{bulk} is higher for ED electrode consistent with higher dopant density measured also in the Mott-Schottky analysis in dark. The striking differences were in the charge transport resistances, however. As seen in Figure 5-5b the R_{trap} was nearly three orders of magnitude lower for ED hematite electrode. This is consistent with increased number of holes being trapped at the surface states at a given applied potential compared to the ALD electrode. This is also is consistent with an enhanced hole conductivity in line with crystallinity dependent hole transport discussed earlier. As seen in Figure 5-5c, more than one order lower charger transfer resistance was also observed for the ED electrode around the photocurrent onset potential, which again is consistent with the early water oxidation onset in the *J-V* response. This also is in line with a higher surface hole collection efficiency resulting form reduced surface recombination rate.

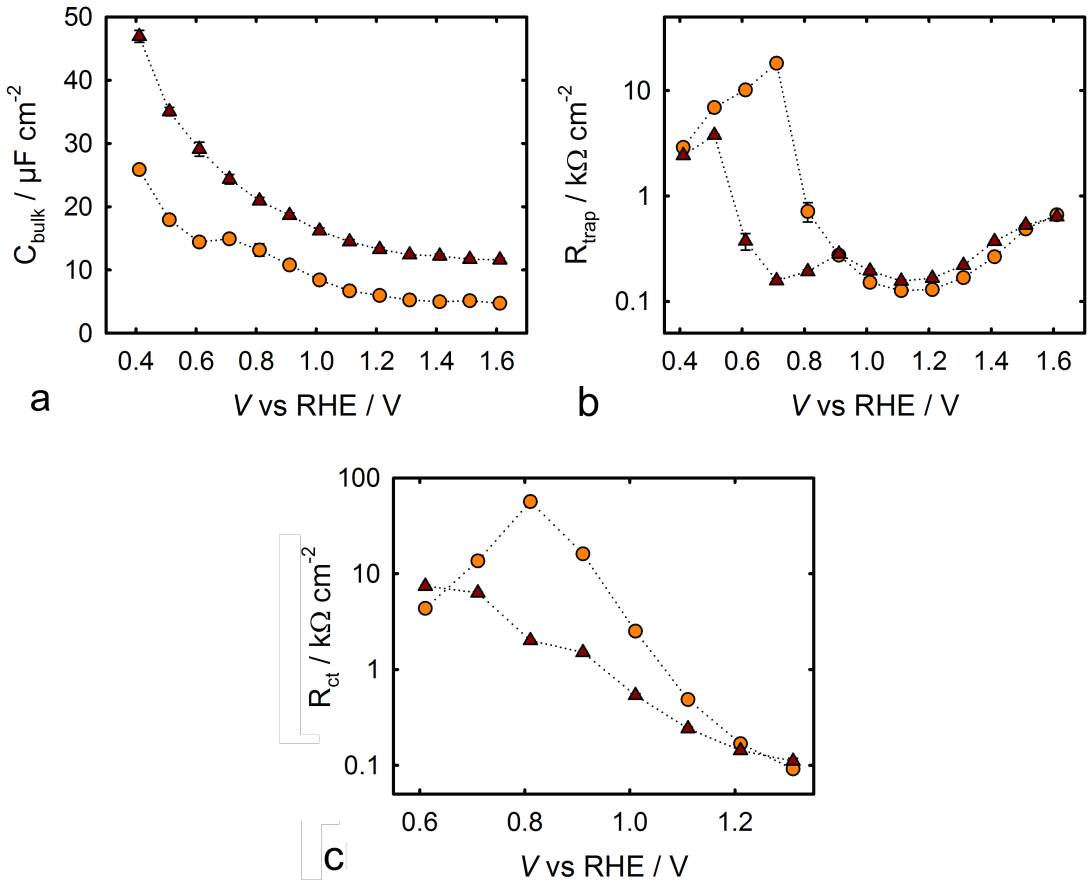

Figure 5-5. Impedance parameters extracted form the fit of the EIS data measured under PEC water oxidation for planar ED (dark red triangles) and ALD (orange circles) hematite thin film electrodes.

All together, the PEC, structural and EIS data support an enhanced charge separation and collection efficiency for planar ED electrode when compared to the electrodes of identical light absorption prepared by ALD. The different in performance is attributed to the structural attributes resulting from differences in preparation condition. Electrodeposition results in uniform films of amorphous FeOOH, which converts to highly crystalline α-Fe_2O_3 after annealing. Improved bulk and surface properties (confirmed by EIS measurements)

result in higher photocurrent and early photocurrent onset as observed in the *J-V* responses. We showed in chapter 2 that crystallinity is an important factor in determining the water oxidation performance of hematite electrodes. Warren *et al.* also demonstrated higher charge separation for electrodes with reduced grain boundaries.[21] In addition to a better crystallinity, electrodeposited electrodes showed one order higher carrier concentration. Higher carrier concentration in turn produces sharper band bending as potential drops across a thinner width (chapter 4). This would enhance the hole drift velocity which reduces depletion region recombination as suggested by others.[37] Sharper band bending also results in a more efficient electron extraction thus reducing surface recombination. These are all in good agreement with the higher photocurrent and better photocurrent onset measured in the *J-V* responses.

One significant consequence of higher carrier concentration however, is the substantial reduction of the depletion width, *W*. Using equation 5-1, depletion region was calculated for ED and ALD films using the calculated dopant densities. At 1.23 V *vs*. RHE the built-in potential is 0.623 V (i.e. *vs.* E_{fb}=0.6 V) for both films assuming no surface Fermi level pining for electrodes in contact with hole scavenger.

$$W=\left(\frac{2\kappa\varepsilon_0 V_{bi}}{qN_d}\right)^{1/2} \qquad (5\text{-}1)$$

Where κ is hematite's dielectric constant (32) and ε_0 is the vacuum permittivity, and N_d is dopant density. Depletion width was then calculated to be 1.41 and 3.66 nm for ED and ALD films, respectively. A very small depletion width, especially in the case of ED film, results from a high dopant density as expected from equation 5-1. Therefore, although a higher dopant result in the sharper band bending which could facilitate charge separation, it

also reduces the depletion layer significantly so that the number of the carrier generated inside of this layer would be significantly lower. In order to obtain a more quantitative measure of this effect, absorptance of the depletion width (i.e. the light harvesting efficiency of the depletion layer for each electrode) was calculated using the absorptivity of hematite films, assuming no reflection losses.[23] The absorptance of depletion widths is shown in Figure 5-6a for 1.41 and 3.66 nm of hematite, corresponding of the *W* of ED and ALD films, respectively. Absorbed photons to current conversion efficiency (APCE) in the depletion layer was then calculated using the incident photons to current conversion efficiency (IPCE) measured at 1.23 V (see the appendix) and the calculated absorptances of *W*. Assuming zero hole diffusion length, quantitative charge collection in the depletion layer should produce a 100% APCE at all wavelengths. As seen in Figure 5-6b, the APCE of the ALD film depletion width reached a maximum of ~30%. This indicates a hole diffusion length of zero and that there is significant depletion region recombination. Strikingly different behavior was observed in the APCE of ED film however, with over 100% values for photons > 450 nm. This indicates that not only the APCE of depletion width is 100% but also there is a nonzero diffusion length of hole outside of the depletion region which contribute to the IPCE. Quantitative hole collection in the depletion region is not surprising given that the thickness is only 1.41 nm. Over 100% APCE however, implies an important conclusion; there in fact nonzero hole diffusion length for photons shorter than 450 nm which is contrast to the our measurement on ALD films.[19,23] This can be attributed to an enhanced hole mobility and/or life time in the bulk resulting form the high crystallinity of the ED film further highlighting the importance of crystallinity in determining the charge separation in hematite. An optimized hematite thickness in this case is thus the *depletion*

width + one hole diffusion length, i.e. ~ 3 nm. Fabricating such a thin high quality electrode is a challenging task, which requires a high level material engineering. A very high dopant density thus is not necessarily beneficial as it reduces the depletion width significantly. Alternatively, one can think of controlling the dopant density low enough to have a larger depletion layer at the same time depositing highly crystalline films. This strategy would effectively utilize the drift + diffusing length to harvest a larger fraction of photons that can generate significantly higher photocurrent. Determination of dopant densities effect is a subject of current investigation in our Lab. Further, Figure 5b indicates zero diffusion length for holes resulted form the absorption of green photons (< 450 nm). This photon energy dependent APCE which is general to hematite electrodes,[19,38] is a major loss in photocurrent as it covers a spectral region where the solar spectrum is most intense.

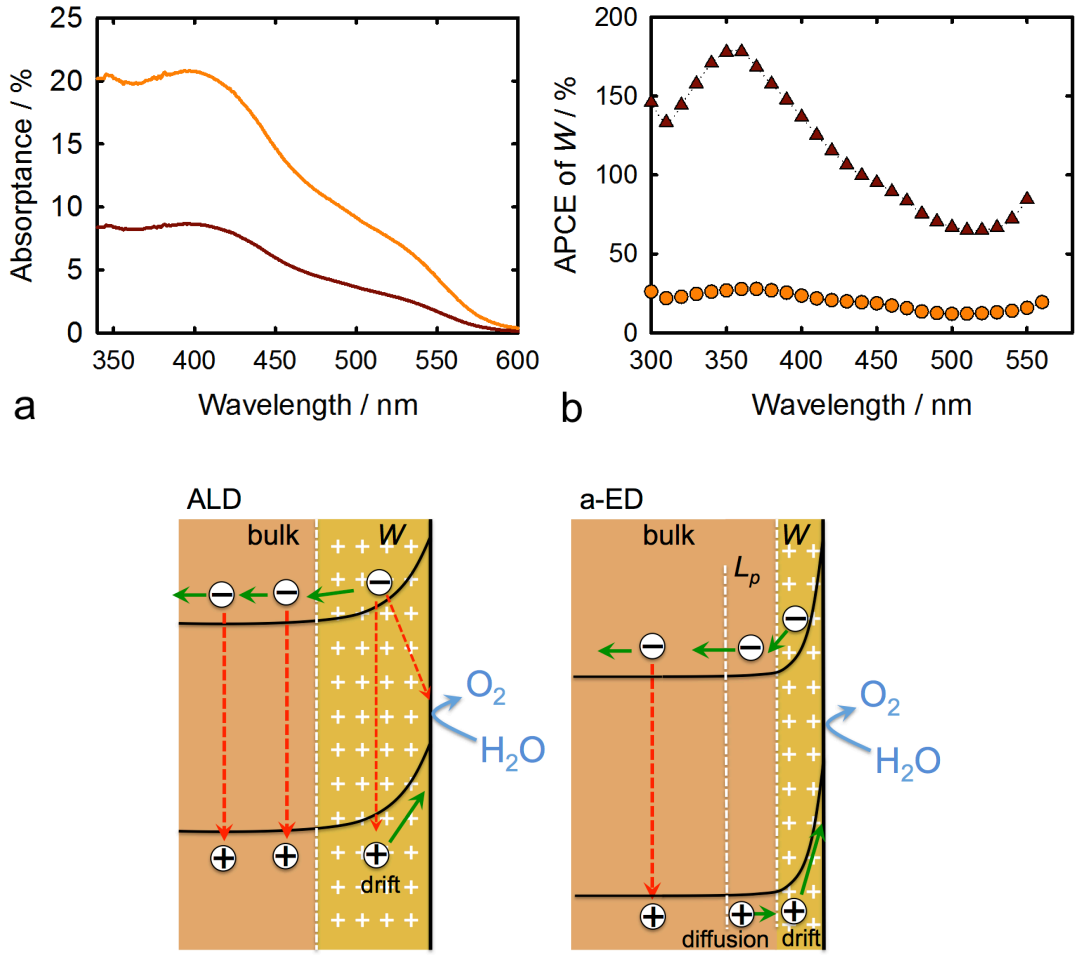

Figure 5-6. a) Calculated absorptance of the depletion width for ED (dark red) and ALD (orange) thin films. b) APCE of the depletion width calculated from the IPCE data measured under 1 Sun illumination at 1.23 V vs. RHE. Schematic band bending diagram and charge transfer processes is also shown for ALD and ED films.

Another possible factor that could produce enhanced charge transport and surface hole collection is preferential crystallographic orientation along [110] plane in hematite. [110] preferred orientation not only provides a higher conductivity for charge carrier transport in the bulk, but also exposes the most catalytically active Fe terminated surfaces.[39–41] This behavior was recently observed by others for hematite electrodes with [110] preferential

orientation.[17,39,40] From the XRD data it can be seen that all samples show a more intense diffraction peak along [110]. However, as the diffraction peak of the ALD film was significantly weaker that the ED films, it is difficult to unambiguously determine the potential beneficial effect of preferred crystallographic orientations in the samples discussed herein. Nonetheless, this effect along with higher crystallinity can further enhance charge transport and collection, which requires further studies so that it can be fully exploited.

5.5 Conclusion

In summary, high performance hematite electrodes of variable morphology were prepared via a simple electrodeposition method. The water oxidation performance of planar thin films in particular were significantly higher than the state of the art planar hematite electrodes reported to date. The better performance was attributed to enhanced charge separation and surface hole collection resulting form a highly crystalline hematite that can be fabricated *via* electrodeposition. In addition, these finding provides a more clear insight on the charge collection length in hematite electrodes of two preparation routes which can be exploited to fabricated efficient photoanode systems.

APPENDIX

Figure A5-1. Photograph of as-deposited (left) and annealed (right) films prepared *via* a-ED (deposition time of 60 min).

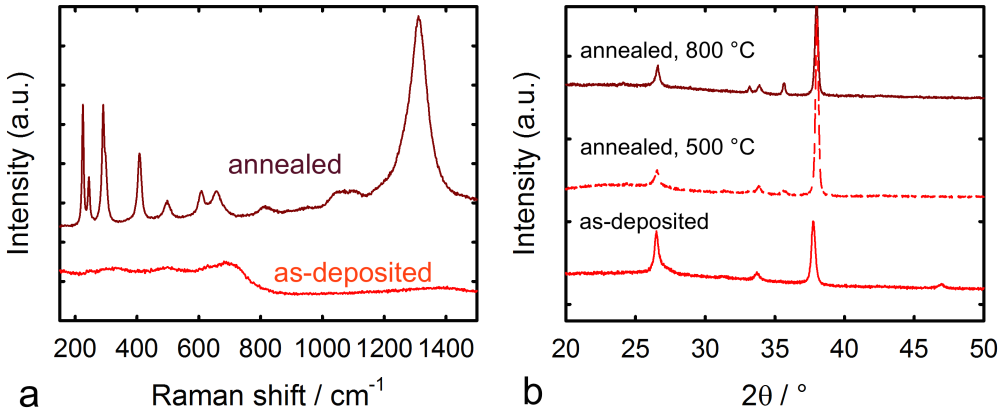

Figure A5-2. Raman (a) and XRD (b) spectra of as-deposited and annealed ED films.

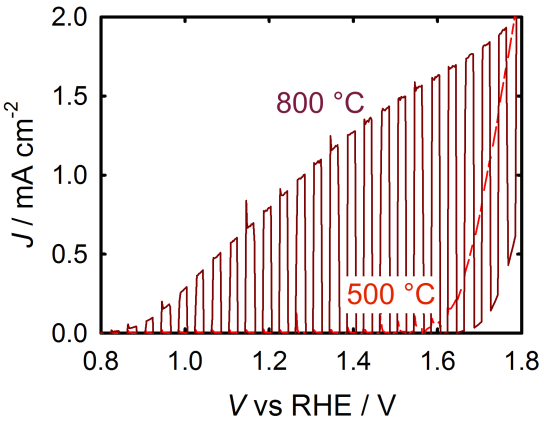

Figure A5-3. *J-V* curves of a-ED hematite electrodes annealed at 500 and 800 °C.

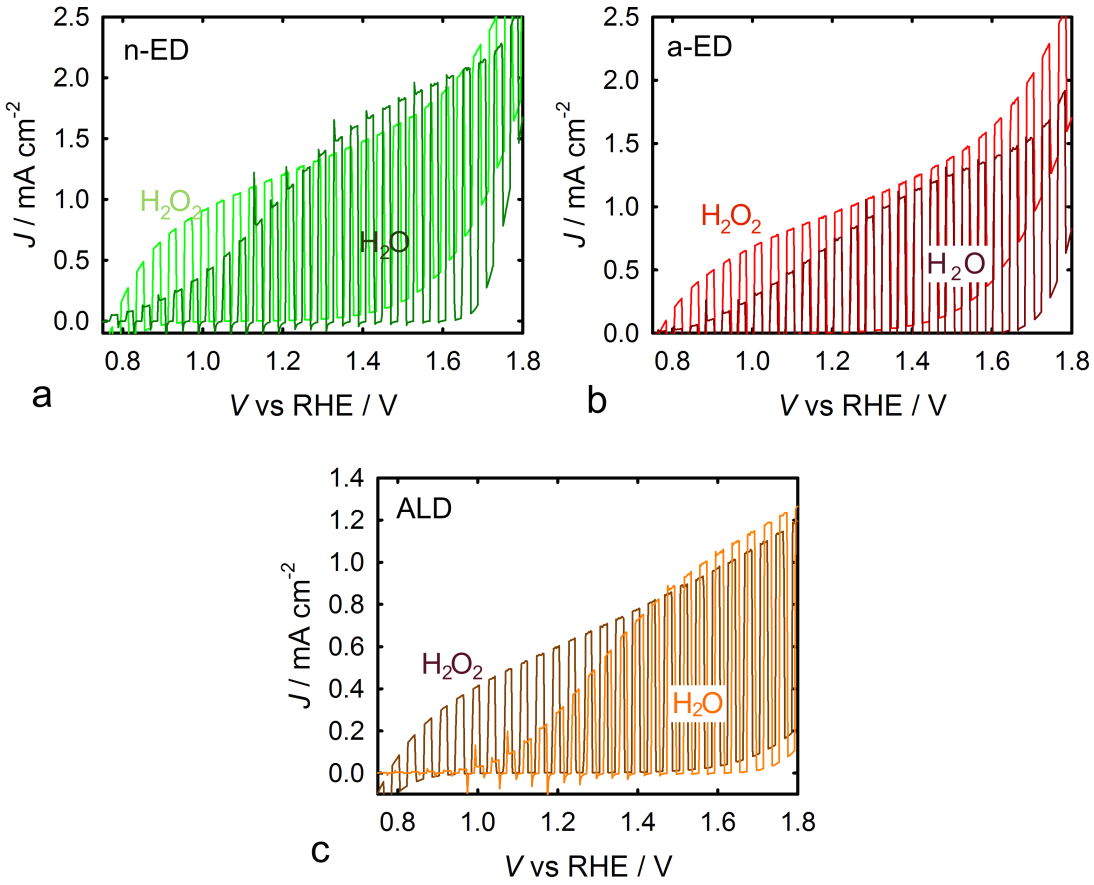

Figure A5-4. *J-V* curves of hematite electrode in contact with 1M KOH (soli curves) and added 0.5 M H2O2 (dotted curves).

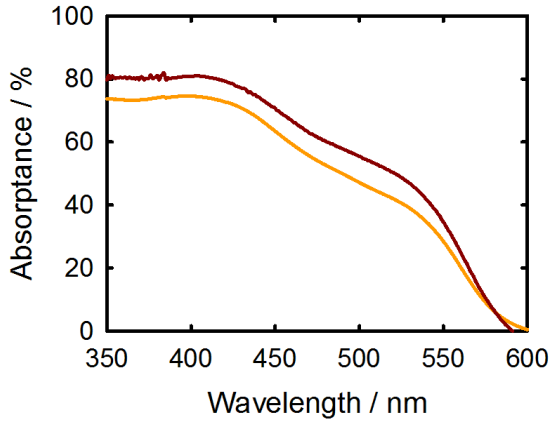

Figure A5-5. Absorptance profile of hematite thin films prepared via ALD (orange) and a-ED (dark red) of the same thickness.

Fitting EIS data: EIS data were fitted using the equivalent circuit models shown below. The justification and physical meaning of using the model in Figure A5-6a (used to fit the light EIS data) is descried elsewhere.[19] This model, which was established for ALD thin films, was found that produces a comparable certainty for the a-ED films. In both cases a very small error associated with fitting was calculated which is included as error bars in the graphs shown in the main text.

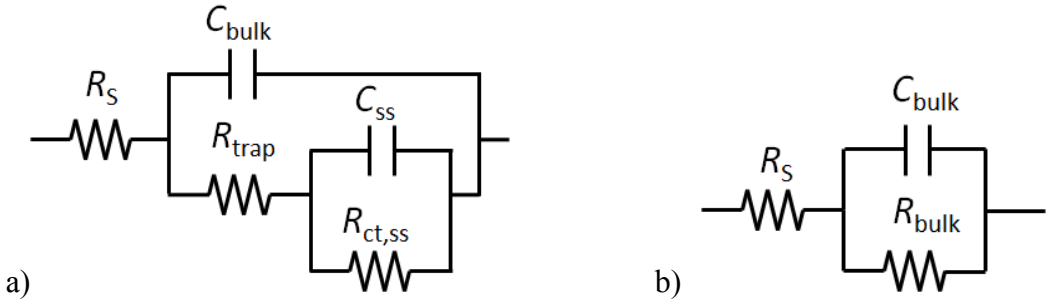

Figure A5-6. Equivalent circuits used to fit the experimental EIS data under illumination (a) and in dark (b).

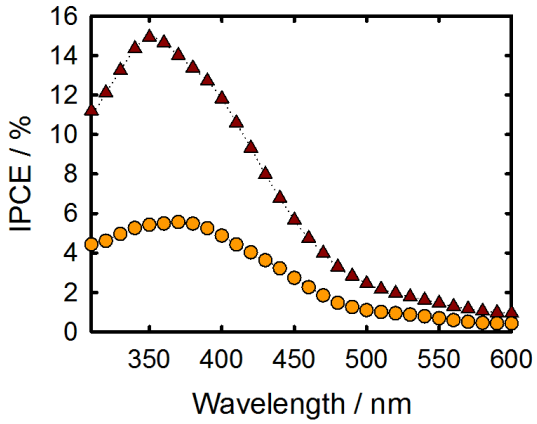

Figure A5-7. IPCE of ED (dark red triangles) and ALD (orange circles) hematite thin film electrodes modified with Co-Pi.

REFERENCES

REFERENCES

(1) Kay, A.; Cesar, I.; Grätzel, M. *J. Am. Chem. Soc.* **2006**, 15714.

(2) Brillet, J.; Grätzel, M.; Sivula, K. *Nano Lett.* **2010**, *10*, 4155.

(3) Beermann, N.; Vayssieres, L.; Lindquist, S.-E.; Hagfeldt, A. *J. Electrochem. Soc.* **2000**, *147*, 2456.

(4) Riha, S. C.; Devries Vermeer, M. J.; Pellin, M. J.; Hupp, J. T.; Martinson, A. B. F. *ACS Appl. Mater. Interfaces* **2013**, *5*, 360.

(5) Lin, Y.; Zhou, S.; Sheehan, S. W.; Wang, D. *J. Am. Chem. Soc.* **2011**, *133*, 2398.

(6) Stefik, M.; Cornuz, M.; Mathews, N.; Hisatomi, T.; Mhaisalkar, S.; Grätzel, M. *Nano Lett.* **2012**, *12*, 5431.

(7) Tilley, S. D.; Cornuz, M.; Sivula, K.; Grätzel, M. *Angew. Chemie* **2010**, *122*, 6549.

(8) Klahr, B.; Gimenez, S.; Fabregat-Santiago, F.; Bisquert, J.; Hamann, T. W. *J. Am. Chem. Soc.* **2012**, *134*, 16693.

(9) Zhong, D. K.; Cornuz, M.; Sivula, K.; Grätzel, M.; Gamelin, D. R. *Energy Environ. Sci.* **2011**, *4*, 1759.

(10) Du, C.; Yang, X.; Mayer, M. T.; Hoyt, H.; Xie, J.; McMahon, G.; Bischoping, G.; Wang, D. *Angew. Chem. Int. Ed. Engl.* **2013**, *52*, 12692.

(11) Le Formal, F.; Tétreault, N.; Cornuz, M.; Moehl, T.; Grätzel, M.; Sivula, K. *Chem. Sci.* **2011**, *2*, 737.

(12) Kim, J. Y.; Magesh, G.; Youn, D. H.; Jang, J.-W.; Kubota, J.; Domen, K.; Lee, J. S. *Sci. Rep.* **2013**, *3*, 1.

(13) Upul Wijayantha, K. G.; Saremi-Yarahmadi, S.; Peter, L. M. *Phys. Chem. Chem. Phys.* **2011**, *13*, 5264.

(14) Dotan, H.; Sivula, K.; Grätzel, M.; Rothschild, A.; Warren, S. C. *Energy Environ. Sci.* **2011**, *4*, 958.

(15) Klahr, B.; Gimenez, S.; Fabregat-Santiago, F.; Bisquert, J.; Hamann, T. W. *Energy Environ. Sci.* **2012**, *5*, 7626.

(16) Zandi, O.; Hamann, T. *J. Phys. Chem. Lett.* **2014**, *5*, 1522.

(17) Jang, J.-W.; Du, C.; Ye, Y.; Lin, Y.; Yao, X.; Thorne, J.; Liu, E.; McMahon, G.; Zhu, J.; Javey, A.; Guo, J.; Wang, D. *Nat. Commun.* **2015**, *6*, DOI: 10.1038/ncomms8447.

(18) Walter, M. G.; Warren, E. L.; Mckone, J. R.; Boettcher, S. W.; Mi, Q.; Santori, E. A.; Lewis, N. S. *Chem. Rev.* **2010**, *110*, 6446.

(19) Klahr, B. M.; Martinson, A. B. F.; Hamann, T. W. *Langmuir* **2011**, *27*, 461.

(20) Klahr, B. M.; Hamann, T. W. *Appl. Phys. Lett.* **2011**, *99*, 063508 1.

(21) Warren, S. C.; Voïtchovsky, K.; Dotan, H.; Leroy, C. M.; Cornuz, M.; Stellacci, F.; Hébert, C.; Rothschild, A.; Grätzel, M. *Nat. Mater.* **2013**, *12*, 842.

(22) Warren, S. C. In *Photoelectrochemical Hydrogen Production*; 2012; pp. 293–316.

(23) Zandi, O.; Hamann, T. *Phys. Chem. Chem. Phys.* **2015**, DOI: 10.1039/C5CP04267D.

(24) Spray, R. L.; Choi, K. S. *Chem. Mater.* **2009**, *21*, 3701.

(25) Zhong, D. K.; Gamelin, D. R. *J. Am. Chem. Soc.* **2010**, *132*, 4202.

(26) Jiao, S.; Xu, L.; Hu, K.; Li, J.; Gao, S.; Xu, D. **2010**, *114*, 269.

(27) Markovac, V.; Cohen, M. *J. Electrochem. Soc.* **1972**, *119*, 987.

(28) Sivula, K.; Zboril, R.; Le Formal, F.; Robert, R.; Weidenkaff, A.; Tucek, J.; Frydrych, J.; Grätzel, M. *J. Am. Chem. Soc.* **2010**, *132*, 7436.

(29) Goncalves, R. H.; Leite, E. R. *J. Mater. Res.* **2013**, *29*, 47.

(30) Patterson, A. L. *Phys. Rev.* **1939**, *56*, 978.

(31) Bosman, a. J.; van Daal, H. J. *Adv. Phys.* **1970**, *19*, 1.

(32) Gelderman, K.; Lee, L.; Donne, S. W. *J. Chem. Educ.* **2007**, *84*, 685.

(33) Zandi, O.; Klahr, B.; Hamann, T. *Energy Environ. Sci.* **2013**, *6*, 634.

(34) Glasscock, J. A.; Barnes, P. R. F.; Plumb, I. C.; Bendavid, A.; Martin, P. J. **2008**, *516*, 1716.

(35) Sivula, K.; Zboril, R.; Le Formal, F.; Robert, R.; Weidenkaff, A.; Tucek, J.; Frydrych, J.; Grätzel, M. *J. Am. Chem. Soc.* **2010**, *132*, 7436.

(36) Klahr, B.; Gimenez, S.; Fabregat-Santiago, F.; Hamann, T.; Bisquert, J. *J. Am. Chem. Soc.* **2012**, *134*, 4294.

(37) Jarrett, H. S. *J. Appl. Phys.* **1981**, *52*, 4681.

(38) Kim, D. W.; Riha, S. C.; Demarco, E. J.; Martinson, A. B. F.; Farha, O. K.; Hupp, J. T. *ACS Nano* **2014**, *8*, 12199.

(39) Peter, L. M.; Upul Wijayantha, K. G. *ChemPhysChem* **2014**, *15*, 1983.

(40) Kment, S.; Schmuki, P.; Hubicka, Z.; Machala, L.; Kirchgeorg, R.; Liu, N.; Wang, L.; Lee, K.; Olejnicek, J.; Cada, M.; Gregora, I.; Zboril, R. *ACS Nano* **2015**, DOI: 10.1021/acsnano.5b01740.

(41) Cornuz, M.; Grätzel, M.; Sivula, K. *Chem. Vap. Depos.* **2010**, *16*, 291.

Chapter 6:

In-Situ Determination of Photoelectrochemical Water Oxidation Intermediates on Hematite Electrodes

6.1 Abstract

The surface of hematite electrodes were probed by *in-situ* ATR-IR spectroscopy under photoelectrochemical (PEC) water oxidation. Potential and light-dependent IR absorption peaks were reproducibly resolved at 744 and 896 cm^{-1} which can be clearly correlated to the current-potential curves. These absorption peaks can be assigned to Fe^{IV}=O and FeO–OH groups forming during PEC water oxidation reaction. Control experiments in contact with a hole scavenger and isotope labeled water further corroborated the assignment of these spectral features to oxygen containing groups involved in the water oxidation reaction. These results thus establishes the mechanism of PEC water oxidation on hematite by providing the first direct evidence of high-valent iron-*oxo* intermediates as the product of the first hole transfer reaction on the surface.

6.2 Introduction

As discussed in the previous chapters, the hematite-electrolyte interface plays a key role in separating charge carriers and subsequent hole transfer to H_2O molecules. A clear understanding of the surface electrochemistry of hematite thus is crucial as it determines the extent of band bending (thus the extent of the space charge layer) as well as the efficiency of hole transfer to H_2O oxidation reaction. For example, surface electron-hole recombination, which is one of the major efficiency loss mechanisms (accounted for the loss of several hundred millivolts voltage) is a parasitic reaction in competition with forward hole transfer.

The hematite/electrolyte photoelectrochemistry has been studied in details by several groups. Surface recombination has been confirmed and often associated with a combination of sluggish kinetics of H_2O oxidation, Fermi-level pinning, and trap state-mediated recombination.[1–3] It is generally agreed upon that surface holes are competitively consumed by either recombination with conduction (and trapped) electrons or forward H_2O oxidation reaction. While this general scheme is widely agreed upon in the literature, the chemical identity of the surface holes and the mechanism of H_2O oxidation has remained controversial as there is no direct evidence as to the nature of the mechanism of four-hole H_2O oxidation reaction on hematite.[1] Peter and co-workers utilized electrochemical impedance spectroscopy (EIS) and intensity modulated photocurrent spectroscopy (IMPS) to study the kinetics of PEC water oxidation on hematite.[2,4] A kinetic model was developed based on the EIS and IMPS data which suggested surface hole accumulation in the form oxidized surface states. They further studied the nature of oxidized surface species by light and potential-modulated absorption spectroscopy.[5] An absorption feature was observed around 570 nm which was assigned Fe^{IV}=O, possible intermediates of oxygen evolution

reaction.[5] Barroso *et al.* observed identical spectral feature on hematite electrodes by spectroelectrochemistry under PEC water oxidation.[6] They however assigned this spectral feature to long-lived surface holes. Klahr *et al.* investigated the hematite-electrolyte interface employing photoelectrochemical and electrochemical impedance spectroscopy measurements.[7,8] A capacitive element was observed in the EIS measurements under illumination which was assigned to the accumulation of holes in surface states. A coincident drop in charge transfer resistance and an abrupt photocurrent onset with the peak of the surface states capacitance corroborated the assignment of surface hole accumulation to a key step in H_2O oxidation on hematite. Klahr *et al.* further demonstrated a decrease in surface state capacitance under competitive methanol and water oxidation which confirmed that the surface states are actively participating in H_2O oxidation process on the hematite surface.[9] The nature of surface accumulated hole was further studied *via* in-situ spectroelectrochemistry under PEC H_2O oxidation. A bias dependent spectral feature was observed at 572 nm identical to Peter and co-workers findings.[10] Quantitative correlation was found between the surface state capacitance and the magnitude of the absorption peak confirming that they are originating from the same effect. Further, the absorption cross section of the peak at 572 nm was calculated to be comparable with Fe^{IV}=O intermediates often observed in iron-based oxygen activating enzymes.[10] The first hole transfer reaction on the fully hydroxylated most stable surface[11] of hematite is therefore described by equation 6-1, which is agreement with first principle calculations.[12]

$$R - Fe^{III} - OH \underset{e^-}{\overset{h^+}{\rightleftharpoons}} R - Fe^{IV} = O + H^+ \qquad (6\text{-}1)$$

Where R represents the bulk hematite. This reaction is thus what in the literature is referred as hole trapping or charging/de-charging of surface states.[6,8,13] The reverse reaction is

essentially the surface recombination reaction which is a function of electron concentration near the surface.

While the previous reports generally support the formation of high-valent iron species on the hematite surface as the first step of PEC water oxidation reaction, none is providing a direct evidence of the chemical identity of such groups. Here we report a first direct evidence of oxidized surface states that are mediating PEC water oxidation on hematite electrodes through *in-situ* IR spectroscopy. This is to the best of our knowledge the first report on identification of H_2O oxidation intermediates on semiconductor electrodes under real working conditions. Probing the electrode surface in dark and under illumination and controlled potential condition allowed us to systematically examine the effect of light and applied potential on the surface chemistry of hematite electrodes. Potential and light-dependent IR spectra thus can be clearly correlated to the PEC measurements and draw mechanistic insight under real working conditions.

6.3 Experimental

6.3.1 Electrode preparation and *in-situ* setup

Hematite electrodes were prepared by atomic layer deposition of Fe_2O_3 following the method previously discussed in chapter 2. A total of 1000 ALD cycles Fe_2O_3 (equivalent of ~ 50 nm) were deposited on F:SnO_2–coated glass substrate (Hartford, 12-15 ohm cm) followed by annealing at 500 °C for 2 h. The electrodes were cut in 1.5×6 cm for the *in-situ* experiments. Electrical contact was made using silver epoxy conductive paste covered with an insulating epoxy finish. Two small holes in the hematite electrodes (contained a droplet of electrolyte) provided electrical connection between the working electrode (hematite

surface), the counter and the reference electrodes (Figure 6-1). For *in-situ* measurements, the hematite electrode was fixed against the IR element with ~ 50 µL electrolyte (0.1 M KCl in D_2O, pH=7.3). A Teflon bridge was used to press the hematite working electrode tightly in place (note that adhesion between two wet surfaces tightly holds the crystal and electrode together).

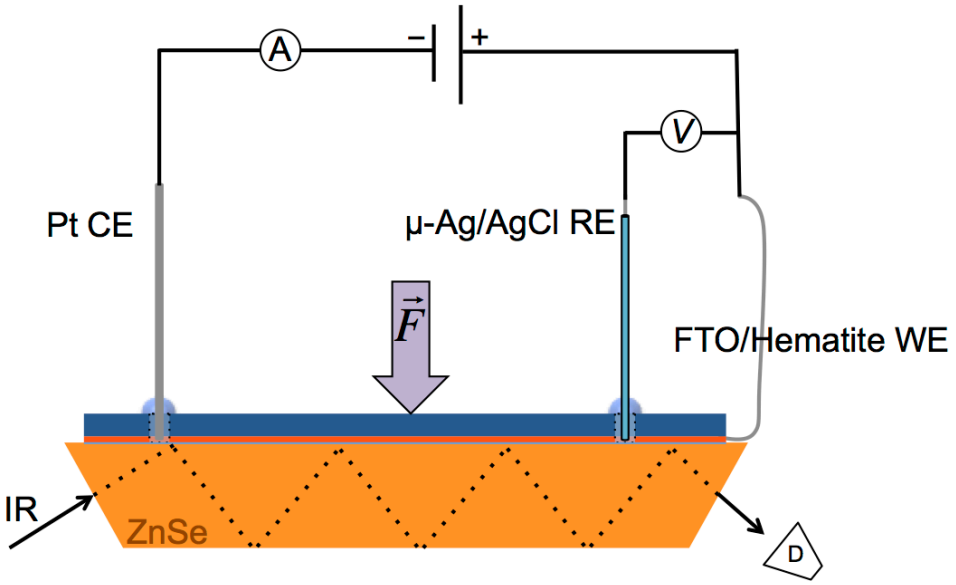

Figure 6-1. Schematic setup of the *in-situ* PEC-IR cell.

6.3.2 *In-situ* PEC-IR measurements

In-situ IR measurements were made using a Magna-IR 550 Spectrometer using a Gateway Flow Through Top-plate cell multi reflection ATR setup (Specac). A 45° angle ZnSe crystal was used (cut-off energy of ~ 625 cm^{-1}). For the in-situ measurement approximately 50 µL aqueous electrolyte was placed on the crystal and the hematite electrode was then pressed against the crystal using a home-built teflon bridge. Each IR absorption spectrum was acquired by averaging 200 scans at the resolution of 4 cm^{-1}. For *in-*

situ IR, spectral acquisition was carried out under constant applied potential to the hematite electrode. *In-situ* IR spectra were individually corrected for the background right before each measurement. A LED UV flashlight (395 nm) was used as the light source for the PEC experiments. The LED power at fixed distance from the electrode surface was estimated to be about 10 $mWcm^{-2}$ using a certified reference cell system (Newport).

In-situ electrochemical measurements were conducted using a micro-Autolab potentiostat using a "*no leak*" Ag/AgCl (Warner) micro-reference electrode and a Pt wire as the counter electrode. Unless otherwise mentioned all the *in-situ* experiments were performed in D_2O (99.9 atomic %, Aldrich) containing 0.2 M KCl (99.0 %, Aldirch). ^{18}O labeled D_2O (95% ^{18}O and 99% D, Medical Isotopes) was used for isotope exchange control experiments. All experiments were performed using as-prepared electrolyte solutions. Prior to the *in-situ* measurements, the electrodes, the crystal and the flow cell holder were dried in a drying oven for at least 2 hours.

6.4 Results and discussion

Before performing the *in-situ* measurements, hematite electrodes were characterized *ex-situ* under PEC water oxidation condition using a monochromatic 395 nm light (the light source used for the *in-situ* measurements). *J-V* curves in dark and under illumination conditions are shown in Figure 6-2a. The general trend of the *J-V* responses is in good agreement with the behavior under 1 sun illumination presented in the previous chapters. EIS measurement were also performed under PEC water oxidation conditions. Two capacitive elements (semicircle in the Nyquist plots) were observed at potentials around the photocurrent onset consistent with previous reports (Figure 6-2b).[8] These capacitive

processes correspond to the space charge capacitance and chemical capacitance due to the build-up of holes on the surface, i.e. surface states capacitance, C_{ss}.[8] The surface state capacitance at various applied potential was then extracted by fitting the EIS data to the equivalent circuit shown in the previous chapter (Appendix 5). As seen in Figure 6-2c, the C_{ss} exhibits a Gaussian peak around the photocurrent onset, which was attributed to the surface hole accumulation.[10] The charging and de-charging of this surface state was also measured by cyclic voltammetry (CV). Figure 6-1d shows the CV curves scanned to more negative potentials immediately after holding the electrode at positive potential under illumination and dark. At positive potential and under illumination holes get trapped in the surface states, i.e. oxidation of surface states. Scanning negatively in the dark reduces these states, resulting in a negative peak in current at their specific energy. The extent and distribution of the cathodic peak is in good agreement with the surface states measured by EIS, again consistent with the previous report under 1 sun illumination.[8] The surface states around 1.3 V *vs*. RHE (i.e. ~ the photocurrent onset potential) which are identified in both CV and EIS measurements was previously assigned to oxidized states (i.e. Fe^{IV}=O) involved in H_2O oxidation reaction (equation 6-1).[7,8]

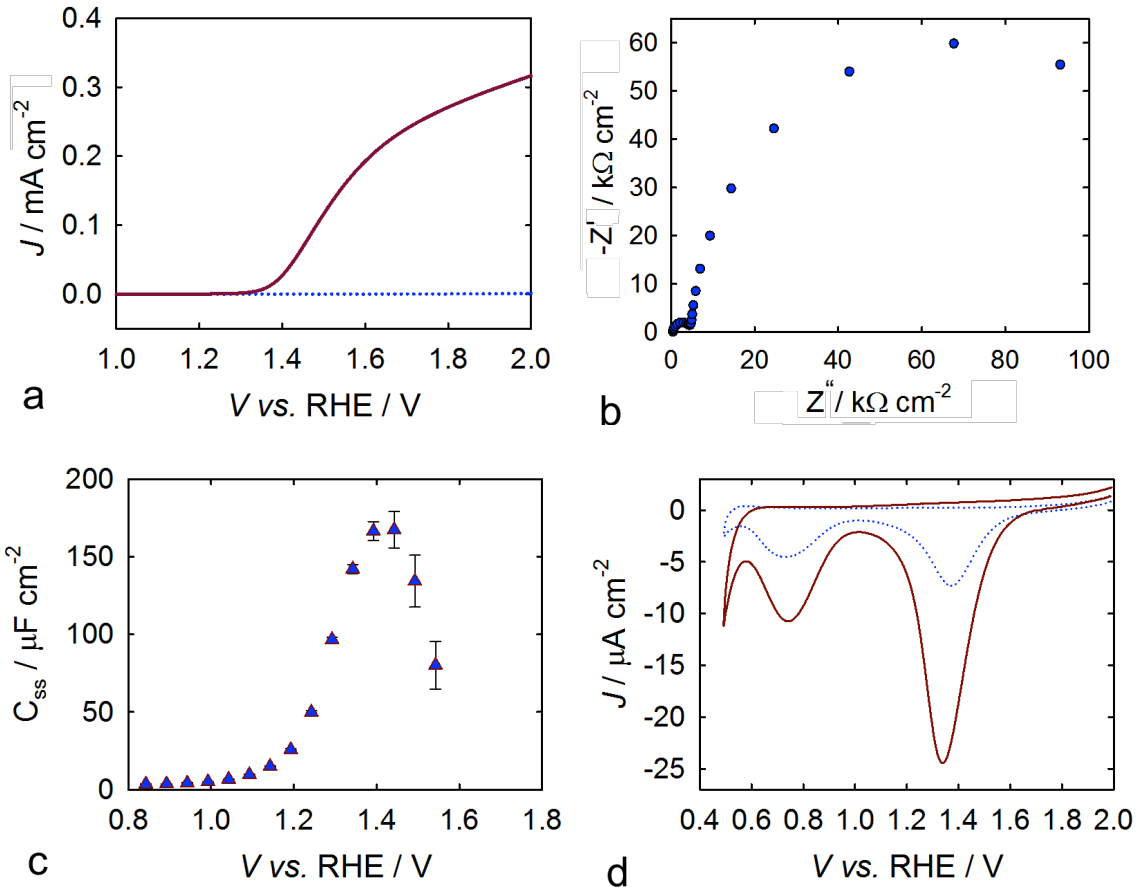

Figure 6-2. a) *J-V* curves of hematite electrodes measured in 0.1 M phosphate buffer (pH=7) in dark and under 395 nm monochromatic illumination. b) A Nyquist plots measured at 1.33 V *vs.* RHE under illumination. c) Surface states capacitance measured at various applied potential under illumination. d) CV curves scanned in dark at 500 mV/s immediately after holding the electrode at 2 V under illumination (solid dark red) and in dark (dotted blue).

Hematite Electrodes were also employed to photoelectrochemically oxidize water in a custom-made attenuated total reflectance infrared spectroscopy (ATR-IR) cell. The schematic cell configuration is shown in Figure 6-1. The *in-situ* IR cell consisted of a flow cell with multi-reflection ZnSe crystal. ZnSe IR element has a sharp cut-off energy at ~625

cm^{-1}. The tumbling mode of H_2O however, strongly reduces the IR transmittance in the 600-850 cm^{-1} which is where the vibration modes of *oxo* and *peroxo* groups are expected.[14] This limitation was circumvented by performing experiments in D_2O (i.e. splitting D_2O) as it provides a significantly better transmittance in this region (Figure 6-3). For *in-situ* measurements, the hematite electrode was fixed against the IR element with ~ 50 μL electrolyte (0.2 M KCl, pH=7.3). *In-situ* current-potential (*J-V*) measurements were performed to insure the feasibility of the PEC cell setup. Plots of *J-V* curves scanned in dark and under 400 nm monochromatic illumination (~ 10 mW cm^{-2}) are shown in Figure 6-3a. The resistive shape of the curves is due to uncompensated resistances mostly imposed by the geometry of the *in-situ* cell. In general, however, the shape of the *J-V* curves is in excellent agreement to the *ex-situ J-V* measurements in an electrochemical cell (Figure 6-2). The *in-situ* IR spectra where then scanned under constant applied potential in order to probe the surface of the hematite electrode in dark and under illumination. We note that surface states attributed to water oxidation intermediates are identified both in dark and under illumination in fast-scan cyclic voltammetry (CV) measurements (Figure 6-2d).

Figure 6-3b and c show IR absorption spectra scanned *in-situ* under electrochemical and PEC water oxidation, respectively. The spectra are corrected for the background absorption at a reference potential of 0.6 V *vs*. RHE (i.e. the flat band potential). Potential dependent spectral features were reproducibly resolved around 744 and 896 cm^{-1} for applied potential positive of the water oxidation current onset (1.7 V in dark and 1.25 V under illumination). The potential and light-dependent peak evolution is consistent with electrochemically or photoelectrochemically generated species on the electrode surface. The fact that the absorption peaks are only observed positive of the water oxidation current onset potential

indicates that theses absorption peaks are associated with species involved in the H_2O oxidation reaction.

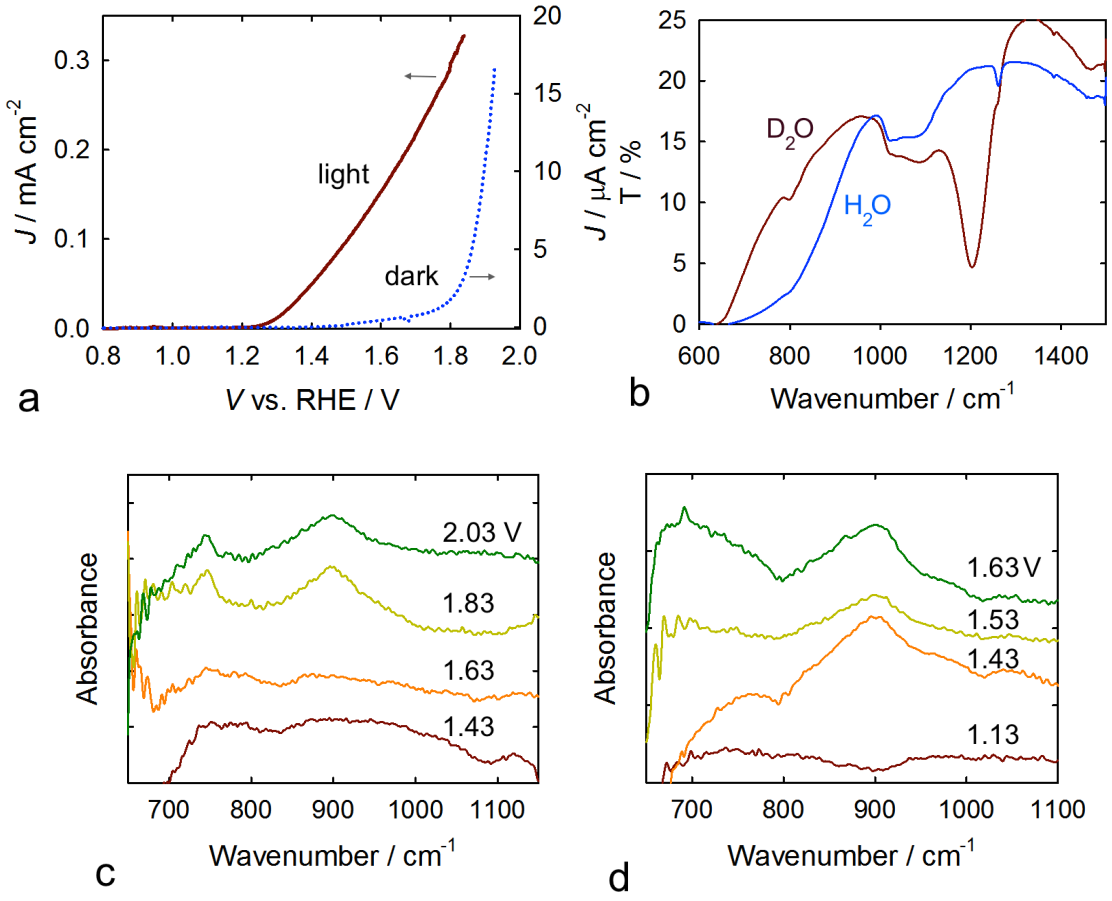

Figure 6-3. a) *J-V* curves of a hematite electrode measured *in-situ* in contact with D_2O (0.2 M KCl). b) The transmittance of the ZnSe IR element in contact with 0.2 M KCl in H_2O and D_2O. *In-situ* IR spectra scanned at a constant applied potential (labeled on the curves) in dark (c) and under monochromatic 395 nm illumination (d). IR spectra are corrected for the background at reference potential of 0.6 V *vs.* RHE.

Identical absorption peaks were also observed after turning the light on at 1.43 V (i.e. corrected for the background in the same applied potential in dark). As seen in Figure 6-4

photocurrent is generated after turning the light on at this applied potential. This indicates that these spectral features are associated with PEC water oxidation reaction. Further, no spectral feature was observed in the presence of iodide (0.2 M KI) as hole scavenger (Figure 6-4b). Under this condition holes are utilized to oxidize I^- as opposed to oxidizing surface states and subsequently water. Potential-dependent spectra and the control measurement in the hole scavenger therefore strongly support the assignment of the IR absorption peaks to species generated during water oxidation on hematite surface.

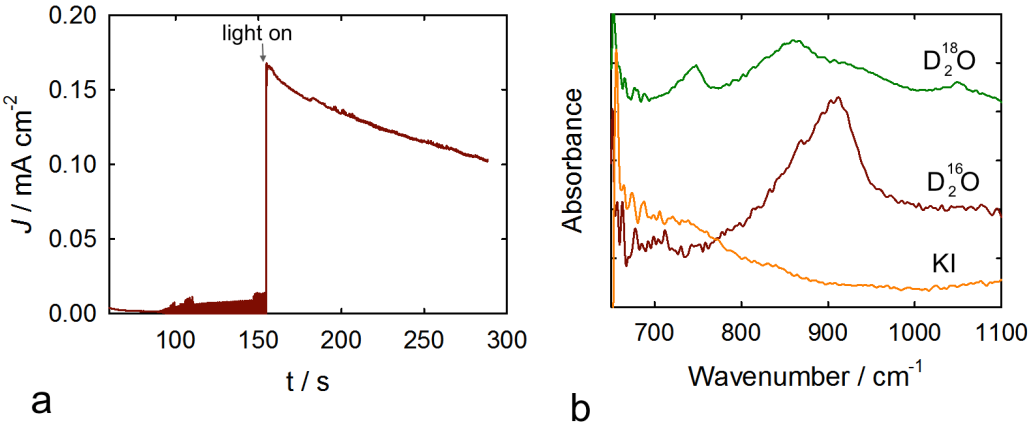

Figure 6-4. a) Current response of a hematite electrode measured *in-situ* at 1.43 V. b) IR absorption spectra collected at 1.43 V after turning the light on in contact with hole scavenger and isotope labeled water.

The vibration frequency of iron-*oxo* and *peroxo* groups have been studied extensively in molecular systems.[15] The vibration frequency of an Fe^{IV}=O group is expected to fall in 750-900 cm^{-1} region.[15–17] The O–O stretching mode of peroxide on the other hand lies in the 740-920 cm^{-1}.[14,18,19] Broad variation in the vibration frequencies is attributed to the degree of H-bonding and the spin state of Fe atom.[17,18] The observed IR vibration peaks can thus be

assigned to either Fe=O or FeO–OH groups forming during water oxidation. Performing experiment in ^{18}O labeled water thus was necessary to distinguish these vibrations as the FeO–OH can incorporate either one or two ^{18}O atoms and thus exhibit a larger frequency shift upon labeling. The $^{16}O/^{18}O$ shift for Fe=O is expected to be ~25-50 cm^{-2}. The frequency shift associated with O–O isotope exchange on the other hand between 20-30 cm^{-1} for partially labeled and 44 and 61 cm^{-1} for fully labeled groups.[18,20] *In-situ* spectra collected in contact with $D_2{}^{18}O$ exhibited two absorption peaks at 743 and 857 cm^{-1} (Figure 6-4b). According to this spectra, the 743 cm^{-1} mode is unchanged upon isotope labeling, while 896 cm^{-1} mode is shifted by 39 cm^{-1}. This isotope exchange frequency shift is consistent with an Fe=O group as a labeled peroxide group is expected to exhibit three different vibrations corresponding to ^{16}O-^{16}O, ^{16}O-^{18}O, and ^{18}O-^{18}O stretching modes. The fact that 743 cm^{-1} mode is not shifted upon labeling with ^{18}O indicates that this absorption peak is either due to groups which do not contain oxygen or inert iron-*oxo* groups which do not proceed to exchange oxygen.[12,18] Further experiments are planned to be conducted to fully understand the origin of this IR peak. Considering these findings, an H_2O oxidation mechanism can be established which involves the formation of an iron-*oxo* group as the product of the first oxidation reaction on the surface by the valence band holes. Subsequent attack by a water molecule and oxidative dissociation of a proton produces a surface peroxide intermediate which released O_2 upon further oxidation.

$$Fe^{III} - OH + h^+ \rightarrow Fe^{IV} = O + H^+ \quad (6\text{-}2)$$

$$Fe^{IV} = O + H_2O + h^+ \rightarrow Fe^{III} - O - OH + H^+ \quad (6\text{-}3)$$

$$Fe^{III} - O - OH + h^+ \rightarrow O_2 + Fe^{III} + H^+ \quad (6\text{-}4)$$

$$Fe^{III} + H_2O + h^+ \rightarrow Fe^{III} - OH + H^+ \quad (6\text{-}5)$$

6.5 Conclusion

Hematite electrodes were examined by *in-situ* IR spectroscopy under photoelectrochemical water oxidation conditions. Light and potential-dependent IR absorption peaks were resolved which correlate to the photoelectrochemical measurements. The combined photoelectrochemical and *in-situ* IR data indicate the formation of Fe^{IV}=O groups in the initial step of water oxidation on hematite surface as suggested by previous works.[1,5,7] These data thus provide the first direct evidence of water oxidation intermediates on hematite, which allowed us to establish a mechanism for water oxidation on hematite photoelectrodes.

REFERENCES

REFERENCES

(1) Young, K. M. H.; Klahr, B. M.; Zandi, O.; Hamann, T. W. *Catal. Sci. Technol.* **2013**, *3*, 1660.

(2) Upul Wijayantha, K. G.; Saremi-Yarahmadi, S.; Peter, L. M. *Phys. Chem. Chem. Phys.* **2011**, *13*, 5264.

(3) Barroso, M.; Pendlebury, S.; Cowan, A.; Durrant, J. *Chem. Sci.* **2013**, *4*, 2724.

(4) Cummings, C. Y.; Marken, F.; Peter, L. M.; Upul Wijayantha, K. G.; Tahir, A. A. *J. Am. Chem. Soc.* **2012**.

(5) Cummings, C. Y.; Marken, F.; Peter, L. M.; Tahir, A. a; Wijayantha, K. G. U. *Chem. Commun.* **2012**, *48*, 2027.

(6) Barroso, M.; Mesa, C. a; Pendlebury, S. R.; Cowan, A. J.; Hisatomi, T.; Sivula, K.; Grätzel, M.; Klug, D. R.; Durrant, J. R. *Proc. Natl. Acad. Sci. U. S. A.* **2012**, *109*, 15640.

(7) Klahr, B.; Gimenez, S.; Fabregat-Santiago, F.; Bisquert, J.; Hamann, T. W. *Energy Environ. Sci.* **2012**, *5*, 7626.

(8) Klahr, B.; Gimenez, S.; Fabregat-Santiago, F.; Hamann, T.; Bisquert, J. *J. Am. Chem. Soc.* **2012**, *134*, 4294.

(9) Klahr, B. M.; Gimenez, S.; Zandi, O.; Fabregat-Santiago, F.; Hamann, T. W. *ACS Appl. Mater. Interfaces* **2015**, *7*, 7653.

(10) Klahr, B.; Hamann, T. *J. Phys. Chem. C* **2014**, *118*, 10393.

(11) Trainor, T. P.; Chaka, A. M.; Eng, P. J.; Newville, M.; Waychunas, G. a.; Catalano, J. G.; Brown, G. E. *Surf. Sci.* **2004**, *573*, 204.

(12) Hellman, A.; Pala, R. G. S. *J. Phys. Chem. C* **2011**, *115*, 12901.

(13) Peter, L. M.; Wijayantha, K. G. U.; Tahir, A. a. *Faraday Discuss.* **2012**, *155*, 309.

(14) Sivasankar, N.; Weare, W. W.; Frei, H. *J. Am. Chem. Soc* **2011**, *133*, 12976.

(15) McDonald, A. R.; Que, L. *Coord. Chem. Rev.* **2013**, *257*, 414.

(16) Tiago de Oliveira, F.; Chanda, A.; Banerjee, D.; Shan, X.; Mondal, S.; Que, L.; Bominaar, E. L.; Münck, E.; Collins, T. J. *Science* **2007**, *315*, 835.

(17) Green, M. T. *J. Am. Chem. Soc.* **2006**, *128*, 1902.

(18) Zhang, M.; de Respinis, M.; Frei, H. *Nat. Chem.* **2014**, 1.

(19) Bonnot, F.; Tremey, E.; Von Stetten, D.; Rat, S.; Duval, S.; Carpentier, P.; Clemancey, M.; Desbois, A.; Nivière, V. *Angew. Chemie - Int. Ed.* **2014**, *53*, 5926.

(20) Nakato, K. *Infrared and Raman Spectra of Inorganic and Coordination Compounds*; John Wiley and Sons 1986.

Chapter 7:

Conclusions and future directions

7.1 Conclusions

As discussed in chapter 1, due to a zero hole diffusion length, the optimal thickness of an hematite electrode needs to be in the order of the depletion region, i.e. ~ 18 nm for hematite electrodes prepared by atomic layer deposition (ALD). Hematite ultrathin films were synthesized by ALD and studied under photoelectrochemical water oxidation. ALD's gas phase and self-limiting surface reaction allows uniform thin films with controllable and reproducible morphology. Systematic studies were then performed to better understand the performance limiting mechanism (i.e. charge recombination) impeding efficient water oxidation with hematite. Enhancement strategies were then developed and employed to mitigate charge carrier recombination resulting in enhanced water oxidation performance.

- A very first problem of ultrathin films is the substrate/substrate interface effect which results in a defective hematite layer at the interface known as "dead layer".[1] It was shown (chapter 2) that the dead layer effect can be eliminated through incorporation of an oxide under layer such as Ga_2O_3 or Nb_2O_5, also deposited by ALD. It was found that underlayer increases the film crystallinity compared to the film deposited on bare FTO substrates. 18 nm hematite film deposited on an FTO / 2 nm Ga_2O_3 thus produced water oxidation performance comparable to that of sufficiently thick state of the art planar electrodes.[1]
- The next major limitation of hematite thin film was the very low photovoltage (i.e. very positive photocurrent onset potential) generated under PEC water oxidation. The positive photocurrent onset, which is a general behavior for hematite electrodes, is attributed to surface recombination. Surface recombination is resulting from kinetic competition between the forward hole

collection *via* H_2O oxidation and back recombination of surface holes with conduction electrons. This is more prominent at low applied potential where band bending is small. We demonstrated that the extent of band bending and thus the charge separation at the interface is limited by Fermi level pinning at surface states, identified *via* cyclic voltammetry and electrochemical impedance spectroscopy (chapter 3). We further demonstrated that the shallow surface state causing Fermi level pinning (and surface recombination) can be removed through high temperature annealing.[2] Ultrathin hematite with a Ga_2O_3 underlayer annealed at 800 °C thus produced record photocurrent onset potential of 0.7 V *vs*. RHE for a bare hematite electrode.[2] It was shown that further modification with water oxidation catalyst Co-Pi effectively suppresses surface recombination producing the photocurrent onset just positive of the flat band potential and quantitative hole collection at 1.23 V *vs*. RHE (chapter 3).[3]

- Even with quantitate hole collection, the photocurrent magnitude generated with hematite thin film electrode was less than one quarter of the expected value based on the flux of the absorbed photons. This indicated that the rest of the photogenerated holes undergo recombination before reaching the electrode surface. More significantly the charge separation efficiently at very positive potential, where the entire bulk is expected to be depleted, was only 25% (chapter 3).[3] This further indicates the population of surface holes thus the photocurrent is limited by surprisingly strong depletion region recombination. We therefore attempted to enhance the charge separation by incorporating Ti dopant fabricated *via* alternative cycle ALD (chapter 4). Ti-doping in principal

can enhance the n-type carrier density and thus increase the conductivity. More relevant to hole transport and collection in the depletion region, a higher dopant density can place a sharper band bending at the interface which accelerates charge separation. In contrary to the majority of literature on Ti-doped hematite, it was found that Ti-doing is not acting as an electronic dopant when added to hematite.[4] The performance enhancement was attributed to an increased hole transport and collection efficiency through a structural modification.[4,5]

- Another strategy to enhance the charge separation hence the photocurrent of hematite is through fabrication of highly crystalline hematite. Higher crystallinity can increase the hole life time, and mobility, thus enhancing charge separation. Due to ALD's gas phase conformal growth it is difficult to alter the deposition mode and crystalline properties of the hematite films prepared with this approach. It was demonstrated in chapter 5 that electrodeposition (ED) can be utilized alternatively to fabricate hematite electrode of variable morphology. ED results in amorphous FeOOH films producing a highly crystalline hematite after annealing at elevated temperature. Planar thin film electrode prepared with ED produced unprecedented water oxidation performance compared to the planar films reported to date (chapter 5). The better performance was found that is due to enhanced charge transport resulting from increased crystallinity (which produces a nonzero hole diffusion length) and enhance surface hole collection due a sharper band bending at the interface.
- It was shown in chapter 3 that surface properties of hematite electrodes play a key role in determining the hole collection efficiency. It has been shown that

water oxidation on hematite surface is associated with the formation of oxidized surface sates which further proceed to evolve oxygen (chapter 3).[6,7] In chapter 6 we present the first direct evidence of oxidized surface states, i.e. water oxidation intermediates *via* an *in-situ* PEC-IR method. These results helped us to establish the mechanism of H_2O oxidation on hematite, reconciling the long-lasting controversy as to the role of surface states in water oxidation with this material.[3,8]

7.2 Future directions

Substantial improvement has been made in the water oxidation performance of hematite electrodes in the last few years. Very promising photocurrent onset of 0.45 V *vs*. RHE was reported recently.[9] Depletion region recombination, however, still effectively limits the bias-dependent charge separation efficiency and thus the photocurrent. It is this loss mechanism that still constrains the fill factor and thus the overall water splitting efficiency. Future research therefore should be focused on enhancing charge separation, i.e. suppressing depletion region recombination, in order to generate high photocurrent with minimal applied bias.

In chapter 5 it was found that electrodeposited hematite shows increased hole diffusion length which was attributed to higher crystallinity. These electrodes, however, also showed a surprisingly high dopant density which substantially reduces the width of the depletion region. This would also reduce the number of photogenerated holes in this region which decreases the photocurrent. It would be interesting to see how these electrodes preform if

one could limit the dopant density sufficiently low while taking advantage of a high crystallinity.

Another interesting strategy is crystal orientation-dependent hole collection (i.e. anisotropic hole transport) which has been shown that is enhancing charge separation efficiency.[10] More work is needed to better understand the beneficial effect of preferential crystallographic orientations on the hole transport and collection in hematite in order to fully exploit this strategy.

Another strategy is fabricating an n-p junction in order to accelerate charge separation in the depletion region. One example of this approach was shown for Mg-doped hematite overlayer which produced enhanced water oxidation performance.[11] Recently Jang *et al.* utilized an amorphous $NiFeO_x$ catalyst which pushed the water oxidation photocurrent onset of hematite to an unprecedented value of 0.45 V vs. RHE.[9] The observed cathodic shift of >300 mV on already well-performing hematite electrodes is significantly higher than the effect of common electrocatalysts such as Co-Pi. Therefore, the role of $NiFeO_x$ is unlikely to be catalysis or surface passivation. In addition, considering that the fill factor and the turn on photocurrent slope were significantly improved with $NiFeO_x$, there is a possibility that hematite-$NiFeO_x$ is behaving as a n-p junction which facilitates hole transport and collection at the interface. More work is required to unravel the details of this exciting result so it can be further exploited.

Once the depletion region recombination is suppressed and electrodes with high APCE is realized, the thin films can be optically scaled up on a nanostructured TCO substrates using TFA approach (chapter 2).[3] Given the recent improvement in the photovoltage and

parallel ongoing progress in photocathode systems, hematite thus still holds the promise of enabling efficient and stable water splitting in a tandem PEC device.

REFERENCES

REFERENCES

(1) Zandi, O.; Beardslee, J.; Hamann, T. *J. Phys. Chem. C* **2014**, *118*, 16494.

(2) Zandi, O.; Hamann, T. *J. Phys. Chem. Lett.* **2014**, *5*, 1522.

(3) Zandi, O.; Hamann, T. *Phys. Chem. Chem. Phys.* **2015**, *17*, 22485.

(4) Zandi, O.; Klahr, B.; Hamann, T. *Energy Environ. Sci.* **2013**, *6*, 634.

(5) Kronawitter, C. X.; Zegkinoglou, I.; Shen, S.-H.; Liao, P.; Cho, I. S.; Zandi, O.; Liu, Y.-S.; Lashgari, K.; Westin, G.; Guo, J.-H.; Himpsel, F. J.; Carter, E. a.; Zheng, X. L.; Hamann, T. W.; Koel, B. E.; Mao, S. S.; Vayssieres, L. *Energy Environ. Sci.* **2014**, *7*, 3100.

(6) Klahr, B.; Gimenez, S.; Fabregat-Santiago, F.; Hamann, T.; Bisquert, J. *J. Am. Chem. Soc.* **2012**, *134*, 4294.

(7) Klahr, B. M.; Gimenez, S.; Zandi, O.; Fabregat-Santiago, F.; Hamann, T. W. *ACS Appl. Mater. Interfaces* **2015**, *7*, 7653.

(8) Young, K. M. H.; Klahr, B. M.; Zandi, O.; Hamann, T. W. *Catal. Sci. Technol.* **2013**, *3*, 1660.

(9) Jang, J.-W.; Du, C.; Ye, Y.; Lin, Y.; Yao, X.; Thorne, J.; Liu, E.; McMahon, G.; Zhu, J.; Javey, A.; Guo, J.; Wang, D. *Nat. Commun.* **2015**, *6*, DOI: 10.1038/ncomms8447.

(10) Kment, S.; Schmuki, P.; Hubicka, Z.; Machala, L.; Kirchgeorg, R.; Liu, N.; Wang, L.; Lee, K.; Olejnicek, J.; Cada, M.; Gregora, I.; Zboril, R. *ACS Nano* **2015**, *9*, 7113.

(11) Lin, Y.; Xu, Y.; Mayer, M. T.; Simpson, Z. I.; McMahon, G.; Zhou, S.; Wang, D. *J. Am. Chem. Soc.* **2012**, *134*, 5508.